

Doctoral thesis

Doctoral theses at NTNU, 2022:120

Adina Basa

Hydrogen-material interactions on austenitic and super duplex stainless steels

NTNU
Norwegian University of Science and Technology
Thesis for the Degree of
Philosophiae Doctor
Faculty of Engineering
Department of Mechanical and Industrial
Engineering



Norwegian University of
Science and Technology

Adina Basa

Hydrogen-material interactions on austenitic and super duplex stainless steels

Thesis for the Degree of Philosophiae Doctor

Trondheim, May 2022

Norwegian University of Science and Technology
Faculty of Engineering
Department of Mechanical and Industrial Engineering



Norwegian University of
Science and Technology

NTNU

Norwegian University of Science and Technology

Thesis for the Degree of Philosophiae Doctor

Faculty of Engineering

Department of Mechanical and Industrial Engineering

© Adina Basa

ISBN 978-82-326-5288-4 (printed ver.)

ISBN 978-82-326-5250-1 (electronic ver.)

ISSN 1503-8181 (printed ver.)

ISSN 2703-8084 (online ver.)

Doctoral theses at NTNU, 2022:120

Printed by NTNU Grafisk senter

Preface

This dissertation is submitted to the Norwegian University of Science and Technology (NTNU), in fulfilment of requirements for the Doctor of Philosophy degree. The experimental work and partial publishing of results has been conducted within January 2009 – July 2013 under the supervision of Prof. Christian Thaulow, from the Department of Mechanical and Industrial Engineering/NTNU and co-supervision of Vigdis Olden, from the Department of Materials and Nanotechnology/SINTEF. The theoretical and publishing of latest results were conducted under the supervision of Prof. Nuria Espallargas and co-supervision of Di Wan from the Department of Mechanical and Industrial Engineering/NTNU. The main experimental work was carried out in the NTNU Nanomechanical Lab, the samples preparation was performed in the Metallography Laboratory and Corrosion Laboratory at the Department of Mechanical and Industrial Engineering/NTNU, while sample characterization prior and post testing took place in the Electron Microscopy Lab from the Department of Materials Science and Engineering and NTNU NanoLab Cleanroom, which is part of the Norwegian Micro- and Nanofabrication Facility (NorFab).

The thesis was financially supported through the Petromaks Programm, Project No. 10290803 by the Research Council of Norway (RCN).

The thesis comprises a summary of the PhD work and four articles published in peer-reviewed scientific journals or conferences.

Adina Basa

December 2021



Acknowledgements

To be here, in this phase, after all the challenges that life brought it along in the last years, it still feels like a dream. A dream that could have not become true without the help from some people.

I am so grateful for the support, guidance, patience and motivation I received in the last couple of years from my supervisor, Prof. Nuria Espallargas. The discussions with you, both personally and mostly professionally have been reinvigorating and brought me back on track every time. I would also like to thank my co-supervisors, Dr. Di Wan and Dr. Vigdis Olden. Di, you have helped me so much and I am deeply thankful to you. Vigdis, you have been the first person to meet when I came to NTNU and I am so grateful for all the support you gave me along these years.

Of course, I wouldn't have come to Norway if it wasn't for Prof. Roy Johnsen, who created this PhD position as a leader of this project, and to Prof. Christian Thaulow, my first supervisor. Thank you Roy for giving me this opportunity and for all your support of course. Christian, thank you for all the guidance and discussions we had until I left Trondheim and prior to your retirement and I wish you all the best in enjoying the life after university.

Going back in time, I would also like to thank Prof. Afrooz Barnoush, for all the guidance and support he showed me throughout the years. Also, I would like to thank all my colleagues and collaborators, from both Sintef Industry, where I was given an office in the first years of my PhD, and from NTNU. Anna, Esmá, Bjørn Rune, Inga, Christer, Nousha, Antonio and many others, thank you to all of you, it was such a pleasure to share the office and so many lunch hours with you.

After I left NTNU, I got so much support and encouragements from my employer that I would like to express my huge thanks to them as well. Richard, Kjell, Andreas, Bård, Anne Mathilde, thank you all for everything you have done for me both professionally and personally, especially through my not that good times.

Last, but not least I would like to thank my family. My parents would have been so proud, and I am so sorry I couldn't finish this while they were still among us, but somehow I know that they are watching and protecting us from the place they are now. My parents-in-law need

special thanks because they encouraged me at all times to finish, especially my mother-in-law that was always telling me: “of course you can do it!” Thank you from the bottom of my heart (Multumesc buca!)

But I am mostly dedicating this work to my husband and to my wonderful two boys. I wanted to give up so many times, but every single time you were there, Claudiu to support me and to not let me do it. Every time I was telling you that I could not, you just told me to be patient and to let the time to heal the wounds and then the motivation will come. I honestly did not believe you at that time, but I am so happy that I heard you, and I did not close the doors to this opportunity. So, this is for you, my love.

Abbreviations

AIDE	Adsorption-Induced Dislocation Emission
AP	Anodic Potential
ASS	Austenitic Stainless Steel
CP	Cathodic Potential
DEFACTANT	DEfect ACTing AgeNTs
DSS/SDSS	Duplex / Super Duplex Stainless Steel
ECNI	Electrochemical Nanoindentation
EP	Electropolishing
FIB	Focused Ion Beam
FSS	Ferritic Stainless Steel
HC	Hydrogen Charging
HE	Hydrogen Embrittlement
HEDE	Hydrogen Enhanced Decohesion
HELP	Hydrogen Enhanced Local Plasticity
HER	Hydrogen Evolution Reaction
HESIV	Hydrogen-Enhanced Strain-Induced Vacancy
HIE	Hydride-Induced Embrittlement
MSS	Martensitic Stainless Steel
OArP	Oxygen-Argon Plasma
OGM	Orientation Gradient Mapping
SEM-EBSD	Scanning Electron Microscopy - Electron Backscattered Diffraction
SPM	Scanning Probe Microscopy
TI	Tribo Indenter



List of tables

Table 1 Chemical composition of the selected steels	27
Table 2 Heat treatment applied to the selected samples.....	27
Table 3 Electropolishing parameters	27



List of figures

Figure 1 Schematic of gas – solid interaction: a) Hydrogen molecules approaching the material surface, b) physisorption, c) chemisorption and d) absorption. Adapted from [93]	22
Figure 2 Micro-mechanisms of hydrogen embrittlement, where hydrogen is marked by the purple circles. Adapted from [96]	24
Figure 3 SDSS sample a) phase map, where red is the ferrite and green is the austenite; b) inverse pole figure map revealing the crystallographic orientation of the grains	28
Figure 4 Austenitic 316L SS inverse pole figure map	28
Figure 5 Experimental setup for in-situ ECNI testing	30
Figure 6 View inside the Tribo Indenter TI 950	30
Figure 7 a) Cross-sectional area of an indentation, b) typical load – displacement curve	31
Figure 8 Picture of the Helios NanoLab™ DualBeam™ system with a schematic detail of the ion beam and electron beam interacting with the surface	33
Figure 9 Interaction between an ion beam with a solid surface gives a) less material removal or b) more material removal on larger angles of incidence [124]	33
Figure 10 Schematic illustration of the EBSD principle. Adapted from [135]	34
Figure 11 Load - displacement curves resulted from in situ electrochemical nanoindentations made on 316L ASS, first in air and later under hydrogen charging (HC) on a) freshly electropolished sample and b) 5 min OArP treated sample	37
Figure 12 Pop-in behaviour with the error bars representing the standard deviation, a) austenitic phase of SDSS, b) 316L ASS.....	38
Figure 13 Hardness behaviour with the error bars representing the standard deviation, a) austenitic phase of SDSS, b) 316L ASS.....	38
Figure 14 SPM topography images after nanoindentation of a 316L sample under hydrogen charging a) pre- and b) post-OArP treatment	38

Figure 15 SDSS sample a) imaged after 6 hour of hydrogen charging on a sample treated for 5 minutes with OArP, b) slip lines captured in austenitic grain after 85 minutes of hydrogen charging on a freshly electropolished sample (without OArP treatment).....	39
Figure 16 The reduction in the onset of plasticity (pop-in load level) due to hydrogen on SDSS	39
Figure 17 Pop-in width and pop-in load from the pop-in analysis.....	40
Figure 18 The hydrogen effect on the SDSS sample hardness.....	40
Figure 19 a) Representative LD curves for 316L SS in different charging potentials and b) the corresponding SPM images, where CP1=-740mV, CP2=-808mV, CP3=-884mV and AP=+100mV	41
Figure 20 Pop-in data from the ECNI of a 316L sample under different charging conditions: a) pop-in load; b) pop-in width	41
Figure 21 Hydrogen effect on nanomechanical properties of 316L sample: a) hardness and b) reduced modulus on low cathodic potentials, c) hardness on high cathodic potentials	42
Figure 22 FIB milled areas in an austenite grain of SDSS sample: a) SEM image of all the patterns milled with different parameters; b) phase map where green is austenite and red is ferrite, c) IPF map showing the change in the crystallographic orientation of the grains after milling	43

Table of Contents

Preface.....	3
Acknowledgements.....	5
Abbreviations	7
List of tables	9
List of figures	11
1. INTRODUCTION	15
1.1. Background and motivation	15
1.2. Objectives	18
1.3. Thesis overview	18
2. HYDROGEN-MATERIAL INTERACTION	21
2.1. Hydrogen entry into metal	22
2.2. Mechanisms of Hydrogen Embrittlement	24
3. MATERIALS AND SAMPLE PREPARATION	27
4. EXPERIMENTAL TECHNIQUES.....	29
4.1. Electrochemical nanoindentation (ECNI)	29
4.2. Focused Ion Beam (FIB) microscopy	32
4.3. Scanning Electron Microscope - Electron Backscatter Diffraction mapping (SEM-EBSD) ..	34
5. MAIN RESULTS.....	37
5.1. Oxygen Argon plasma effect on hydrogen uptake in steels	37
5.2. Hydrogen effect on the nanomechanical properties of SDSS and 316L ASS	39
6. SUMMARY OF PAPERS.....	45
7. CONCLUSIONS AND FURTHER WORK.....	51
8. REFERENCES	53
9. APPENDICES.....	61
PAPER I	63
PAPER II	77
PAPER III	99
PAPER IV	111



1. INTRODUCTION

1.1. Background and motivation

Severe damages caused by Hydrogen Induced Stress Cracking (HISC) in subsea pipelines and fittings were investigated in the Petromaks project entitled "***Prevention of hydrogen induced stress cracking in subsea pipelines and production systems made from stainless steel***". This PhD thesis was financed entirely by this project and the main objective was to develop a fundamental understanding of the effect of hydrogen on the mechanical properties of some stainless steels relevant for the project and their partners. The research work has been primarily performed through nanoindentation experiments under electrochemical charging.

For many years, all kinds of industries have experienced numerous problems due to the interaction between hydrogen and structural materials, especially metal alloys such as stainless steels [1]. The diversity of the stainless steels family in combination with their excellent corrosion resistance makes them an excellent choice in endless applications, from oil and gas production and power generation industries to biomedical alloys, civil infrastructure or automotive industry. Steels become stainless when added in their composition at least 12 wt.% of Chromium (Cr), with some stainless steel grades containing as much as 25 wt.% Cr in their composition in addition to other alloying elements that strengthen their corrosion resistance, such as Nickel (Ni), Molybdenum (Mo), Nitrogen (N), etc [2-5]. In many applications, stainless steels are used in combination with mechanical load and cathodic protection, like in the oil and gas industry or in pipeline and pressure applications [2]. In these applications, hydrogen is generated due to the cathodic protection measures taken (typically under electrochemical control). Hydrogen is a very small atom that easily ingresses into the metal microstructure leading to the deleterious effects on the chemical and mechanical properties of metal alloys (and materials in general). This is known as hydrogen embrittlement (HE) and it has been widely documented in many different types of steels [1, 6-9]. Regardless of the outstanding corrosion resistance of the different grades of stainless steels, their properties are still affected by the hydrogen diffusion into the microstructure [6, 10-12].

The damaging effects of hydrogen on the structural properties of Iron (Fe) and steels were first published in 1875 by Johnson [13] who proposed the theory that the hydrogen locked in

interspaces impedes the movement of Fe atoms. Since then, intensive efforts and studies have been made to characterize and understand the mechanisms of this phenomenon, i.e. the effect of hydrogen on the degradation of metal structures [14-16]. However, not only hydrogen can have a detrimental effect on the mechanical properties of metals and steels, other gases like oxygen, nitrogen and argon have been reported to negatively affect the mechanical stability of metals [17, 18]. However, the effect of hydrogen on metals is the most widely studied, and this attention will grow in the coming years with the green shift and the increased interest in hydrogen production and transport for more sustainable energy production systems. Therefore, it is important to elucidate the mechanisms behind hydrogen material interaction, as well as to find solutions to protect the materials against hydrogen uptake and to minimize, even discard, its damaging effect.

Stainless steels are classified based on their microstructures: martensitic or transformable stainless steels (MSS), ferritic stainless steels (FSS), austenitic stainless steels (ASS) and duplex / super duplex stainless steels (DSS/SDSS). The focus of this PhD thesis has been mainly on ASS but some investigations on SDSS have also been reported.

Due to their enhanced corrosion and oxidation resistance, FSSs are attractive materials for applications in oil and gas as well as in automotive and marine industries. Even though they have relatively low price compared to the ASS grades [8, 9, 19-25], the most commonly used materials for hydrogen storage and transportation are the austenitic stainless steels. These alloys exhibit high corrosion resistance combined with good mechanical properties, especially ductility (yield strength from 205 to 260 MPa, tensile strength up to 515 MPa and 40 % elongation [26]). However, when exposed to cathodic protection methods or when used in pressurized hydrogen gas environments, their excellent mechanical properties can be compromised with an unexpected early failure [27]. Among different types of ASSs, the more expensive versions containing Ni and Mo (e.g. AISI 316L) make other, more affordable versions of ASSs (e.g. AISI 304), much more often chosen in hydrogen applications [27-30].

Other, very intensively used, materials for subsea equipment are duplex and super duplex stainless steels, due to their excellent mechanical properties as well as corrosion resistance provided by the dual phase microstructure (austenite/ferrite) and the very high content of Cr (> 20wt.%) [31]. Despite these strong points, SDSS has often failed due to hydrogen generated during cathodic protection leading to hydrogen embrittlement. Although the concentration of hydrogen may be higher in austenite, the ferrite is prone to crack propagation at lower hydrogen concentrations [15]. Even though many experimental studies [32, 33] and

simulations [34, 35] of hydrogen effects on SDSS have been done, a more complete understanding of the micro-mechanism is still needed.

Hydrogen was reported to increase dislocation density in both austenite and ferrite phases of different ferritic, austenitic and duplex stainless steels [36-38]. In literature, the austenite to martensite phase transformation has also been related to hydrogen embrittlement [39-42]. After electrochemical cathodic charging of a DSS, strain releasing effects and elastic stresses have been the causes for γ -austenite transformation to ϵ -martensite and/or to α' -martensite during desorption of hydrogen [42]. After hydrogen charging, the lattice parameter expansion of up to 2% observed in austenite resulted in surface damages [41, 43, 44].

Despite the considerable progress that has been done in recent years, there are still a number of key open questions related to HE or mechanical properties' degradation of stainless steels due to hydrogen intake. There is still a considerable disagreement in the literature regarding the underlying mechanisms responsible for HE, thus a comprehensive understanding of the hydrogen effect on the properties of stainless steels in general is still required to develop the next generation of steels with resistance to hydrogen and other chemical elements that might have an effect in their mechanical integrity.

There are many methods used nowadays for investigating the hydrogen effect on steels, from traditional methods like tensile testing of hydrogen charged samples [45, 46] to in-situ micro tensile testing [20, 47-49], to electrochemical nanoindentation [50-52] and in-situ micro and nanopillar compression [48, 53, 54]. Electrochemical nanoindentation (ECNI) is the method used during this thesis to investigate the hydrogen effect on materials properties. The method allows sample testing while in-situ hydrogen charging, the charging conditions are controlled by switching from cathodic potentials (charging conditions) to anodic potentials (discharging conditions). Thus, this method makes it possible to catch the immediate hydrogen effect. Also, other advantages on using electrochemical nanoindentation are the reduced testing time and the refined testing area for small scale behaviour. In addition, it minimizes the hydrogen discharging while transferring a sample from the charging experimental setup to the testing setup.

The importance of sample preparation prior testing is crucial, especially that an improper preparation could result in a phase transformation. A mechanically deformed layer resulting from sample polishing can undergo an austenitic to martensitic phase transformation [55]. Also ion implantation can change the chemical composition of the alloy, thus by implantation of nickel and nitrogen, which are strong austenite-stabilizing ions, it was shown that

martensite can transform into austenite [56]. Focused Ion Beam (FIB), one of the intensively used techniques for sample characterization [57, 58] and preparation [53, 59], uses Gallium ions and their effect on material's chemical composition is becoming a concern [60]. Since FIB is used as sample preparation method in this PhD thesis, it is important to elucidate Gallium ion implantation effects on austenite stability prior testing.

1.2. Objectives

The main objective of this thesis is to derive a fundamental understanding of the hydrogen interaction with materials microstructures using advanced characterization techniques like electrochemical nanoindentation (ECNI), scanning electron microscopy coupled with electron backscattered diffraction (SEM-EBSD) and focused ion beam (FIB). Primary and secondary objectives of this research work are:

- Develop a nanomechanical testing procedure and sample preparation using the newly purchased Tribo Indenter equipment at NTNU, in 2009.
- Implement the ECNI experimental setup on the Tribo Indenter and prepare the in-situ hydrogen charging testing procedure.
- Investigate the effect of oxygen-argon plasma treatment applied during sample preparation of a 25%Cr SDSS and a 316L ASS on further hydrogen uptake.
- Investigate the chemically-induced austenite-to-ferrite phase transformation under gallium implantation in the austenitic phase of a 25%Cr SDSS during FIB milling.
- Investigate the effect of hydrogen on the nanomechanical properties of 316L ASS throughout ECNI experiments.

1.3. Thesis overview

The thesis is structured in 9 chapters, where the first 8 represent the background and motivations of the work done, state of the art, experimental techniques used and the main results, while the Appendices in chapter 9 are a summary of the published papers.

The following papers have been produced during this PhD. Papers I, II and III have been published already in peer-reviewed journals and the results from Paper IV were presented in two international conferences.

Paper I: Afrooz Barnoush, **Adina Basa** and Christian Thaulow, *Oxygen argon plasma treatment effect on hydrogen uptake in austenitic stainless steels*. International Journal of Hydrogen Energy, 2014, 39(26), 14120–14131,

<https://doi.org/10.1016/j.ijhydene.2014.06.161>

Paper II: **Adina Basa**, Christian Thaulow and Afrooz Barnoush, *Chemically induced phase transformation in austenite by focused ion beam*, Metallurgical and Materials Transactions A, 2014, 45(3), 1189–1198, <https://doi.org/10.1007/s11661-013-2101-4>

Paper III: **Adina Basa**, Dong Wang, Nuria Espallargas and Di Wan, *An in-situ electrochemical nanoindentation (ECNI) study on the effect of hydrogen in the mechanical properties of 316L austenitic stainless steel*. Materials, 2021, 14(21), 6426, <https://doi.org/10.3390/ma14216426>

Individual contribution: the PhD candidate has performed all experimental work of this PhD, under the guidance of the co-authors. The results published in the papers are direct findings of the PhD candidate during the experimental work. All the authors were involved in the discussion of the results, drafting the manuscripts and the final approval towards publication.

In addition, the PhD candidate has contributed to conference presentations and articles listed below. The presenting author is underlined.

- International Conference on Steel and Hydrogen; September 28 – 29, 2011, Ghent, Belgium.

Adina Basa, Christian Thaulow and Vigdis Olden, *In situ nanoindentation testing of hydrogen degradation on super duplex stainless steel*. (Conference presentation)

- International Conference Diagnosis and Prediction in Mechanical Systems Engineering; May 31 – June 1, 2012, Galati, Romania.

Adina Basa, Afrooz Barnoush and Christian Thaulow, *Nanomechanical testing of hydrogen effects on super duplex stainless steel*. Mechanical Testing and Diagnosis, ISSN 2247-9635, 2012 (II), Volume 2, pp. 5–14. (Conference presentation and paper)

2. HYDROGEN-MATERIAL INTERACTION

Over the years, many metal degradation processes due to the interaction with hydrogen have been described in literature. The severity and character of the hydrogen damage depends on the source of hydrogen, stress level and/or treatment applied to materials. The hydrogen can either be initially present in the material as internal hydrogen or come from the environment to which the material is exposed as external hydrogen [61, 62].

Internal hydrogen embrittlement (IHE) involves the concentration of pre-existing hydrogen in regions of high hydrostatic residual stress resulting in cracking under stresses below the yield stress [63-65]. Hydrogen environment embrittlement (HEE) describes subcritical cracking of materials under sustained loads in hydrogen or hydrogen-sulphide gases [28, 66-70].

Other terminologies for the hydrogen effect on materials are used in specific industries. Hydrogen-assisted cracking (HAC) [71-73] and hydrogen-assisted fatigue [74-78] have been also reported. In the welding industry it is used the term hydrogen-assisted cold cracking (HACC) when welds are subjected to cracking after cooling to room temperature [79-81]. Stress-oriented hydrogen induced cracking is used mostly in the oil and gas industry when cracking has a ladder-like morphology due to cracking from elongated inclusions distributed along the rolling direction of the plate [82-84]. Other forms of hydrogen damage are blistering and hydrogen attack.

Apart from the hydrogen blistering and hydrogen attack the rest of the hydrogen damage types mentioned above can be traced back to the hydrogen effect on mechanical properties of the metal. The deleterious effect of hydrogen on the mechanical properties of metals manifest itself in the form of a reduction in the ductility during tensile testing of hydrogen charged samples [85-87]. The effect is different in various metals and alloys and typically scales itself with the strength of the alloy [47, 88-90].

2.1. Hydrogen entry into metal

The hydrogen entry into materials is a complex process with many dependent parameters, while the material properties are affected regardless if hydrogen entered from a gaseous phase or a liquid phase. Different charging methods have been used in literature to allow hydrogen enter materials. In this section, a summary of some commonly used methods, as well as their theoretical backgrounds are given.

Hydrogen resulting from gaseous phase

Three main processes characterize the gas–solid interaction: physisorption, chemisorption, and absorption, Figure 1. Physisorption is a completely reversible process and occurs instantaneously due to van der Waals forces between a surface and an adsorbent. The chemical reaction between the surface atoms and the adsorbent molecules is described as chemisorption and it can be a slowly reversible or completely irreversible process [91]. Finally, absorption happens when the products of chemisorption penetrate the surface and diffuse into the bulk lattice of the material. The absorption capacity of hydrogen into material depends however on the samples' type and microstructure. The literature is intensively dissecting the nature of hydrogen dissolved in transition metals, on whether it is present as atom (H), proton (H^+) or gas (H_2) [92].

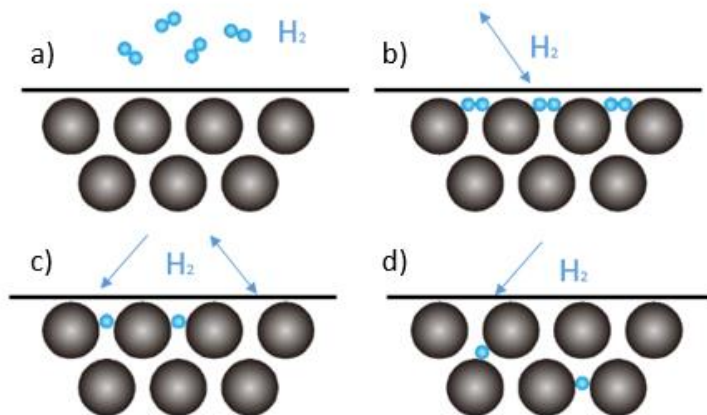
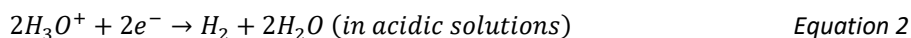
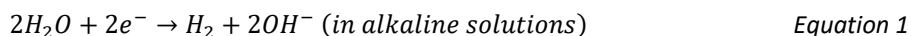


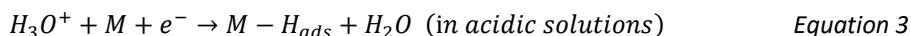
Figure 1 Schematic of gas – solid interaction: a) Hydrogen molecules approaching the material surface, b) physisorption, c) chemisorption and d) absorption. Adapted from [93]

Hydrogen resulting from cathodic charging

One intensively used method in studying the effect of hydrogen on materials through electrochemical charging during cathodic polarization. The cathodic reaction in aqueous electrolytes generates hydrogen and the hydrogen evolution reaction (HER) depends on the pH of the media:



There are two successive steps which contribute to the overall HERs mechanism. In the first step, common to all metals, the hydrated protons are discharged in acid solutions while in alkaline solutions the water is decomposed into oxygen and hydrogen gas. This process is known as water electrolysis:

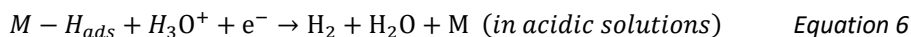


where H_{ads} represents the hydrogen atom adsorbed on a metal surface.

The second step is the desorption of hydrogen atoms from the metal surface, which can either be through chemical or electrochemical desorption. The chemical desorption, known also as catalytic recombination, occurs in both acid and alkaline solutions:



While the electrochemical desorption is pH dependent:



In this PhD thesis, cathodic charging was used in the experimental part to evaluate the hydrogen effect on stainless steels due to its simplicity and the safety of the process as compared to working with hydrogen gas under pressure.

2.2. Mechanisms of Hydrogen Embrittlement

Different micro-mechanisms have been proposed over the years for interpreting the variation in properties due to hydrogen ingress in metals [1, 41, 90, 94-98] namely, the hydride-induced embrittlement (HIE), the hydrogen enhanced decohesion (HEDE), the hydrogen enhanced local plasticity (HELP), the adsorption-induced dislocation emission (AIDE), the hydrogen-enhanced strain-induced vacancy (HESIV) formation, and lately the DEFACTANT theory, Figure 2. Each mechanism defines the material behaviour observed in special conditions and is strongly affected by stress and environment. In other words, these mechanisms are system-dependent mechanisms and might not be used as universal mechanisms for the effect of hydrogen on metals. Hydrogen embrittlement mechanisms can occur separately or in combination [99] and during crack initiation and crack growth one or more mechanisms can take the dominant role.

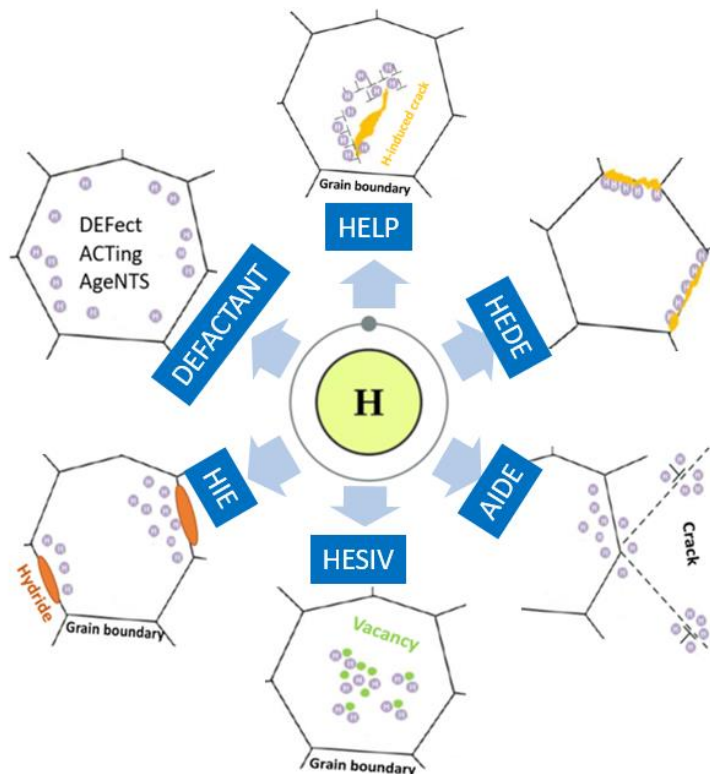


Figure 2 Micro-mechanisms of hydrogen embrittlement, where hydrogen is marked by the purple circles. Adapted from [96]

The hydride-induced embrittlement (HIE) mechanism describes the fracture of metal hydrides nucleated at the crack tip due to hydrogen diffusion ahead of the crack [11, 100]. According to Birnbaum et al. [101], HIE mechanism is influenced by the temperature at which the stable metal hydrides are brittle and the strain rate conditions that give time for the hydrogen to diffuse.

The hydrogen enhanced decohesion (HEDE) mechanism has been intensively reported in literature [90, 102, 103]. The mechanism reported initially by Troiano [104] and further developed by Oriani [105] is based on the hypothesis that the cohesive bonding strength between metal atoms is reduced by the hydrogen diffused within the lattice.

The hydrogen enhanced localized plasticity (HELP) is the mechanism proposed by Beachem [71] and developed further by Birnbaum and Sofronis [106] in which the distance between dislocations is reduced by hydrogen. The enhanced plasticity results in a localized softening along preferred crystallographic planes at the crack tip, thus cracking along these planes occur.

The adsorption-induced dislocation emission (AIDE) is a mechanism proposed for the first time in 1976 and further developed by Lynch [72, 90, 96, 97], which implies a dislocation nucleation facilitated by the external hydrogen adsorbed at the crack surface followed by dislocations movement away from the crack tip under stress. Thus, the adsorbed hydrogen acts by weakening the interatomic bonds in the substrate and facilitates the dislocations' emission [90].

The hydrogen-enhanced strain-induced vacancy formation mechanism (HESIV) is the mechanism in which hydrogen slightly enhances homogenous dislocation nucleation, however it promotes dislocation emission, induces slip planarity, and localizes dislocation activity significantly, leading to locally enhanced vacancy formation from dislocations [107]. Some studies have reported that the hydrogen-enhanced localized dislocation activity and vacancy formation is the main reason of hydrogen embrittlement in metals and alloys [107-109].

A recently proposed mechanism is the DEFACTANT model by Kirchheim [110-113]. The term is a shortcut from "DEFect ACTing AGEnts" which refers to solute atoms that segregates to material defects and is proposed in analogy to the concept of surfactants (SURFace ACTing AGEnts). The concept is based on thermodynamic calculations and refers to hydrogen atoms as defactants that reduce the formation energy of defects. The concept equations were used

for interpreting nanoindentation results and it was shown how the hydrogen affects the energy barrier for homogeneous dislocation nucleation [50, 52, 112, 114, 115].

In the recent years, the synergistic interplay between multiple mechanisms (e.g. HELP+HEDE and HELP-mediated HEDE) has been proposed in several works, which can explain and model some hydrogen embrittlement cases successfully [99, 116].

3. MATERIALS AND SAMPLE PREPARATION

This PhD thesis focuses on two types of materials: a dual phase 25%Cr super duplex stainless steel and a 316L austenitic stainless steel. The chemical composition of the investigated steels are given in Table 1, while the heat treatments of the samples are given in Table 2.

Table 1 Chemical composition of the selected steels

	C	Si	Mn	S	P	Cr	Ni	W	Mo	Cu	N	Al
SDSS	0.017	0.23	0.51	0.001	0.027	24.92	7.31	0.53	3.6	0.60	0.253	0.005
316L	0.015	0.38	1.25	0.0005	0.027	16.39	10.16	-	2.09	-	0.04	-

Table 2 Heat treatment applied to the selected samples

	Heat treatment	Temp., °C	Time	Cooling
SDSS	Annealing	1130	7 hours	Water quenching
316L	Annealing	1150	8 days	In furnace

The heat treatments applied to the samples resulted in coarse grain microstructures with a very low dislocation density. The samples were cut 10 mm in thickness and 10 - 12 mm in diameter to fit the electrochemical cell. To achieve an average roughness of the sample's surface of less than 10 nm, the samples were grinded with silicon-carbide papers up to 2400 grade, polished mechanically with a water-based diamond suspension and to remove the microscopic layer affected by mechanical polishing [51] the samples were electropolished using the parameters presented in Table 3.

Table 3 Electropolishing parameters

	Electrolyte	Pot., V	Flow rate	Time, s	Temp., °C
SDSS	Methanol/H ₂ SO ₄	35	12	30	21
316L	Methanol/H ₂ SO ₄	20	12	30	21

To exclude the phase and crystallographic orientation effect on the results, Scanning Electron Microscope and Electron Back Scattering Diffraction (EBSD) mapping was done on selected areas on the sample's surface. Figure 3 and Figure 4 give information about the crystal lattice as well as crystallographic orientation of the grains. From these images, specific grains were

selected for performing the nanoindentation tests. Two microindents (marked as MI) were performed on each sample, close enough to the selected grains for easier identification, deep enough to be visible with the optical camera of the nanoindenter but far away enough from the investigated areas so the plastic deformation around them does not affect the tested grains (marked with NI in Figure 3b) and Figure 4).

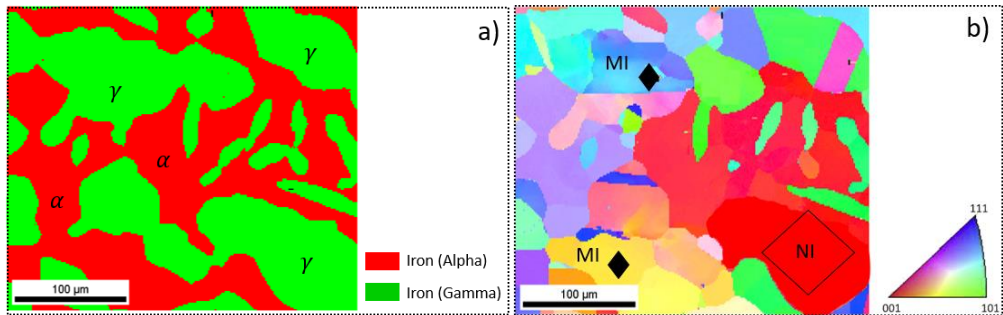


Figure 3 SDSS sample a) phase map, where red is the ferrite and green is the austenite; b) inverse pole figure map revealing the crystallographic orientation of the grains

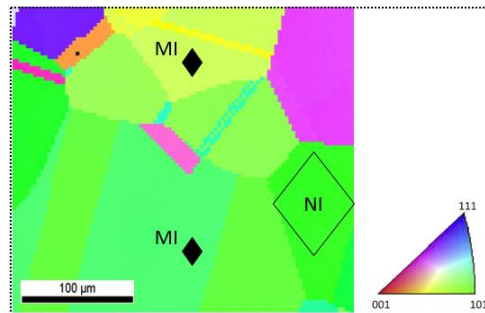


Figure 4 Austenitic 316L SS inverse pole figure map

4. EXPERIMENTAL TECHNIQUES

During this PhD thesis, several experimental methods have been used. These are described in the following sections.

4.1. Electrochemical nanoindentation (ECNI)

Electrochemical nanoindentation, shortly refer to as ECNI, is a method developed rather recently to investigate the effect of hydrogen on the micromechanical properties of different materials under hydrogen charging conditions [50, 51]. The experimental setup involves using a tribo indenter in combination with an electrochemical setup and the immediate effect of hydrogen on local material micro-constituents can be recorded. The main advantage of using in situ ECNI technique for investigating the hydrogen effect is that it ensures a constant hydrogen source during testing, while in the case of ex-situ ECNI, a large amount of hydrogen diffuses out of the material when the sample is transferred from the electrochemical setup to the nanoindentation setup [117].

This PhD thesis implemented the ECNI setup for the first time at the Norwegian University of Science and Technology (NTNU) and it is schematically shown in Figure 5 [118-120]. An electrochemical cell set up was incorporated in a nanoindenter (Tribo Indenter TI 950 from Hysitron, now Bruker), and a Gamry Reference 600™ Potentiostat was used to control the electrode potentials. The electrolyte with a pH of 6.22 was prepared dissolving Na₂SO₄ (99%, Merck KGaA) in deionised water (18.2 MΩ·cm) at a concentration of 0.05 mol/L.

The Tribo Indenter TI 950 is able to perform both indentations and scanning probe images of the sample's surface. The indentation technique generates load - displacement curves (LD) when an indenter tip is pushed into the sample surface with loads from nano to micro Newton levels. From these LD curves generated the material properties are calculated, like hardness, reduced elastic modulus, as well as it can capture the first dislocation nucleation (pop in).

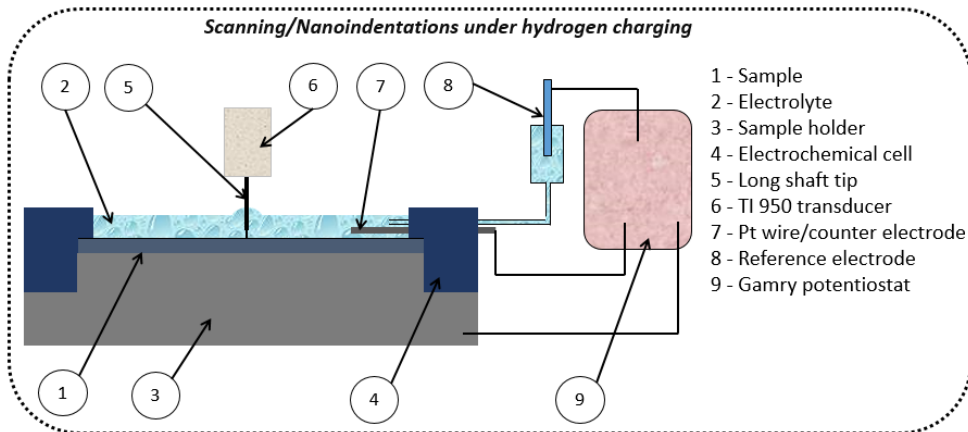


Figure 5 Experimental setup for in-situ ECNI testing

Different types of indenters can be used and the difference is given by the shape of its tips, which can be spherical, pyramidal, conical, cylindrical or cube-corner with the shape of a three-sided pyramid also known as the Berkovich indenters [121]. Berkovich type indenters' tips were used in this study.

The TI 950 equipment shown in Figure 6, is equipped with an optical camera, a transducer and the sample stage. The electrochemical setup is placed on the sample stage and the system can be operated in six directions ($\pm X$, $\pm Y$ and $\pm Z$) to position the sample under the optical camera. The system can be switched between the optical position mode and contact mode, when the tip indenter approaches and gets in contact with the sample.

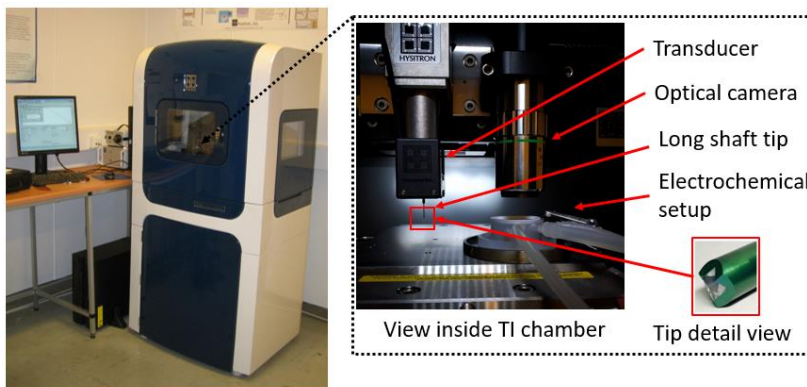


Figure 6 View inside the Tribo Indenter TI 950

Maximum forces of 2000 μN were used to perform indentations during this PhD thesis which gave material information at a sub-micron level, thus they will be referred to as nanoindentations [122]. During nanoindentation a tip is approaching slowly to the sample and is applying a defined load or displacement to the sample, Figure 7a), and the load-displacement curve produced, Figure 7b), is used to calculate the material properties like hardness and the reduced modulus of elasticity.

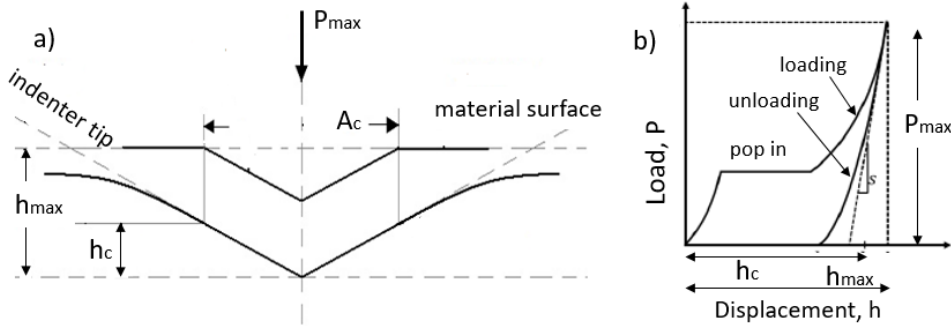


Figure 7 a) Cross-sectional area of an indentation, b) typical load – displacement curve

The hardness is calculated based on the maximum load applied to the sample, P_{max} , and the contact area, A_c :

$$H = \frac{P_{max}}{A_c} \quad \text{Equation 8}$$

The contact area, A_c , is calculated from the tip area function based on the contact depth, h_c . For a perfect Berkovich indenter [123]:

$$A_c = 24.5 \cdot h_c^2 \quad \text{Equation 9}$$

$$h_c = h_{max} - \varepsilon \frac{P_{max}}{S} \quad \text{Equation 10}$$

The contact depth, h_c , is extracted from the maximum displacement, h_{max} , material stiffness, S , and a geometric constant, ε equal to 0.75.

The reduced modulus of elasticity is calculated from the material stiffness, contact area and a correction factor, β which depends on the tip geometry ($\beta = 1.034$ for a Berkovich indenter):

$$E_r = \frac{\sqrt{\pi}}{2} \frac{1}{\beta} \frac{S}{\sqrt{A_c}} \quad \text{Equation 11}$$

There is an interconnected relation between the reduced modulus and the elastic modulus and that depends on the Poisson's ratios for the sample, ν_s , respectively indenter, ν_i , as well as on both elastic modulus of the sample, E_s , respectively indenter, E_i :

$$\frac{1}{E_r} = \frac{1 - \nu_s^2}{E_s} + \frac{1 - \nu_i^2}{E_i} \quad \text{Equation 12}$$

4.2. Focused Ion Beam (FIB) microscopy

The focused ion beam (FIB) microscopy is used in materials' studies and has the same principle as a scanning electron microscope (SEM), except that is using an ion beam instead of an electron one. FIB is capable of high-resolution imaging, patterning, precise micromachining and deposition in one single unit [20, 49, 59, 124-127].

A FIB system is comprising a vacuum system, a gas injection system, a liquid metal ion source responsible for producing the ion beam, sample stage and a computer that controls the equipment. The ion source is usually made of gallium (Ga), due to its properties like low melting point (29.8 °C), high surface tension, low vapour pressure and long lifetime.

The FIB system used in this study was a Helios NanoLab™ DualBeam™ produced by FEI (now ThermoFisher) and it is shown schematically in Figure 8. The system has a SEM column along the FIB column thus, the electron beam was used to perform the imaging while the FIB column was used to perform milling. Inside the chamber there is a pressure lower than 2.6×10^{-6} mbar and the stage can move in five axes (x, y, x, rotational and tilt axis). The physical and thermal stability of the stage is important to perform accurate positioning and to avoid the specimen drift. This combined FIB–SEM system can perform advanced characterisation and produce complex shapes for further material investigations.

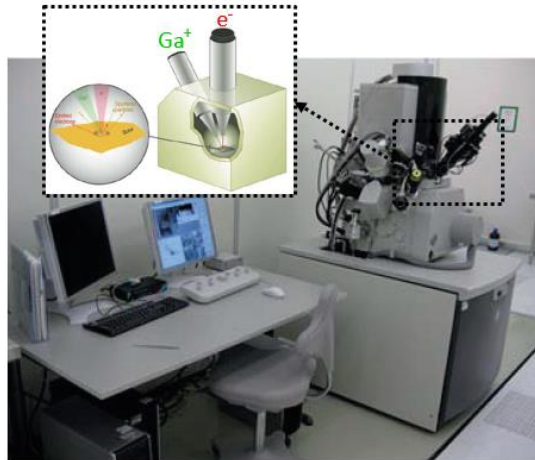


Figure 8 Picture of the Helios NanoLab™ DualBeam™ system with a schematic detail of the ion beam and electron beam interacting with the surface

When a Ga^+ ion hits the sample surface and collides with the surface atoms, different amounts of material can be removed, depending on the angle of incidence, Figure 9.

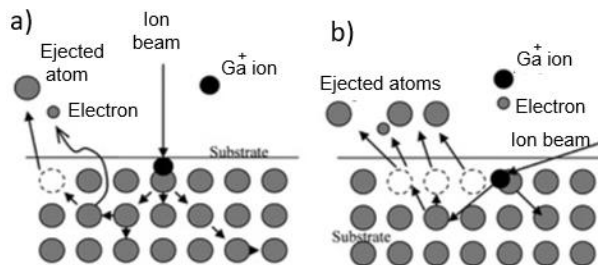


Figure 9 Interaction between an ion beam with a solid surface gives a) less material removal or b) more material removal on larger angles of incidence [124]

Although the ion beam - sample interactions are essential in the FIB application, the ions' effect on the sample material can cause damages including atomic sputtering, ion emission, localized heating and ion implantation in the sample surface. It is highly important to elucidate these side effects when using FIB for characterization, examination and sample preparation in materials science; for example, micro-compression testing of pillars [53, 126-128], 3D tomography of microstructure [57, 129], studying the crack interaction with the grain boundary [130, 131], preparation of TEM and atom probe tomography samples [132, 133].

FIB was used in this PhD thesis to investigate the chemically induced phase transformation of austenite to ferrite due to Gallium implantation.

4.3. Scanning Electron Microscope - Electron Backscatter Diffraction mapping (SEM-EBSD)

Scanning Electron Microscope - Electron Backscatter Diffraction (SEM-EBSD) technique provides microstructural crystallographic characterization of materials [58, 79, 134] revealing phases on surfaces, grain orientations as well as grain sizes, local texture and point-to-point orientation correlations.

A phosphor screen is situated within the SEM chamber to detect the electrons which are accelerated by the electron beam and diffracted by the atomic layers in a crystalline sample [135]. During characterization, the diffracted electrons will hit the phosphor screen and generate Kikuchi patterns known as EBSD patterns, which are giving information about the structure and crystallographic orientation of the grains. The intensity of the generated Kikuchi patterns increases with surface inclination, thus the sample surface is tilted approximately 70° relative to normal incidence of the electron beam, Figure 10.

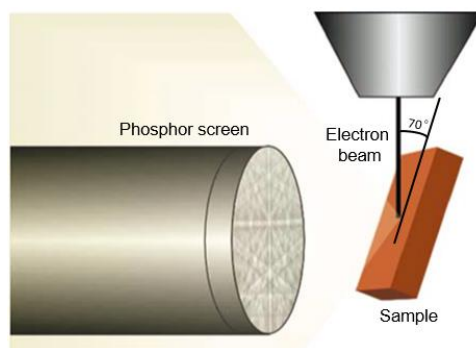


Figure 10 Schematic illustration of the EBSD principle. Adapted from [135]

The equipment used to generate the EBSD maps of the samples in this PhD thesis was a field emission SEM (FESEM), Zeiss Ultra 55 VP. The EBSD patterns were acquired with a high speed NORDIF UF750 camera system, and for indexing and data analysis a TSL OIM software was

used. While the sample was tilted 70° and placed on a working distance of 21 mm, the acceleration voltage inside the chamber was 30 kV.

The EBSD patterns resulting from the electron beam – sample interaction were indexed in different types of maps: the material phase map (which gives information about the identified phase in each measurement point), the inverse pole figure (IPF) map (also known as the crystallographic orientation map), the confidence index (CI) map (which gives the quality of indexing the diffraction pattern at each point) and the image quality (IQ) map. In addition to these standard methods, orientation gradient mapping (OGM) analysis was also used to analyse the lattice misorientation calculated with respect to its neighbouring points [136].

5. MAIN RESULTS

5.1. Oxygen Argon plasma effect on hydrogen uptake in steels

As explained in Chapter 3, the sample preparation for testing is done in several steps. During experimental trials for investigating the hydrogen effect on stainless steels, it was observed and proposed a new method for controlling the hydrogen uptake into samples when applying cathodic protection. Two samples, one SDSS and one 316L ASS, freshly electropolished, were tested first in air and afterwards under hydrogen charging. The tests were repeated on the same samples treated for 5 minutes with Oxygen Argon plasma (OArP) prior testing and Figure 11 shows that the hydrogen effect is suppressed under electrochemically hydrogen charging. The treatment applied does not affect the dislocation nucleation during ECNI, Figure 11, neither the nanomechanical properties of the materials, Figure 12, but it greatly inhibited the hydrogen uptake when the surfaces were electrochemically charged. Topography images made on 316L sample show no differences on the pile ups around nanoindentations made prior and after OArP treatment, Figure 14. Also Figure 15 shows the topography images made on SDSS sample and a clear effect of hydrogen on austenitic grain is shown by the slip lines captured after only 85 minutes of hydrogen charging on a freshly electropolished sample, while no slip lines are observed on the OArP treated sample not even after 6 hours of hydrogen charging [137].

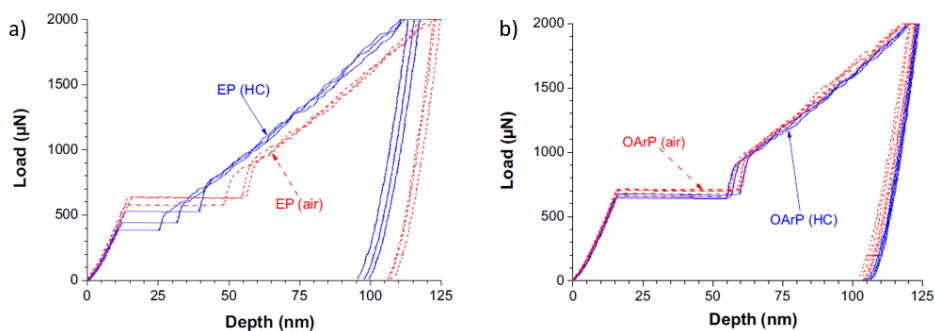


Figure 11 Load - displacement curves resulted from in situ electrochemical nanoindentations made on 316L ASS, first in air and later under hydrogen charging (HC) on a) freshly electropolished sample and b) 5 min OArP treated sample

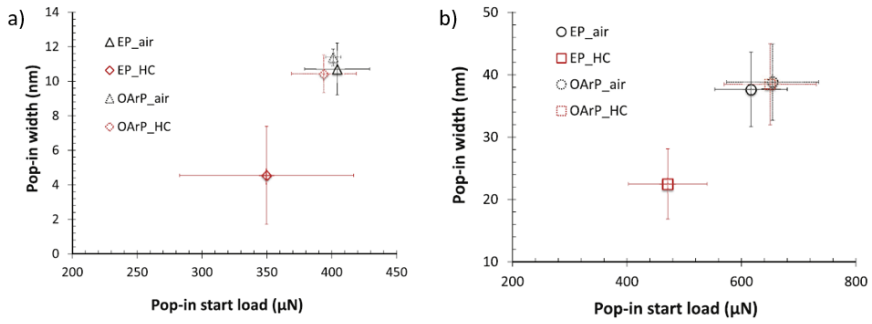


Figure 12 Pop-in behaviour with the error bars representing the standard deviation, a) austenitic phase of SDSS, b) 316L ASS

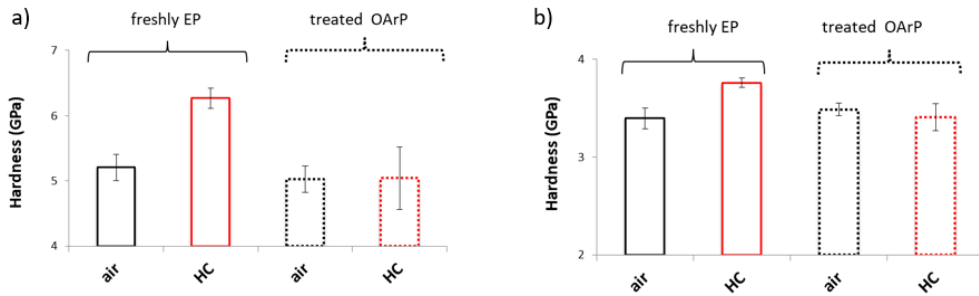


Figure 13 Hardness behaviour with the error bars representing the standard deviation, a) austenitic phase of SDSS, b) 316L ASS

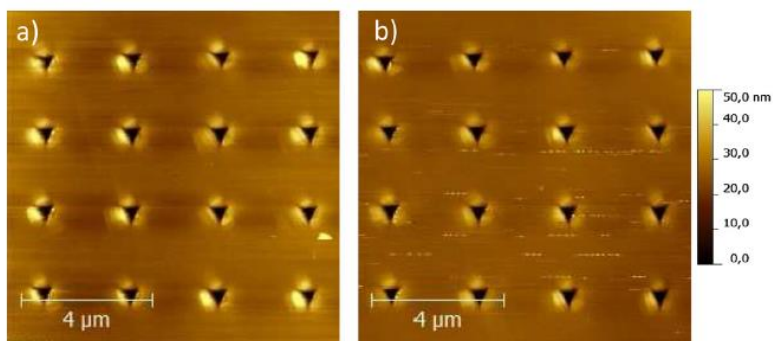


Figure 14 SPM topography images after nanoindentation of a 316L sample under hydrogen charging a) pre- and b) post-OArP treatment

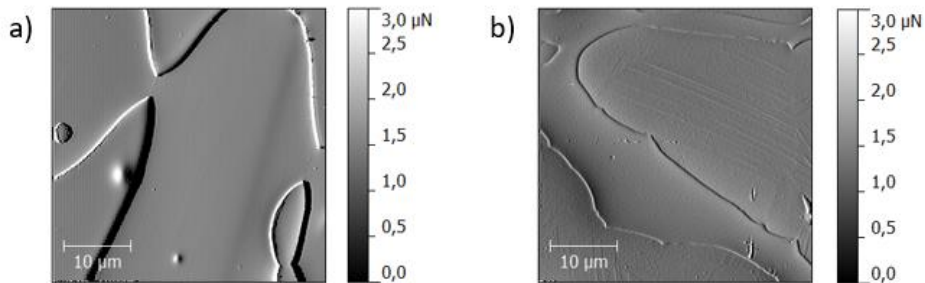


Figure 15 SDSS sample a) imaged after 6 hour of hydrogen charging on a sample treated for 5 minutes with OArP, b) slip lines captured in austenitic grain after 85 minutes of hydrogen charging on a freshly electropolished sample (without OArP treatment)

5.2. Hydrogen effect on the nanomechanical properties of SDSS and 316L ASS

Using ECNI, the hydrogen effect on the nanomechanical properties and dislocation nucleation was investigated in both SDSS and 316L ASS. Under hydrogen charging a reduction in the pop in load and width was reported on both austenitic and ferritic phases of a SDSS sample, Figure 16 and Figure 17, as well as an increase in hardness, Figure 18.

Hydrogen effect on the material hardness is larger for the austenitic phase than for the ferritic one, with a difference before and after hydrogen charging, of approximately 1 GPa for austenite and only 0.6 GPa for ferrite. The higher increase in the hardness under hydrogen charging for the austenite is attributed to the fact that austenite has a higher solubility of hydrogen than ferrite [138].

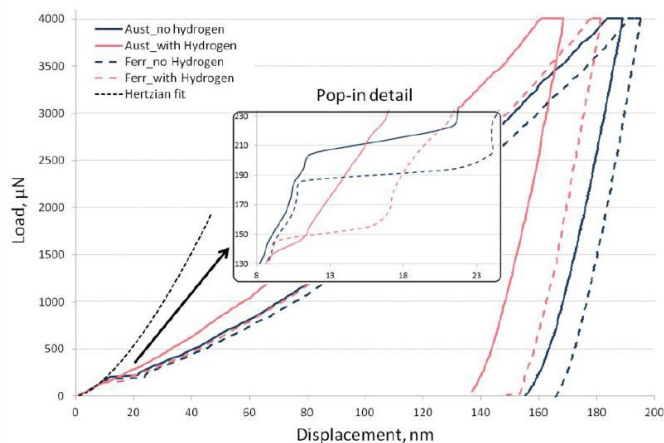


Figure 16 The reduction in the onset of plasticity (pop-in load level) due to hydrogen on SDSS

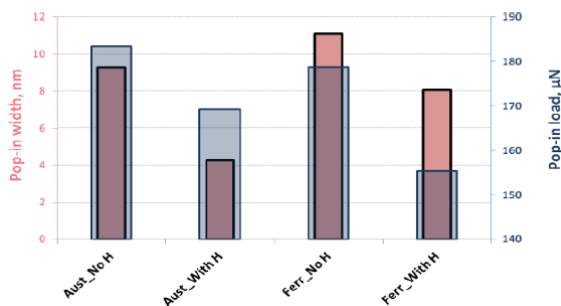


Figure 17 Pop-in width and pop-in load from the pop-in analysis

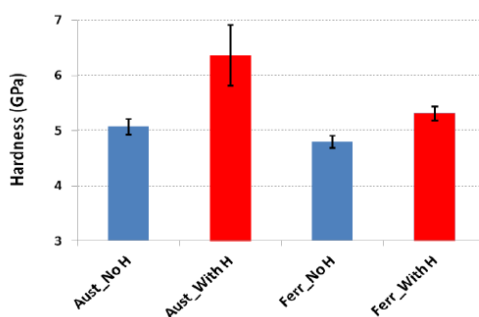


Figure 18 The hydrogen effect on the SDSS sample hardness

On austenitic 316L SS, it was investigated the interconnection of the electrode potential of the sample with the hydrogen effect on the nanomechanical properties. It was found that more positive cathodic potentials have a softening effect, while applying more negative cathodic potentials a significant hardening can be observed.

There is a clear difference in the LD curves under hydrogen charging, the curves are similar in air and under anodic potentials (AP), Figure 19. While at different cathodic potentials (CPs), both the pop-in load and pop-in width are decreasing with increasing of the cathodic charging, Figure 20. The sample recovers under anodic polarization, Figure 21. From the scanning probe microscopy (SPM) images made after each set of nanoindentations, Figure 21b, it can be concluded that the changes in the material behaviour are due to the dissolved hydrogen and not to the changes in the surface conditions.

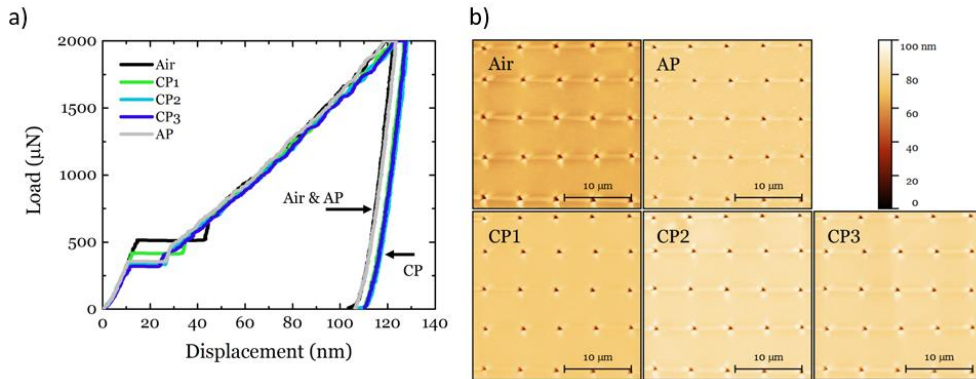


Figure 19 a) Representative LD curves for 316L SS in different charging potentials and b) the corresponding SPM images, where CP1=-740mV, CP2=-808mV, CP3=-884mV and AP=+100mV

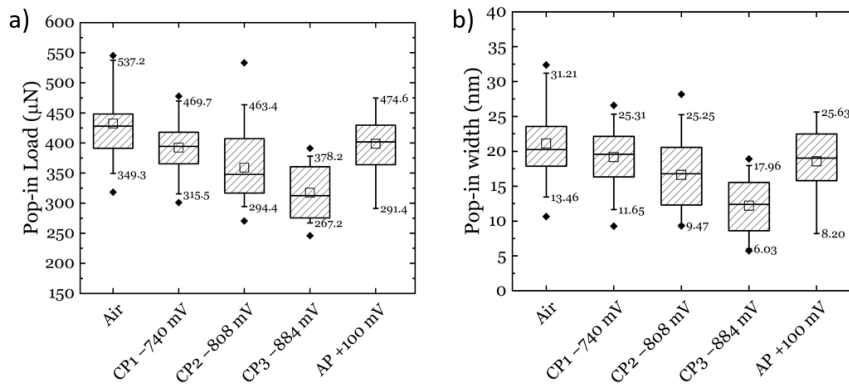


Figure 20 Pop-in data from the ECNI of a 316L sample under different charging conditions: a) pop-in load; b) pop-in width

Hydrogen has a huge effect on the nanomechanical properties, like hardness and reduced modulus, Figure 21. By decreasing further the cathodic potentials (CPs) to -1200 mV and -1400 mV, the hardness increases systematically and abruptly when the cathodic potential of -1500 mV is reached, Figure 21 c). Also, the SPM image shows the formation of slip lines and/or martensite formation on the surface [139].

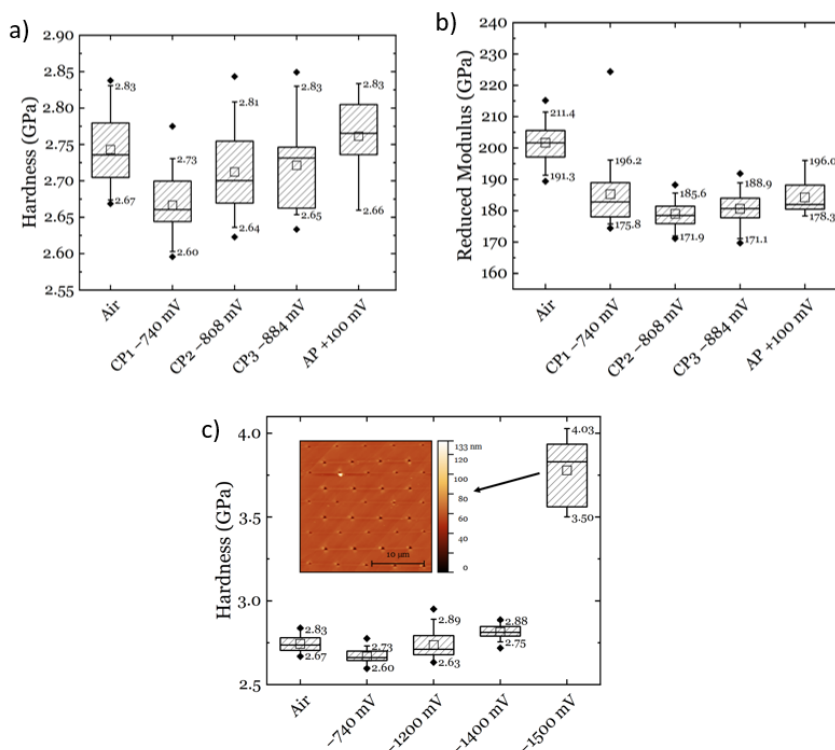


Figure 21 Hydrogen effect on nanomechanical properties of 316L sample: a) hardness and b) reduced modulus on low cathodic potentials, c) hardness on high cathodic potentials

During material testing the phase transformation was triggered not only during hydrogen charging but it was also observed when other elements, like gallium, were implanted into the surface. During FIB, which is an intensively used method nowadays for creating testing samples, like pillars for example, it was found a chemically induced austenitic-to-ferritic phase transformation under gallium ions. In an independent test, several regions were milled under FIB using 3 different gallium ion doses at different acceleration voltages. The phase transformation occurred within the milled areas. Both high resolution electron backscatter diffraction analysis Figure 22, and chemical analysis of the affected areas showed that the gallium implantation preceded the FIB milling and the phase transformation was not triggered by the shear and plastic deformation expected from the typical martensitic transformation. By increasing locally the amount of gallium, which is a ferrite stabilizer, the chemical composition of the austenite was changed, and this resulted in the selective transformation of austenite to ferrite [140].

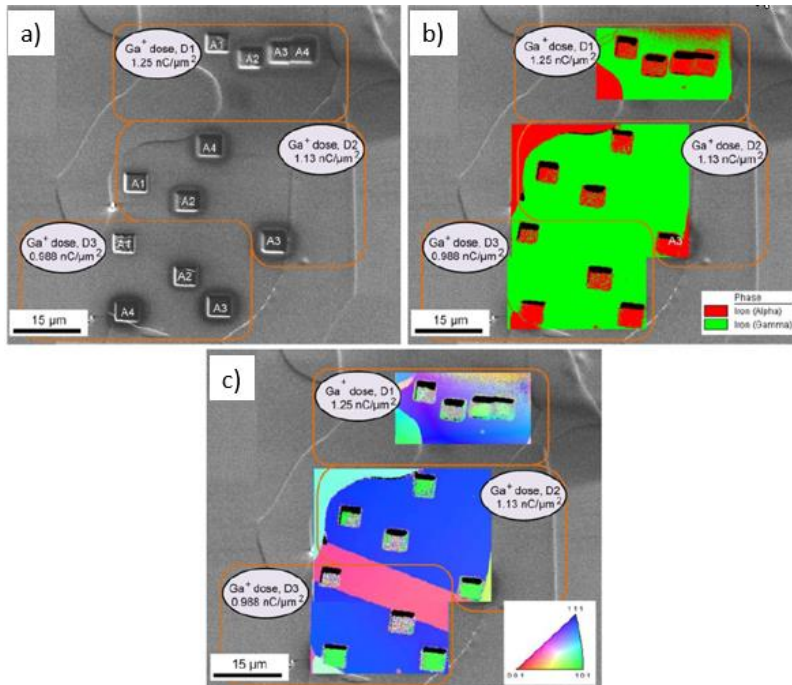


Figure 22 FIB milled areas in an austenite grain of SDSS sample: a) SEM image of all the patterns milled with different parameters; b) phase map where green is austenite and red is ferrite, c) IPF map showing the change in the crystallographic orientation of the grains after milling.

6. SUMMARY OF PAPERS

This chapter presents the papers that were published and presented in conferences during the PhD thesis, while APPENDICES chapter comprises the papers.

Paper I: Oxygen argon plasma treatment effect on hydrogen uptake in austenitic stainless steels

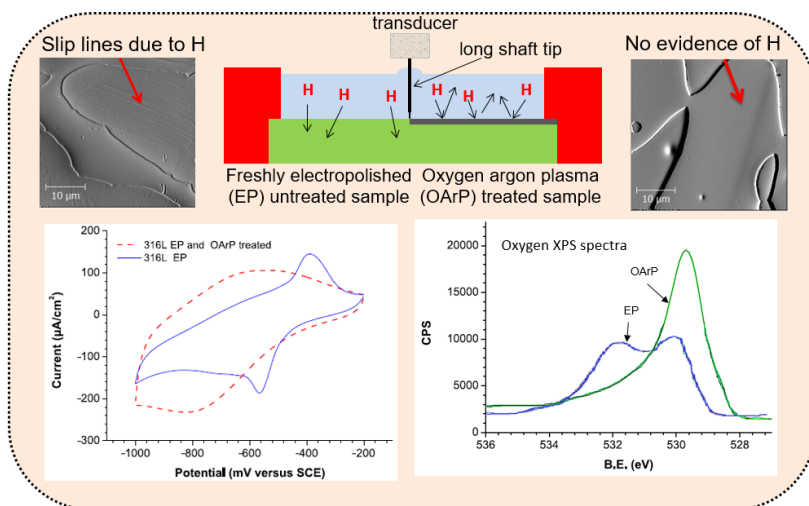
Authors: Afrooz Barnoush, ***Adina Basa*** and Christian Thaulow.

Published in: International Journal of Hydrogen Energy, 2014, 39(26), 14120–14131.

<https://doi.org/10.1016/j.ijhydene.2014.06.161>

Abstract: In this study, oxygen argon plasma (OArP) treatment was introduced as a new method for controlling hydrogen uptake in austenitic stainless steels during cathodic protection. It was determined that a 5-min treatment with OArP did not affect the nanomechanical properties of the material or the dislocation nucleation process, but it greatly inhibited the effect of hydrogen when the surfaces were in situ electrochemically hydrogen charged. Moreover, the cyclic voltammetry and X-ray photoelectron spectroscopy tests showed that the applied treatment influenced the composition of the surface oxide which in turn influences the hydrogen uptake from the surface.

Graphical abstract:



Paper II: An In-Situ Electrochemical Nanoindentation (ECNI) Study on the Effect of Hydrogen on the Mechanical Properties of 316L Austenitic Stainless Steel

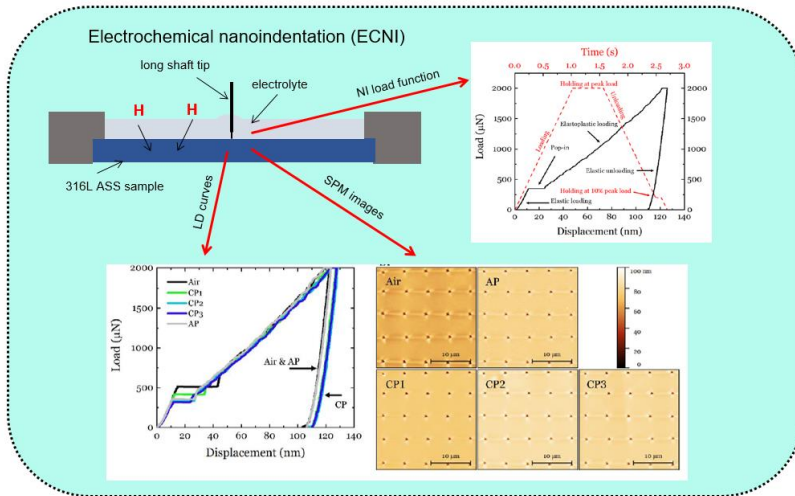
Authors: Adina Basa, Dong Wang, Nuria Espallargas and Di Wan

Published in Materials, 2021, 14(21), 6426,

<https://doi.org/10.3390/ma14216426>

Abstract: In-situ electrochemical nanoindentation (ECNI) has been used to study the effect of hydrogen on the mechanical properties of austenitic stainless steel AISI 316L. Changing the electrode potential (via electrochemical charging) revealed the interconnected nature of the hydrogen effect on the nanomechanical properties of the stainless steel. At more positive cathodic potentials, a softening effect of hydrogen can be noticed, while significant hardening can be observed at more negative cathodic potentials. The hydrogen effects on the nanomechanical properties were analysed in terms of the homogeneous dislocation nucleation (HDN) and the hydrogen-dislocation interactions from the energy point of view. The effects can be explained with the framework of the defactant theory and the hydrogen-enhanced localized plasticity (HELP) mechanism.

Graphical abstract:



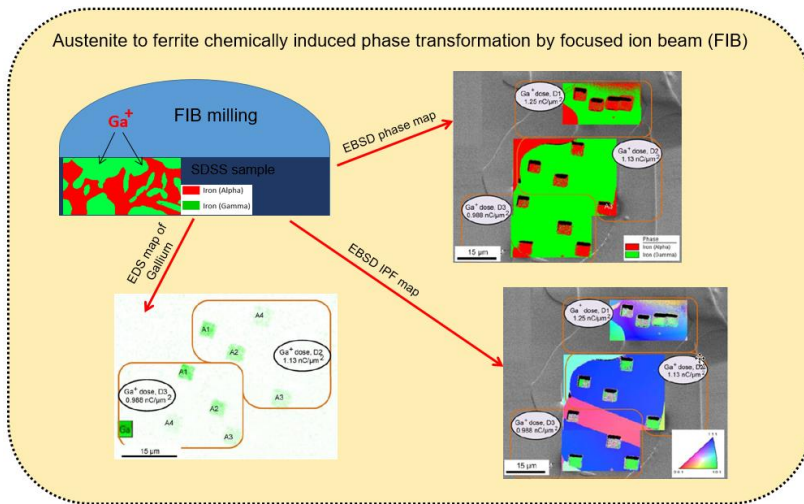
Paper III: Chemically induced phase transformation in austenite by focused ion beam

Authors: **Adina Basa**, Christian Thaulow and Afrooz Barnoush.

Published in: Metallurgical and Materials Transactions A, 2014, 45(3), 1189–1198.

<https://doi.org/10.1007/s11661-013-2101-4>

Abstract: A highly stable austenite phase in a super duplex stainless steel was subjected to a combination of different gallium ion doses at different acceleration voltages. It was shown that contrary to what is expected, an austenite to ferrite phase transformation occurred within the focused ion beam (FIB) milled regions. Chemical analysis of the FIB milled region proved that the gallium implantation preceded the FIB milling. High resolution electron backscatter diffraction analysis also showed that the phase transformation was not followed by the typical shear and plastic deformation expected from the martensitic transformation. On the basis of these observations, it was concluded that the change in the chemical composition of the austenite and the local increase in gallium, which is a ferrite stabilizer, results in the local selective transformation of austenite to ferrite.

Graphical abstract:**Conferences presentations/publications**

In addition, the PhD candidate have contributed in the conference presentations and articles listed beneath. The presenting author is underlined.

- **Conference presentation: In situ nanoindentation testing of hydrogen degradation on super duplex stainless steel.**

Authors: Adina Basa, Christian Thaulow and Vigdis Olden.

Conference: International Conference on Steel and Hydrogen; September 28 – 29, 2011, Ghent, Belgium

Abstract: The effect of hydrogen on mechanical properties of super duplex stainless steel was studied using a nanoindenter equipment combined with an electrochemical setup so the nanoindentations can be made on an electrochemically charged surface. In situ electrochemical nanoindentation testing captures the change in the onset of

plasticity (pop-in load level) as well as the change in hardness due to absorption of atomic hydrogen.

- **Conference paper: Nanomechanical testing of hydrogen effects on super duplex stainless steel.**

Authors: Adina Basa, Afroz Barnoush and Christian Thaulow.

Published in: International Conference Diagnosis and Prediction in Mechanical Systems Engineering; May 31 – June 1, 2012, Galati, Romania. Mechanical Testing and Diagnosis, ISSN 2247-9635, 2012 (II), Volume 2, pp. 5–14 (Conference presentation and paper)

Abstract: The effect of hydrogen on the mechanical properties of the super duplex stainless steel is examined using in situ electrochemical nanoindentation (ECNI) tests. Within the ECNI, which is a nanoindenter combined with an electrochemical setup, the nanoindentation can be made on a surface that is immersed in an electrolyte and in situ electrochemically charged with hydrogen. In situ electrochemical nanoindentation testing captures the change in the onset of plasticity (pop-in load level) as well as the change in the hardness due to the absorption of the atomic hydrogen.

7. CONCLUSIONS AND FURTHER WORK

In this PhD thesis the hydrogen interaction with two stainless steels, one austenitic and one super duplex stainless steel, was investigated. The tests were performed within the same grains, first in air, and then under electrochemical charging with hydrogen by applying cathodic potentials and discharging when applying anodic potential. The following conclusions can be drawn:

- Hydrogen has a clear effect on both hardness and the pop-ins of both the austenite and the ferrite phases of the super duplex steel as well as on the austenitic steel.
- The cathodically charged hydrogen promotes the homogeneous dislocation nucleation during nanoindentation in samples (316L ASS and SDSS), which was explained by the framework of the defactant theory.
- A softening effect of hydrogen was observed at cathodic potentials up to the redox potential for hydrogen evolution on the austenitic stainless steel sample (316L ASS), which was explained by the HELP mechanism. When charging the sample at higher cathodic potentials (more negative), hydrogen-induced surface steps (slip lines) are observed, which contribute to permanent changes in the material microstructure.
- After oxygen argon plasma treatment of the two materials (316L ASS and SDSS), the nanomechanical properties of the surfaces in air did not change. Also, the effect on hardness and pop-in load induced by electrochemically charged hydrogen at cathodic polarization was not observed for the oxygen argon plasma treated samples. The clear inhibition of hydrogen induced hardening and reduction in the pop-in load after oxygen argon plasma treatment proved that this treatment prevents hydrogen uptake into the metal.
- Hydrogen is not the only element that triggers a phase transformation. Gallium implantation into a highly stable austenite phase in a SDSS was observed to spark the austenite to ferrite phase transformation. Further analysis proved that the phase transformation was not followed by plastic deformation or an increase in the dislocation density, but it is a transformation triggered by local changes in the chemical composition of the steel.

Some of the work started in this thesis was continued by other PhD candidates at NTNU during the years I was not formally a PhD student in the department anymore (2013-2021), however there is still a need for further investigations. The effect of hydrogen on different types of materials is intensively reported in literature, both internationally and resulted from NTNU, but the candidate would like to point out that there is still a huge need for:

- Investigating the effect of other gases/chemical elements on the nanomechanical properties of stainless steels.
- Investigating barriers for hydrogen uptake, which delay or even cancel the deleterious effect that hydrogen has on the materials.
- Finding and investigating desorption methods for hydrogen or proposing hydrogen traps for the steels used for, for example, hydrogen transport applications.

8. REFERENCES

1. Barrera, O., et al., *Understanding and mitigating hydrogen embrittlement of steels: a review of experimental, modelling and design progress from atomistic to continuum*. Journal of Materials Science, 2018. 53(9): p. 6251-6290.
2. Lacombe, P., *Stainless steels*. Les Ulis: Les Editions de Physique, 1993: p. 403-434.
3. Townsend, H., *Effects of alloying elements on the corrosion of steel in industrial atmospheres*. Corrosion, 2001. 57(6): p. 497-501.
4. Wan, J., Y. Lou, and H. Ruan, *The partition coefficient of alloying elements and its influence on the pitting corrosion resistance of 15Cr-2Ni duplex stainless steel*. Corrosion Science, 2018. 139: p. 13-20.
5. Lu, Y., M. Ives, and C. Clayton, *Synergism of alloying elements and pitting corrosion resistance of stainless steels*. Corrosion Science, 1993. 35(1-4): p. 89-96.
6. Bhadeshia, H.K.D.H., *Prevention of Hydrogen Embrittlement in Steels*. ISI International, 2016. 56(1): p. 24-36.
7. Brück, S., et al., *Hydrogen Embrittlement Mechanism in Fatigue Behavior of Austenitic and Martensitic Stainless Steels*. Metals, 2018. 8: p. 339.
8. Chan, W., C. Kwok, and K. Lo, *Mechanical Properties and Hydrogen Embrittlement of Laser-Surface Melted AISI 430 Ferritic Stainless Steel*. Coatings, 2020. 10(2): p. 140.
9. Costa, L.R.O., L.F. Lemus, and D.S. dos Santos, *Hydrogen embrittlement susceptibility of welded 2¼Cr-1Mo steel under elastic stress*. International Journal of Hydrogen Energy, 2015. 40(47): p. 17128-17135.
10. Robertson, I.M., et al., *Hydrogen Embrittlement Understood*. Metallurgical and Materials Transactions B, 2015. 46(3): p. 1085-1103.
11. Ferreira, P.J., I.M. Robertson, and H.K. Birnbaum, *Hydrogen effects on the interaction between dislocations*. Acta Materialia, 1998. 46(5): p. 1749-1757.
12. Oriani, R.A., *Hydrogen embrittlement of steels*. Ann. Rev. Mater. Sci., 1978. 8: p. 327-57.
13. Johnson, W.H., *On Some Remarkable Changes Produced in Iron and Steel by the Action of Hydrogen and Acids*. Proceedings of the Royal Society of London, 1875. 23: p. 168-179.
14. Olden, V., Thaulow, C., Johnsen, R., *Modelling of hydrogen diffusion and hydrogen induced cracking in supermartensitic and duplex stainless steels*. Materials & Design, 2008. 29(10): p. 1934-1948.
15. Zakroczymski, T. and E. Owczarek, *Electrochemical investigation of hydrogen absorption in a duplex stainless steel*. Acta Mater., 2002. 50(10): p. 2701-2713.
16. McNabb, A. and P. Foster, *A new analysis of the diffusion of hydrogen in iron and ferritic steels*. Trans. Metall. Soc. AIME, 1963. 227(3): p. 618-627.
17. Pauzon, C., et al., *Effect of argon and nitrogen atmospheres on the properties of stainless steel 316 L parts produced by laser-powder bed fusion*. Materials & Design, 2019. 179: p. 107873.

18. Dietrich, K., et al., *The influence of oxygen on the chemical composition and mechanical properties of Ti-6Al-4V during laser powder bed fusion (L-PBF)*. Additive Manufacturing, 2020. 32: p. 100980.
19. Gaspard, V., et al., *Hydrogen effect on dislocation nucleation in a ferritic alloy Fe-15Cr as observed per nanoindentation*. Materials Science and Engineering: A, 2014. 604: p. 86-91.
20. Hajilou, T., et al., *In situ small-scale hydrogen embrittlement testing made easy: An electrolyte for preserving surface integrity at nano-scale during hydrogen charging*. International Journal of Hydrogen Energy, 2018. 43(27): p. 12516-12529.
21. Okada, K., et al., *Crystallographic feature of hydrogen-related fracture in 2Mn-0.1C ferritic steel*. International Journal of Hydrogen Energy, 2018. 43(24): p. 11298-11306.
22. Cui, T.C., Liu, P. F., Gu, C. H., *Finite element analysis of hydrogen diffusion/plasticity coupled behaviors of low-alloy ferritic steel at large strain*. International Journal of Hydrogen Energy, 2017. 42(31): p. 20324-20335.
23. Kim, S.J., *Effect of the elastic tensile load on the electrochemical corrosion behavior and diffusible hydrogen content of ferritic steel in acidic environment*. International Journal of Hydrogen Energy, 2017. 42(30): p. 19367-19375.
24. Malitckii, E., et al., *Hydrogen effects on mechanical properties of 18%Cr ferritic stainless steel*. Materials Science and Engineering: A, 2017. 700: p. 331-337.
25. Yin, L., et al., *Effect of hydrogen charging conditions on hydrogen blisters and pitting susceptibility of 445J1M ferritic stainless steel*. Journal of The Electrochemical Society, 2018. 165(16): p. C1007.
26. Marshall, P., *Austenitic stainless steels: microstructure and mechanical properties*. 1984: Springer Science & Business Media.
27. Bak, S., M. Abro, and D. Lee, *Effect of Hydrogen and Strain-Induced Martensite on Mechanical Properties of AISI 304 Stainless Steel*. Metals, 2016. 6(7): p. 169.
28. Han, G., et al., *Effect of strain-induced martensite on hydrogen environment embrittlement of sensitized austenitic stainless steels at low temperatures*. Acta Materialia, 1998. 46(13): p. 4559-4570.
29. Hayashi, N., et al., *Phase transformation in He+ and H+ ion irradiated type 304 stainless steel*. Hyperfine Interact., 1988. 42(1-4): p. 989-992.
30. Kim, Y.S., S.H. Bak, and S.S. Kim, *Effect of Strain-Induced Martensite on Tensile Properties and Hydrogen Embrittlement of 304 Stainless Steel*. Metallurgical and Materials Transactions A, 2016. 47(1): p. 222-230.
31. Nilsson, J.O., *Super duplex stainless steels*. Mater. Sci. Technol., 1992. 8(8): p. 685-700.
32. Oltra, R., C. Bouillot, and T. Magnin, *Localized hydrogen cracking in the austenitic phase of a duplex stainless steel*. Scripta Mater., 1996. 35(9): p. 1101-1105.
33. Johnsen, R., et al., *New improved method for HISC testing of stainless steels under cathodic protection*, in *Corrosion 2007*, NACE International: Nashville, Tennessee.
34. Olden, V., Thaulow, C., Johnsen, R., Østby, E., Berstad, T., *Influence of hydrogen from cathodic protection on the fracture susceptibility of 25%Cr duplex stainless steel - Constant load SENT testing and FE-modelling using hydrogen influenced cohesive zone elements*. Engineering Fracture Mechanics, 2009. 76(7): p. 827-844.
35. Olden, V., et al., *Cohesive zone modeling of hydrogen-induced stress cracking in 25% Cr duplex stainless steel*. Scripta Materialia, 2007. 57(7): p. 615-618.
36. Lula, R., *Duplex stainless steels*. R. A. Lula, Ed. 775 pages. American Society for Metals, Metals Park, Ohio, 1983. ASM members, \$ 55. 20, 1983.

37. Szummer, A., E. Jezierska, and K. Lublińska, *Hydrogen surface effects in ferritic stainless steels*. Journal of Alloys and Compounds, 1999. 293-295: p. 356-360.
38. Abraham, D.P. and C.J. Altstetter, *The effect of hydrogen on the yield and flow stress of an austenitic stainless steel*. Metallurgical and Materials Transactions A, 1995. 26(11): p. 2849-2858.
39. Silverstein, R. and D. Eliezer, *Effects of residual stresses on hydrogen trapping in duplex stainless steels*. Materials Science and Engineering A, 2017. 684: p. 64-70.
40. Silverstein, R., D. Eliezer, and B. Glam, *Hydrogen Effect on Duplex Stainless Steels at Very High Strain Rates*. Energy Procedia, 2017. 107: p. 199-204.
41. Silverstein, R. and D. Eliezer, *Mechanisms of hydrogen trapping in austenitic, duplex, and super martensitic stainless steels*. Journal of Alloys and Compounds, 2017. 720: p. 451-459.
42. Sobol, O., et al., *Novel approach to image hydrogen distribution and related phase transformation in duplex stainless steels at the sub-micron scale*. International Journal of Hydrogen Energy, 2017. 42(39): p. 25114-25120.
43. Wang, D., et al., *In-situ observation of martensitic transformation in an interstitial metastable high-entropy alloy during cathodic hydrogen charging*. Scripta Materialia, 2019. 173: p. 56-60.
44. Wang, D., et al., *Effect of hydrogen-induced surface steps on the nanomechanical behavior of a CoCrFeMnNi high-entropy alloy revealed by in-situ electrochemical nanoindentation*. Intermetallics, 2019. 114: p. 106605.
45. Chou, S.-L. and W.-T. Tsai, *Effect of grain size on the hydrogen-assisted cracking in duplex stainless steels*. Materials Science and Engineering: A, 1999. 270(2): p. 219-224.
46. Liang, X.Z., et al., *Hydrogen embrittlement in super duplex stainless steels*. Materialia, 2020. 9: p. 100524.
47. Depover, T., et al., *The effect of hydrogen on the crack initiation site of TRIP-assisted steels during in-situ hydrogen plasma micro-tensile testing: Leading to an improved ductility?* Materials Characterization, 2020. 167: p. 110493.
48. Deng, Y. and A. Barnoush, *Hydrogen embrittlement revealed via novel in situ fracture experiments using notched micro-cantilever specimens*. Acta Materialia, 2018. 142: p. 236-247.
49. Rogne, B.R.S., et al., *In situ micromechanical testing in environmental scanning electron microscope: A new insight into hydrogen-assisted cracking*. Acta Materialia, 2018. 144: p. 257-268.
50. Barnoush, A. and H. Vehoff, *In situ electrochemical nanoindentation: A technique for local examination of hydrogen embrittlement*. Corrosion Science, 2008. 50(1): p. 259-267.
51. Barnoush, A. and H. Vehoff, *Electrochemical nanoindentation: A new approach to probe hydrogen/deformation interaction*. Scripta Mater., 2006. 55(2): p. 195-198.
52. Wang, D., et al., *Effect of hydrogen on nanomechanical properties in Fe-22Mn-0.6C TWIP steel revealed by in-situ electrochemical nanoindentation*. Acta Materialia, 2019. 166: p. 618-629.
53. Barnoush, A., et al., *Examination of hydrogen embrittlement in FeAl by means of in situ electrochemical micropillar compression and nanoindentation techniques*. Intermetallics, 2010. 18(7): p. 1385-1389.
54. Deng, Y., et al., *Functional materials under stress: In situ TEM observations of structural evolution*. Advanced materials, 2020. 32(27): p. 1906105.

55. Jiang, S.-y., et al., *Stress-induced martensite phase transformation of FeMnSiCrNi shape memory alloy subjected to mechanical vibrating polishing*. Transactions of Nonferrous Metals Society of China, 2020. 30(6): p. 1582-1593.
56. Vardiman, R.G. and I.L. Singer, *Transformation of stress-induced martensite in 304 stainless steel by ion implantation*. Mater. Lett., 1983. 2(2): p. 150-154.
57. Raabe, D., et al., *3D EBSD: Tomographic orientation microscopy in a FIB SEM*. E-MRS Strassbourg,, 2010.
58. Perret, J., et al., *EBSD, SEM and FIB characterisation of subsurface deformation during tribocorrosion of stainless steel in sulphuric acid*. Wear, 2010. 269(5–6): p. 383-393.
59. Rogne, B.R.S., C. Thaulow, and A. Barnoush, *Micromechanical Testing of Fracture Initiation Sites in Welded High-Strength Low-Alloy Steel*. Metallurgical and Materials Transactions A, 2014. 45(4): p. 1996-2003.
60. Yang, Y., et al., *Evaluating the effects of pillar shape and gallium ion beam damage on the mechanical properties of single crystal aluminum nanopillars*. Journal of Materials Research, 2021: p. 1-14.
61. Djukic, M.B., et al., *Hydrogen damage of steels: A case study and hydrogen embrittlement model*. Engineering Failure Analysis, 2015. 58: p. 485-498.
62. Djukic, M.B., et al., *Hydrogen Embrittlement of Industrial Components: Prediction, Prevention, and Models*. CORROSION, 2016. 72(7): p. 943-961.
63. Hack J. E., L.G.R., *The influence of microstructure on the susceptibility of titanium alloys to internal hydrogen embrittlement*. Metallurgical Transactions A, Volume 13, Issue 10, pp 1729–1738, 1982.
64. Richard L. S. Thomas, J.R.S., Richard P. Gangloff, *Internal hydrogen embrittlement of ultrahigh-strength AERMET 100 steel*. Metallurgical and Materials Transactions A, Volume 34, Issue 2, pp 327–344, 2003.
65. Tiwari, G.P., et al., *A study of internal hydrogen embrittlement of steels*. Materials Science and Engineering: A, 2000. 286(2): p. 269-281.
66. Walter, R.J., R.P. Jewett, and W.T. Chandler, *On the mechanism of hydrogen-environment embrittlement of iron- and nickel-base alloys*. Materials Science and Engineering, 1970. 5(2): p. 99-110.
67. Michler, T., et al., *Influence of macro segregation on hydrogen environment embrittlement of SUS 316L stainless steel*. International Journal of Hydrogen Energy, 2009. 34(7): p. 3201-3209.
68. Michler, T. and J. Naumann, *Coatings to reduce hydrogen environment embrittlement of 304 austenitic stainless steel*. Surface and Coatings Technology, 2009. 203(13): p. 1819-1828.
69. Nelson, H.G., D.P. Williams, and J.E. Stein, *Environmental hydrogen embrittlement of an α - β titanium alloy: Effect of microstructure*. Metallurgical and Materials Transactions B, 1972. 3(2): p. 473-479.
70. Liu, C.T., *Environmental embrittlement and grain-boundary fracture in Ni sub 3 Al*. Scripta Metallurgica et Materialia; (United States), 1992: p. Medium: X; Size: Pages: 25-28.
71. Beachem, C.D., *A new model for hydrogen-assisted cracking (hydrogen "embrittlement")*. Metallurgical and Materials Transactions B, 1972. 3(2): p. 441-455.
72. Lynch, S.P., *A fractographic study of hydrogen-assisted cracking and liquid-metal embrittlement in nickel*. Journal of Materials Science, 1986. 21(2): p. 692-704.

73. McEvily, A.J. and I. Le May, *Hydrogen-assisted cracking*. Materials Characterization, 1991. 26(4): p. 253-268.
74. Frandsen, J.D. and H.L. Marcus, *The correlation between grain size and plastic zone size for environmental hydrogen assisted fatigue crack propagation*. Scripta Metallurgica, 1975. 9(10): p. 1089-1094.
75. Marrow, T.J., P.J. Cotterill, and J.E. King, *Temperature effects on the mechanism of time independent hydrogen assisted fatigue crack propagation in steels*. Acta Metallurgica et Materialia, 1992. 40(8): p. 2059-2068.
76. Tsay, L.W., J.J. Chen, and J.C. Huang, *Hydrogen-assisted fatigue crack growth of AISI 316L stainless steel weld*. Corrosion Science, 2008. 50(11): p. 2973-2980.
77. Takakuwa, O. and H. Soyama, *Suppression of hydrogen-assisted fatigue crack growth in austenitic stainless steel by cavitation peening*. International Journal of Hydrogen Energy, 2012. 37(6): p. 5268-5276.
78. Holobut, P., *Random hydrogen-assisted fatigue crack growth in steel plates*. Probabilistic Engineering Mechanics, 2011. 26(1): p. 61-66.
79. Brown I.H. , C.W.L., Ghomashchi R, *Application of SEM-EBSD for Measurement of Plastic Strain Fields associated with Weld Metal Hydrogen Assisted Cold Cracking* Proceedings of the 2012 9th International Pipeline Conference 2012.
80. Kurji, R. and N. Coniglio, *Towards the establishment of weldability test standards for hydrogen-assisted cold cracking*. The International Journal of Advanced Manufacturing Technology, 2015. 77(9): p. 1581-1597.
81. Magudeeswaran, G., V. Balasubramanian, and G. Madhusudhan Reddy, *Hydrogen induced cold cracking studies on armour grade high strength, quenched and tempered steel weldments*. International Journal of Hydrogen Energy, 2008. 33(7): p. 1897-1908.
82. Takahashi A., O.H., *Influence of Microhardness and Inclusion on Stress Oriented Hydrogen Induced Cracking of Line Pipe Steels*. ISIJ International, volume 36, p. 334-340 1996.
83. Takahashi A., O.H., *Influence of Softened Heat-affected Zone on Stress Oriented Hydrogen Induced Cracking of a High Strength Line Pipe Steel*. ISIJ International, volume 35, p. 1190-1195, 1995.
84. Al-Anezi, M.A., G.S. Frankel, and A.K. Agrawal, *Susceptibility of Conventional Pressure Vessel Steel to Hydrogen-Induced Cracking and Stress-Oriented Hydrogen-Induced Cracking in Hydrogen Sulfide-Containing Diglycolamine Solutions*. CORROSION, 1999. 55(11): p. 1101-1109.
85. Lu, X., et al., *Effect of electrochemical charging on the hydrogen embrittlement susceptibility of alloy 718*. Acta Materialia, 2019. 179: p. 36-48.
86. Depover, T., et al., *Assessment of the potential of hydrogen plasma charging as compared to conventional electrochemical hydrogen charging on dual phase steel*. Materials Science and Engineering: A, 2019. 754: p. 613-621.
87. Depover, T. and K. Verbeken, *The effect of TiC on the hydrogen induced ductility loss and trapping behavior of Fe-C-Ti alloys*. Corrosion Science, 2016. 112: p. 308-326.
88. Depover, T., E. Van den Eeckhout, and K. Verbeken, *Hydrogen induced mechanical degradation in tungsten alloyed steels*. Materials Characterization, 2018. 136: p. 84-93.
89. Depover, T. and K. Verbeken, *Hydrogen trapping and hydrogen induced mechanical degradation in lab cast Fe-C-Cr alloys*. Materials Science and Engineering: A, 2016. 669: p. 134-149.

90. Lynch, S., *Hydrogen embrittlement phenomena and mechanisms*. Corros Rev 30, 2012.
91. Bhatia, B. and D.S. Sholl, *Chemisorption and diffusion of hydrogen on surface and subsurface sites of flat and stepped nickel surfaces*. The Journal of Chemical Physics, 2005. 122(20): p. 204707.
92. Myers, S.M., Baskes, M. I., Birnbaum, H. K., Corbett, J. W., DeLeo, G. G., Estreicher, S. K., Haller, E. E., Jena, P., Johnson, N. M., Kirchheim, R., Pearton, S. J., Stavola, M. J., *Hydrogen interactions with defects in crystalline solids*. Reviews of Modern Physics, 1992. 64(2): p. 559-617.
93. Wan, D., *Hydrogen-Assisted Fatigue Crack Growth in Ferritic Steels*. 2019.
94. Carter, T.J. and L.A. Cornish, *Hydrogen in metals*. Engineering Failure Analysis, 2001. 8(2): p. 113-121.
95. Chai, G., et al., *Mechanisms of hydrogen induced stress crack initiation and propagation in super duplex stainless steels*. steel research international, 2009. 80(7): p. 482-487.
96. Lynch, S., *Mechanisms of hydrogen assisted cracking—a review*. Hydrogen effects on material behaviour and corrosion deformation interactions, 2003: p. 449-466.
97. Lynch, S.P., *Metallographic contributions to understanding mechanisms of environmentally assisted cracking*. Metallography, 1989. 23(2): p. 147-171.
98. Kirchheim, R., *On the solute-defect interaction in the framework of a defactant concept*. Int. J. Mater. Res., 2009. 4(4): p. 483-487.
99. Djukic, M.B., et al., *The synergistic action and interplay of hydrogen embrittlement mechanisms in steels and iron: Localized plasticity and decohesion*. Engineering Fracture Mechanics, 2019. 216: p. 106528.
100. Vehoff, H., *Hydrogen related material problems, Hydrogen in Metals III*, H. Wipf, Editor. 1997, Springer Berlin / Heidelberg. p. 215-278.
101. Birnbaum, H.K., *Mechanical properties of metal hydrides*. Journal of the Less Common Metals, 1984. 104(1): p. 31-41.
102. Wasim, M., M.B. Djukic, and T.D. Ngo, *Influence of hydrogen-enhanced plasticity and decohesion mechanisms of hydrogen embrittlement on the fracture resistance of steel*. Engineering Failure Analysis, 2021. 123: p. 105312.
103. Nagao, A., et al., *Hydrogen-enhanced-plasticity mediated decohesion for hydrogen-induced intergranular and “quasi-cleavage” fracture of lath martensitic steels*. Journal of the Mechanics and Physics of Solids, 2018. 112: p. 403-430.
104. Troiano, A.R., *The role of hydrogen and other interstitials in the mechanical behaviour of metals*. Trans ASM; 52:54-80, 1960.
105. Oriani, R.A., *The diffusion and trapping of hydrogen in steel*. Acta Metallurgica, 1970. 18(1): p. 147-157.
106. Birnbaum, H.K. and P. Sofronis, *Hydrogen-enhanced localized plasticity—a mechanism for hydrogen-related fracture*. Materials Science and Engineering: A, 1994. 176(1-2): p. 191-202.
107. Wen, M., et al., *Hydrogen-enhanced dislocation activity and vacancy formation during nanoindentation of nickel*. Physical Review B, 2009. 80(9): p. 094113.
108. Szost, B.A. and P.E.J. Rivera-Díaz-del-Castillo, *Unveiling the nature of hydrogen embrittlement in bearing steels employing a new technique*. Scripta Materialia, 2013. 68(7): p. 467-470.

109. Nagumo, M., T. Yagi, and H. Saitoh, *Deformation-induced defects controlling fracture toughness of steel revealed by tritium desorption behaviors*. Acta Materialia, 2000. 48(4): p. 943-951.
110. Kirchheim, R., *Reducing grain boundary, dislocation line and vacancy formation energies by solute segregation. I. Theoretical background*. Acta Mater., 2007. 55(15): p. 5129-5138.
111. Kirchheim, R., *Reducing grain boundary, dislocation line and vacancy formation energies by solute segregation: II. Experimental evidence and consequences*. Acta Mater., 2007. 55(15): p. 5139-5148.
112. Kirchheim, R., *Revisiting hydrogen embrittlement models and hydrogen-induced homogeneous nucleation of dislocations*. Scripta Materialia, 2010. 62(2): p. 67-70.
113. Kirchheim, R. and A. Pundt, *25 - Hydrogen in Metals*, in *Physical Metallurgy (Fifth Edition)*, D.E. Laughlin and K. Hono, Editors. 2014, Elsevier: Oxford. p. 2597-2705.
114. Barnoush, A. and H. Vehoff, *Recent developments in the study of hydrogen embrittlement: Hydrogen effect on dislocation nucleation*. Acta Materialia, 2010. 58(16): p. 5274-5285.
115. Barnoush, A., M. Zamanzade, and H. Vehoff, *Direct observation of hydrogen-enhanced plasticity in super duplex stainless steel by means of in situ electrochemical methods*. Scripta Materialia, 2010. 62(5): p. 242-245.
116. Novak, P., et al., *A statistical, physical-based, micro-mechanical model of hydrogen-induced intergranular fracture in steel*. Journal of the Mechanics and Physics of Solids, 2010. 58(2): p. 206-226.
117. Barnoush, A., *Hydrogen embrittlement, revisited by in situ electrochemical nanoindentation*. PhD Dissertation, 2008.
118. Basa, A., C. Thaulow, and V. Olden, *In situ nanoindentation testing of hydrogen degradation on super duplex stainless steel*. Steely Hydrogen Conf. Proc., 2011: p. 157-166.
119. Asgari, M., et al., *Microstructural characterization of pulsed plasma nitrided 316L stainless steel*. Mater. Sci. Eng. A, 2011. 529(0): p. 425-434.
120. Asgari, M., et al., *Nanomechanical evaluation of the protectiveness of nitrided layers against hydrogen embrittlement*. Corros. Sci., 2012. 62(0): p. 51-60.
121. Hysitron, *TI-750 Ubi User Manual NRL-M-201 r9.0.0609 (TriboScan 9.1)*. 2009.
122. A., F.C., *Nanoindentation*. 2002.
123. Oliver W.C. and Pharr G.M., *An improved technique for determining hardness and elastic modulus*. J. Mater. Res., 1992. 7(6).
124. Bhavsar, S.N., S. Aravindan, and P.V. Rao, *Machinability study of cemented carbide using focused ion beam (FIB) milling*. Materials and Manufacturing Processes, 2012. 27(10): p. 1029-1034.
125. McCarthy, J., et al., *FIB micromachined submicron thickness cantilevers for the study of thin film properties*. Thin Solid Films, 2000. 358(1): p. 146-151.
126. Uchic, M.D. and D.M. Dimiduk, *A methodology to investigate size scale effects in crystalline plasticity using uniaxial compression testing*. Mater. Sci. Eng., A,, 2005. 400-401(0): p. 268-278.
127. Volkert, C.A. and A.M. Minor, *Focused Ion Beam Microscopy and Micromachining*. MRS Bull., 2007. 32: p. 389-399.
128. Kheradmand, N., A. Barnoush, and H. Vehoff, *Investigation of the role of grain boundary on the mechanical properties of metals*. J. Phys.: Conf. Ser., 2010. 240.

129. Zaefferer, S., S.I. Wright, and D. Raabe, *Three-Dimensional Orientation Microscopy in a Focused Ion Beam–Scanning Electron Microscope: A New Dimension of Microstructure Characterization*. Metall. Mater. Trans. A,, 2008. 39(2): p. 374-389.
130. Holzapfel, C., et al., *Interaction of cracks with precipitates and grain boundaries: Understanding crack growth mechanisms through focused ion beam tomography*. Scr. Mater., 2007. 56(8): p. 697-700.
131. Schaef, W., et al., *A 3-D view on the mechanisms of short fatigue cracks interacting with grain boundaries*. Acta Mater., 2011. 59(5): p. 1849-1861.
132. Lozano-Perez, S., *A guide on FIB preparation of samples containing stress corrosion crack tips for TEM and atom-probe analysis*. Micron,, 2008. 39(3): p. 320-328.
133. Kuwano, S., et al., *TEM sample preparation for microcompressed nanocrystalline Ni*. Mater. Trans., 2008. 49(9): p. 2091-2095.
134. Maitland, T. and S. Sitzman, *Electron backscatter diffraction (EBSD) technique and materials characterization examples*. Vol. 14. 2007: Springer Berlin.
135. Schwarzer, R.A., et al., *Present State of Electron Backscatter Diffraction and Prospective Developments*, in *Electron Backscatter Diffraction in Materials Science*, A.J. Schwartz, et al., Editors. 2009, Springer US: Boston, MA. p. 1-20.
136. Henning, M. and H. Vehoff, *Local mechanical behavior and slip band formation within grains of thin sheets*. Acta Mater., 2005. 53(5): p. 1285-1292.
137. Barnoush, A., A. Basa, and C. Thaulow, *Oxygen argon plasma treatment effect on hydrogen uptake in austenitic stainless steels*. International journal of hydrogen energy, 2014. 39(26): p. 14120-14131.
138. Basa, A., C. Thaulow, and A. Barnoush. *Nanomechanical testing of hydrogen effect on super duplex stainless steel*. in *Intern. Conf. Diagnosis and Prediction in Mechanical Engineering Systems, DIPRE'12*. 2012. Galati, Romania.
139. Basa, A., et al., *An In-Situ Electrochemical Nanoindentation (ECNI) Study on the Effect of Hydrogen on the Mechanical Properties of 316L Austenitic Stainless Steel*. Materials, 2021. 14(21): p. 6426.
140. Basa, A., C. Thaulow, and A. Barnoush, *Chemically induced phase transformation in austenite by focused ion beam*. Metallurgical and Materials Transactions A, 2014. 45(3): p. 1189-1198.

9. APPENDICES

PAPER I

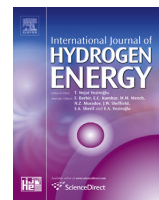
***Oxygen argon plasma treatment effect on hydrogen uptake in
austenitic stainless steels***



ELSEVIER

Available online at www.sciencedirect.com

ScienceDirect

journal homepage: www.elsevier.com/locate/he

Oxygen argon plasma treatment effect on hydrogen uptake in austenitic stainless steels

Afroz Barnoush^{*}, Adina Basa, Cristian Thaulow

Department of Engineering Design and Materials, Norwegian University of Science and Technology, No 7491 Trondheim, Norway

ARTICLE INFO

Article history:

Received 9 December 2013

Received in revised form

25 June 2014

Accepted 30 June 2014

Available online 25 July 2014

Keywords:

Stainless steel

Cyclic voltammetry

XPS

Hydrogen embrittlement

Nanoindentation

Passive films

ABSTRACT

In this study, oxygen argon plasma (OArP) treatment was introduced as a new method for controlling hydrogen uptake in austenitic stainless steels during cathodic protection. It was determined that a 5-min treatment with OArP did not affect the nanomechanical properties of the material or the dislocation nucleation process, but it greatly inhibited the effect of hydrogen when the surfaces were in situ electrochemically hydrogen charged. Moreover, the cyclic voltammetry and X-ray photoelectron spectroscopy tests showed that the applied treatment influenced the composition of the surface oxide which in turn influences the hydrogen uptake from the surface.

Copyright © 2014, Hydrogen Energy Publications, LLC. Published by Elsevier Ltd. All rights reserved.

Introduction

Super duplex stainless steels (SDSS) and austenitic stainless steels (ASS) are widely used in many industrial applications because of their cost efficiency, high mechanical properties, and good stress corrosion cracking resistance. However, under appropriate conditions they can undergo hydrogen embrittlement [1–9]. Specifically, within the sub-sea applications where due to the cathodic protection a continuous source of hydrogen exist on the surface [10]. It is known that SDSS can often fail due to hydrogen being released during cathodic protection, leading to hydrogen embrittlement (HE) [11–15].

In the presence of an external hydrogen source, such as hydrogen transportation pipelines or sub-sea pipelines under cathodic protection, one possible approach for controlling HE is to inhibit the uptake of hydrogen from the surface. Hydrogen uptake is a complicated process that happens through different steps depending on the source of the hydrogen i.e. gaseous or electrochemical. In the case of electrochemical hydrogen, hydrogen uptake involves the whole steps within the hydrogen evolution reaction as well as atomic hydrogen absorption on the surface and its diffusion through the different phases which are present on the surface [6,16]. The rate of hydrogen uptake is controlled by the kinetic of the slowest step involved. For a given alloy, the most convenient way to reduce the rate of hydrogen uptake is by modification

^{*} Corresponding author.

E-mail addresses: afroz.barnoush@ntnu.no, afroz.barnoush@gmail.com (A. Barnoush), adina.basa@ntnu.no (A. Basa), christian.thaulow@ntnu.no (C. Thaulow).

<http://dx.doi.org/10.1016/j.ijhydene.2014.06.161>

0360-3199/Copyright © 2014, Hydrogen Energy Publications, LLC. Published by Elsevier Ltd. All rights reserved.

Table 1 – Chemical composition of materials investigated in this study (wt%).

	C	Si	Mn	S	P	Cr	Ni	W	Mo	Cu	N	Al
SDSS	0.017	0.23	0.51	0.001	0.027	24.92	7.31	0.53	3.6	0.6	0.253	0.005
316L	0.015	0.38	1.25	0.0005	0.027	16.39	10.16	–	2.09	–	0.04	–

of its surface. This can be done by surface treatment which alters the kinetic of hydrogen evolution on the surface and/or formation of a surface film with a very low diffusivity for hydrogen. For example, studies have shown that a pulsed plasma nitride layer reduces the hydrogen uptake [17–21] while at the same time enhances the mechanical properties in presence of the hydrogen [21–23]. The exact mechanism of how the hydrogen uptake through nitriding is reduced, is not clear yet. Primary studies shows that the nitriding mainly affects the transportation and the solubility of the hydrogen on the surface layer [18]. In a recent study, Izawa et al. showed that the oxide film on the surface of the ASS can alter its mechanical behaviour in hydrogen atmosphere [24].

Recently, electrochemical nanoindentation (ECNI) technique [25–32], has been extensively used to study the effect of hydrogen on mechanical properties [26,33,34]. The ECNI method provides a rapid possibility to evaluate the hydrogen effect on the nanomechanical properties in a relatively small sample with a high statistics. In comparison to the conventional mechanical testing methods for hydrogen embrittlement e.g. tensile test in hydrogen atmosphere, ECNI is simpler, cheaper and material-conservative. As an example we can refer to the Zamanzade et al. work on evaluation of the hydrogen effect on nanomechanical properties of intermetallic iron aluminide alloys with different Cr concentration [35,36]. Within a similar experimental approach in this study, we examined the hydrogen effect on naomechanical properties of two different austenitic phases: austenite phase of 25% Cr SDSS (UNS S32760) and 316L ASS, with two different surface treatments. An oxygen argon plasma (OArP) is used to alter the freshly electropolished (EP) surface of the both steels, and the subsequent changes in mechanical properties are studied by means of nanoindentation in both hydrogen charged and uncharged conditions. The surface compositional changes and electrochemical properties are studied using X-ray photoelectron spectroscopy (XPS) and cyclic voltammetry (CV).

Materials and methods

Materials and sample preparation

The chemical compositions of EN1.4501 (UNS S32760) SDSS and 316L ASS are presented in Table 1. The heat treatments were applied to the samples according to Table 2, which resulted in microstructures with a very low dislocation

density and coarse grains. The dimensions of the samples used were 1 mm–2 mm in thickness and 12 mm in diameter for SDSS and 10.6 mm in diameter for 316L. The preparation of the samples began by grinding with silicon-carbide papers up to 2400 grade, followed by mechanical polishing with a water-based diamond suspension up to 1 μm . The final step was electropolishing using the parameters presented in Table 3 to remove the microscopic work-hardened layer of material caused by mechanical polishing [37].

Methods

Oxygen–argon plasma treatment

The OArP treatment was performed with Fishione 1020 PC equipment. The freshly EP samples were treated for 5 min with a mixture of 25% oxygen and 75% argon. This treatment was originally developed for cleaning hydrocarbon contamination from SEM samples. An oscillating electromagnetic field accelerates free electrons to high velocities and the excited gas atoms create the plasma. The energies with which plasma ions collide on the surface are less than 12eV, which is below the typical sample sputtering threshold. The same treatment with the same parameters was applied to both the SDSS and 316L samples.

Electron backscatter diffraction mapping

A low vacuum field emission SEM (LV-FESEM), Zeiss Supra 95 VP was used for electron backscatter diffraction (EBSD) mapping of the samples prior testing, and TSL OIM software was used for the data analysis. The samples were tilted by 70°, the acceleration voltage was 30 kV, the working distance was 21 mm and a step size of 200 nm was used for EBSD mapping. Fig. 1(a) presents the phase map of SDSS and Fig. 1(b and c) presents the inverse pole figure maps which give information regarding the grain orientations of both SDSS and 316L samples respectively. To exclude the crystallographic orientation effect, all sets of nanoindentations were performed within the same grain. In the SDSS sample, an austenite grain orientated close to the (001) plane was tested, while a grain orientated close to the (101) plane was investigated in the 316L sample, as indicated by the straight arrows in Fig. 1(b and c). The selection of these orientations made based on availability of large size grain with low index close to the centre of the sample for ease of performing in situ electrochemical nanoindentation. For easier identification of these grains, each sample was marked with several microindents (dotted arrows) where the

Table 2 – Heat treatments applied to materials.

	Heat treatment	Temp. (°C)	Time	Cooling
SDSS	Annealing	1130	7 h	Water quenching
316L [21]	Annealing	1150	8 days	In furnace

Table 3 – Parameters used for electropolishing.

	Electrolyte	Pot. (V)	Flow rate	Time (s)	Temp. (°C)
SDSS	Methanol/H ₂ SO ₄	35	12	30	21
316L	Methanol/H ₂ SO ₄	20	12	30	21

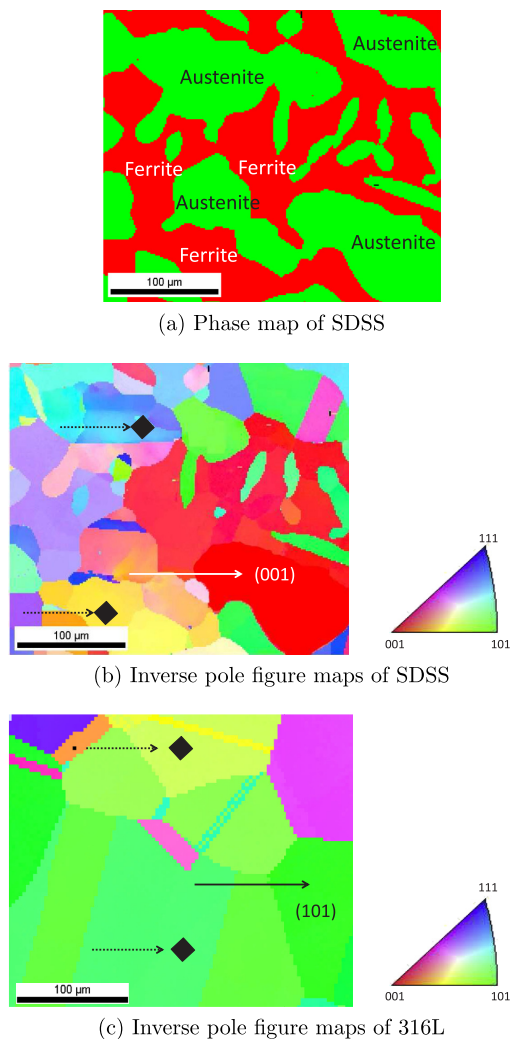


Fig. 1 – EBSD characterisation of materials studied: (a) phase map of SDSS, where green is the austenite phase (γ) and red is the ferrite (α), and the inverse pole figure maps of (b) SDSS and (c) 316L. (For interpretation of the references to colour in this figure legend, the reader is referred to the web version of this article.)

prints of the microindents are sufficiently deep to be visible with the optical camera of the TI-750. Notice that the distance between the microindents and the grains is sufficiently large that the investigated grains are not affected by the plastic zones of the microindents. In the case of nanoindentation with non-axisymmetric Berkovich tip not only the orientation of the indented grains in indentation direction i.e. normal to the grain matters but also the crystallographic direction parallel to the surface and its relation relative to the tree fold symmetry of the Berkovich geometry should be considered. In

order to have the same normal and parallel orientations for reliable comparison between the results, in addition to confining the indents within the same grain, we used the same microindent pattern to orient the sample under the optical microscope of the TI-750 exactly in the same parallel orientation on the stage (formation of precisely similar pile up patterns in Fig. 9 clearly shows that samples are indented in the same normal and parallel orientations).

X-ray photoelectron spectroscopy

The XPS measurements were performed using a Kratos AXIS Ultra DLD spectrometer with a monochromatized Al K_{α} X-ray ($h\nu = 1486.69\text{eV}$) at 15 kV and 150 W on freshly EP and OArP treated samples. The C 1s peak from adventitious carbon at 284.9 eV was used as a reference to correct the charging shifts. Spectrometer pass energies of 160eV for the survey spectra and 20 eV for high resolution spectra were used for all elemental spectral regions. Data files were recorded in the VAMAS format and processed using the CasaXPS software package where the XPS signals were separated into the contributions from the different species.

Nanoindentation

Nanoindentation tests were performed with a Hysitron TriboIndenter™ TI-750 with a Performech™ controller in combination with an electrochemical setup to allow hydrogen charging of the samples. Nanoindentation tests were all performed on freshly EP or EP and OArP treated samples to exclude any contamination effect e.g. electron induced carbon deposition during EBSD. In addition to nanoindentations, the TI-750 is capable of scanning prior to and after the testing, giving topographical images of the samples. A long shaft Berkovich indenter tip was calibrated for both the tip area function and machine compliance prior to the tests. The procedure involves performing a series of at least 25 (up to 100) indents of different contact depths (varying the loading levels) on a fused quartz sample with a known reduced modulus of 69.6 GPa. The nanoindentations were performed with a maximum load of 2000 μN and a loading rate of 2000 $\mu\text{N s}^{-1}$, according to the load function presented in Fig. 2.

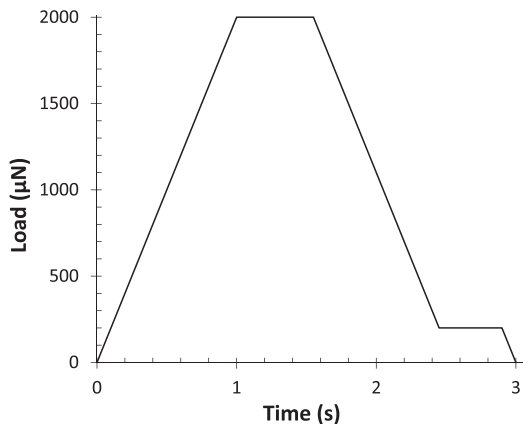


Fig. 2 – Typical load function used for nanoindentation.

For drift corrections, an additional holding time of 0.5 s at 10% of the maximum load value was added during the unloading.

In situ electrochemical nanoindentation

ECNI was used to examine the electrochemically charged hydrogen effect on nanomechanical properties. The ECNI setup consist of a three-electrode electrochemical cell integrated into the nanoindentation system explained in 2.2.4. The ECNI setup schematically shown in Fig. 3 was developed at the Norwegian University of Science and Technology and its detail are given elsewhere [21,23]. A platinum wire was the counter electrode, while a saturated calomel electrode (SCE) served as the reference electrode. The working electrode was the sample holder, and a Gamry Reference 600™ Potentiostat was used to control the electrochemical potentials. A salt bridge was used to eliminate Cl^- ion exchange between the reference electrode and the sample. The preparation of the setup prior to testing is very important, and careful cleaning must be performed. The electrochemical cell was cleaned before each set of tests with soap, water and ethanol and, lastly, was ultrasonically cleaned for 15 min in double distilled water. The long shaft tip was cleaned in ethanol and double distilled water to reduce the capillary forces acting on it during testing inside the electrolyte. Scanning probe microscopy (SPM) and nanoindentation tests were performed inside the electrochemical cell while the sample was covered with electrolyte. The electrolyte was prepared from Na_2SO_4 (99%, Merck KGaA) with deionised water (18.2 M Ω cm) at a concentration of 0.05 mol, giving a solution with a pH of 6.22.

The testing procedure was as follows: first, a freshly EP sample was installed in the electrochemical cell and tested in air. Then, a cathodic potential of -1150 mV (SCE) was applied while the electrolyte was added on top of the sample. The nanoindentation tests were started after 10 min of hydrogen charging of the sample under cathodic polarisation. For the whole period of in situ nanoindentation the sample was kept at cathodic polarization. The typical duration of the in situ test was about one hour and within this time no time dependent change in the nanomechanical behaviour was observed. Next, the sample was removed from the electrochemical cell, cleaned with distilled water, EP one more time to remove the tested layer and subjected to OArP treatment for 5 min. After the electrochemical setup was freshly cleaned and dried, the treated sample was installed and tested first in air and then

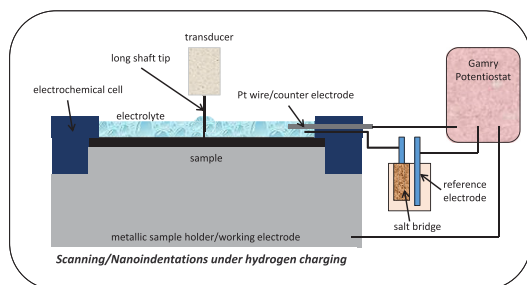


Fig. 3 – Electrochemical setup for hydrogen charging of the samples.

under hydrogen charging conditions (-1150 mV(SCE)) in the same grain as before. The microindents created for the identification of the grains were still visible after the second EP of the samples because the layer removed was not thicker than 15 μm [21].

Cyclic voltammetry tests

Cyclic voltammetry (CV) experiments were carried out to study the redox reactions on the sample surfaces using the same electrochemical setup as for the ECNI i.e. non deaerated solution (Fig. 3) while the cell was outside of the nanoindenter compartment. The samples were subjected to 10 potential sweeps between -1000 mV(SCE) and -200 mV(SCE) at different scan rate of 25 mV s^{-1} to 200 mV s^{-1} . Before and after the CV tests, the open circuit potential (OCP) was measured for 30 s. For both materials, the OCP was between -400 mV(SCE) and -500 mV(SCE).

Experimental results and discussion

Nanomechanical characterization

During a nanoindentation test, the load versus displacement is registered, and a load–displacement (LD) curve is generated. Nanoindentation tests were performed on both 316L ASS and austenitic phase in SDSS. Fig. 4 shows the typical LD curves resulting from nanoindentations in air made on the (001) orientated austenite grain of the SDSS sample and the (101) orientated grain of 316L. The LD curves of both materials show a discontinuity in the loading segment, i.e., a pop-in (between 380 μN and 420 μN for SDSS and 600 μN – 700 μN for 316L), where a sudden increase in the displacement occurs without any appreciable increase in the load. The initial elastic portions of the loading curves can be fitted with the Hertzian elastic response (dashed lines in Fig. 4) and expressed according to Eq. (1):

$$P = \frac{4}{3} E_r \sqrt{R} h^{3/2} \quad (1)$$

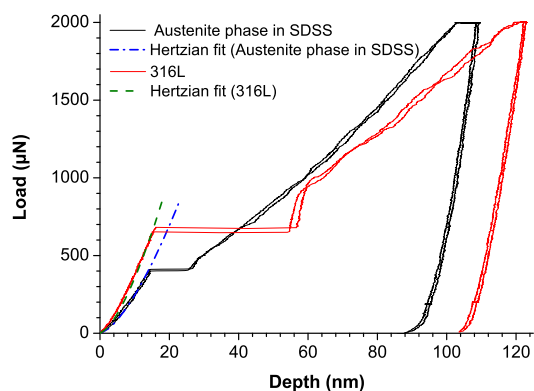


Fig. 4 – LD curves made in air on the untreated samples showing the Hertzian fit for the elastic part and the pop-ins following the dislocation nucleation.

where P is the applied load, h is the indentation depth, R is the radius of the tip curvature and E_r is the reduced modulus, given by Eq. (2):

$$\frac{1}{E_r} = \frac{1 - \nu_s^2}{E_s} + \frac{1 - \nu_i^2}{E_i} \quad (2)$$

where E_s and E_i are the elastic moduli of the sample and indenter, respectively and ν_s and ν_i are the Poissons ratio of the sample and indenter, respectively. The initial elastic loading begins as soon as the tip makes contact with the material surface and continues until dislocation nucleation or motion occurs. Typical dislocation densities in an annealed material are in the range of $1 \times 10^{10} \text{m}^{-2}$ to $1 \times 10^{12} \text{m}^{-2}$, with dislocations spaced between $1 \mu\text{m}$ and $10 \mu\text{m}$ apart. A typical indentation test in the elastic regime probes a lateral region of at most a few hundred nanometres from the point where the pop-in is noted, suggesting that the volume of material sampled by the indentation test at this depth is smaller than the average dislocation spacing [38–41]. Thus, an indentation placed randomly on the surface will have a significant probability of sampling a region that contains no pre-existing dislocations. Experimental studies [40,42–47], as well as atomistic simulations [38,48,49], have been conducted, and all lend credibility to the assumption that, for a well-annealed and EP sample, the indenter tip can initially contact a volume of material sufficiently small as to be dislocation free. The absence of dislocations means that the material continues to load elastically until the shear stress under the tip reaches a value near the theoretical shear strength of the material, well above that necessary to activate an existing dislocation source. At this point, dislocations are homogeneously nucleated, followed by subsequent glide and multiplication events. Homogeneous dislocation nucleation (HDN) should occur when the stress beneath the indenter tip approaches the theoretical shear strength of the material. The term HDN is used here to indicate that the dislocations are nucleated from an otherwise dislocation-free material. For an indentation test, the applied shear stress that nucleates a dislocation can be assumed to be the maximum shear stress beneath the indenter during purely elastic loading. According to continuum mechanics, the maximum shear stress acts on a point 0.48 times the contact radius, a , below the sample surface. Computer simulations have also shown that dislocations nucleate at this point [50]. The position of this maximum shear stress $z_{r(\text{max})}$ and its value $\tau_{r(\text{max})}$ are given by Eqs. (3) and (4):

$$z_{r(\text{max})} = 0.48 \cdot a = 0.48 \left(\frac{3PR}{4E_r} \right)^{\frac{1}{3}} \quad (3)$$

$$\tau_{r(\text{max})} = 0.31 \left(\frac{6E_r^2 P}{\pi^3 R^2} \right)^{\frac{1}{3}} \quad (4)$$

The elastic modulus and Poisson's ratios of the samples are 200 GPa and 0.3 [51] for the SDSS [52] and 194.6 GPa and 0.294 [53] for the 316L, respectively. For a standard diamond indenter probe, E_i is 1140 GPa, and ν_i is 0.07, resulting in a reduced elastic modulus of 184 GPa for the SDSS and 179.6 GPa for the 316L sample. According to Eq. (1), the elastic part of the

LD curve can be fitted to find R equal to 2200 nm for the SDSS sample and 1000 nm for the 316L (two different tips have been used in this study, one for each sample, explaining the difference in the radii). The value of R is used in Eq. (3) to calculate maximum shear stresses of 3.7 GPa (SDSS) and 2.8 GPa (316L) for the mean pop-in loads of 400 μN (SDSS) and 650 μN (316L). The theoretical strength of the material defined by Frenkels model [54] is generally approximated by $\mu/20$ to $\mu/30$, where μ is the shear modulus. Considering shear moduli of 76.9 GPa and 75.2 GPa for SDSS and 316L, respectively, the theoretical strengths of the studied materials will be in the 3.84 GPa–2.5 GPa range, which is in good agreement with the measured maximum shear stress values.

The LD curves were also analysed according to the Oliver-Pharr method [55,56] to extract the hardness and elastic modulus. The resulting hardnesses and effective Young's moduli can be calculated from Eqs. (5) and (6):

$$H = \frac{P_{\text{max}}}{A_c} \quad (5)$$

$$E_r = \frac{\sqrt{\pi}}{2} \frac{1}{\beta} \frac{S}{\sqrt{A_c}} \quad (6)$$

where S is the slope of the load–displacement curve at the initial unloading, A_c is the projected contact area evaluated from the contact depth (h_c) and the tip area function and β is a correction factor depending on the tip geometry (1.034 for a Berkovich indenter).

Fig. 5 shows the typical LD curves resulting from ECNI together with the ones made in air on the freshly EP (101) orientated austenite grain in 316L ASS. The clear effect of the hydrogen on both pop-in and hardness in agreement with the previous studies can be seen [7–9].

In the case of the freshly electropolished and then OArP treated sample the LD curves after hydrogen charging showed no change as shown in Fig. 6. The LD curves of the austenite grain in the SDSS also showed a completely identical trend as the 316L ASS and for the sake of brevity they are not included. Figs. 7 and 8 summarise the hardnesses and the

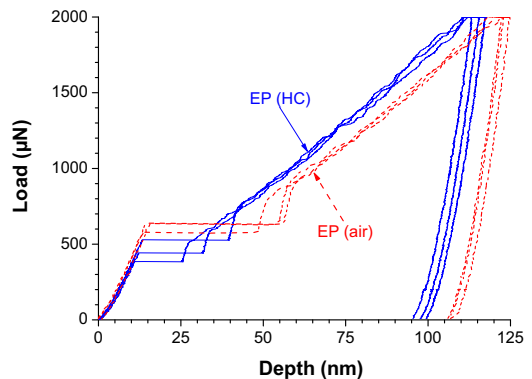


Fig. 5 – Typical LD curves resulting from in situ electrochemical nanoindentations in hydrogen charged and air, made on the freshly electropolished (101) orientated austenite grain in 316L ASS.

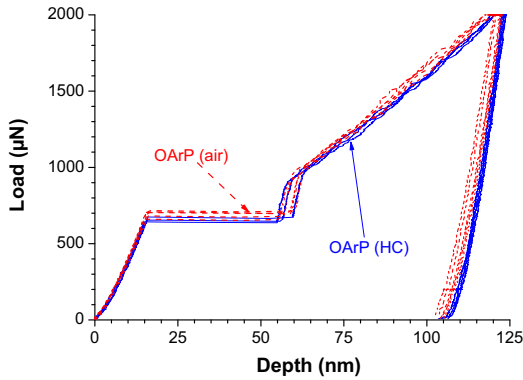


Fig. 6 – Typical LD curves resulting from in situ electrochemical nanoindentations in hydrogen charged and air, made on the freshly electropolished and then OArP treated (101) orientated austenite grain in 316L ASS.

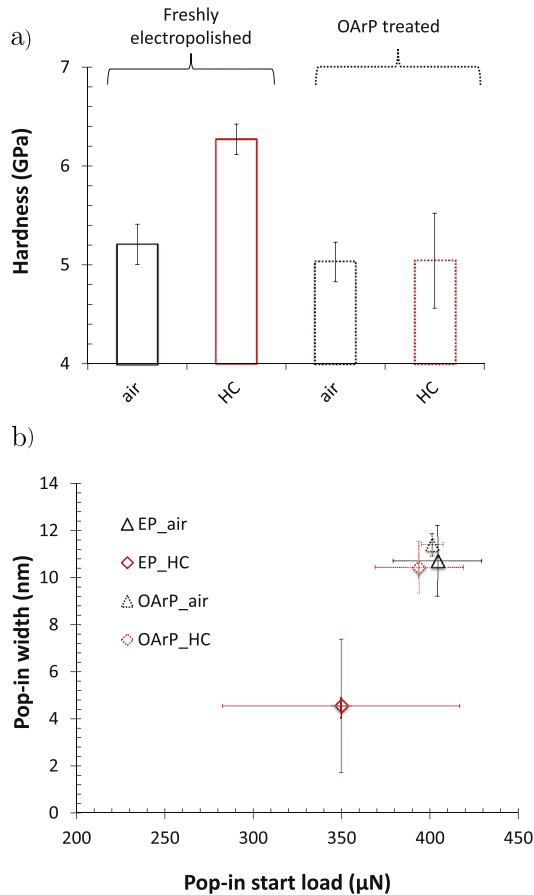


Fig. 7 – OArP treatment effect on austenitic phase of SDSS: a) hardness plot and b) pop-in behaviour with the error bars representing the standard deviation.

pop-in behaviours of the austenite phase in the SDSS and 316L samples, respectively, before and after OArP treatment. As mentioned before, the tests were performed inside the same grain to exclude any changes in the hardness or pop-in load as a result of a change in the orientation of the indented grain. Clearly, OArP treatment results in no changes in the pop-in behaviour or hardness of the austenite phase of both steels when they are indented in air. Moreover, the topographical images taken with the in situ imaging capability of the nanoindentation system show no differences in the surface topographies or indents or the pile ups around the indents prior to and after OArP treatment. A typical surface topography image of the indents made with a maximum load of 2000 μN and a loading rate of 2000 $\mu\text{N s}^{-1}$ in the 316L sample before and after OArP treatment is shown in Fig. 9. From the air indentation results and topography images, we can clearly conclude that OArP treatment has no effect on the mechanical properties or surface topographies of both austenite phases.

The ECNI tests performed on the cathodically polarised samples are also shown in Fig. 7 (SDSS) and Fig. 8 (316L).

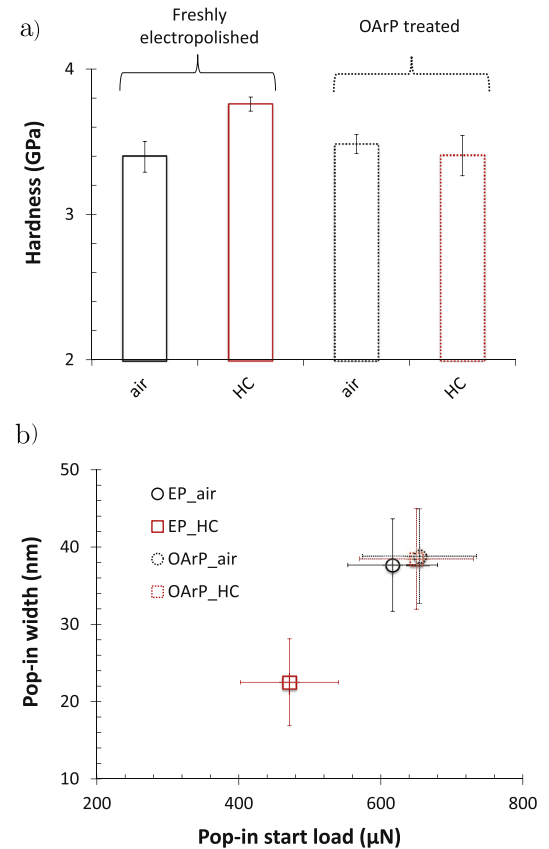


Fig. 8 – OArP treatment effect on 316L ASS: a) hardness plot and b) pop-in behaviour with the error bars representing the standard deviation.

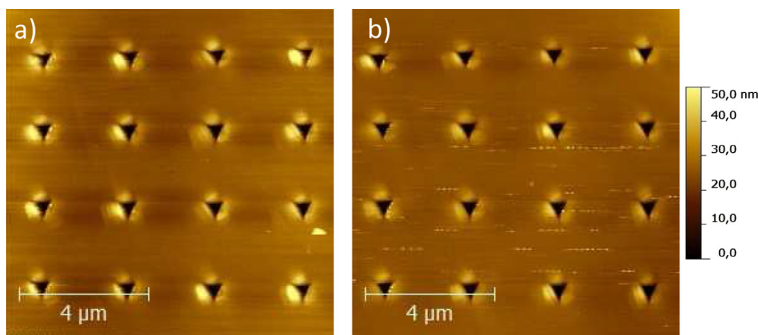


Fig. 9 – SPM topography images after nanoindentation of a 316L sample a) pre- and b) post-OArP treatment.

Obviously, hydrogen charging of untreated freshly EP samples changed both their hardnesses and pop-in loads, as expected [8,57]. However, in the case of the OArP treated samples, a similar cathodic polarisation altered neither the hardness nor the pop-in load.

The effects of electrochemically charged hydrogen on the nanomechanical properties of SDSS and 316L captured with the nanoindentation technique are well investigated and have been discussed elsewhere [7–9,21,57,58]. The change in the pop-in load can be related to the change in the activation energy required for dislocation nucleation according to the defactant theory [59–61] i.e., in the presence of hydrogen, the line energy of the dislocation is reduced, and the dislocation nucleation can occur at lower loads. The increase in the hardness is related to the effect of hydrogen on lattice friction, increasing as a result of short-range interactions between dislocations and hydrogen atoms in the solid solution [8].

Under hydrogen charging condition, the increases in hardness for both steels, as well as the decreases in pop-in load and pop-in width, are in good agreement with the results previously reported by the authors [8,21,57]. As in the

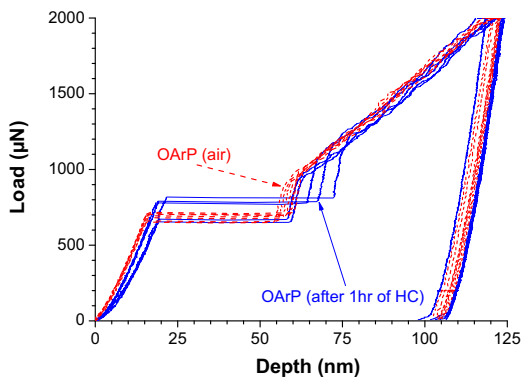
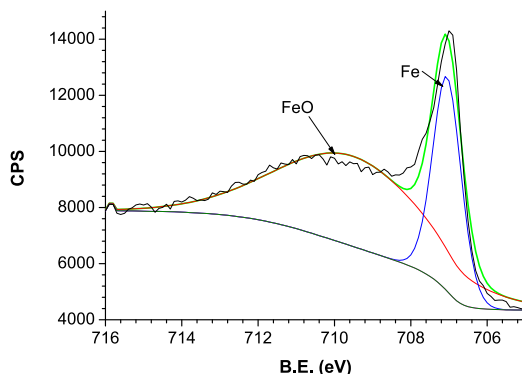
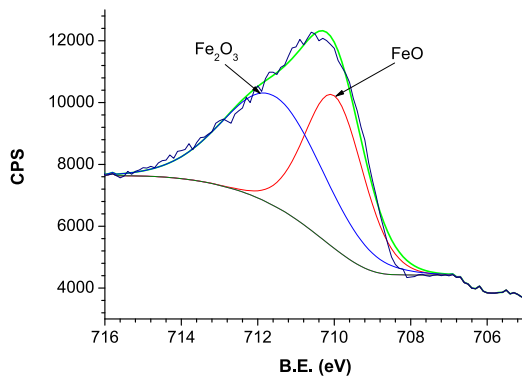


Fig. 10 – Typical LD curves resulting from one hour of hydrogen charging together with the air nanoindentation results, made on the freshly electropolished and then OArP treated (001) orientated austenite grain in 316L ASS.

case of SDSS, the non-effect of hydrogen on the 316L sample treated with OArP before charging was captured with the nanoindentation technique. Even after one hour of hydrogen charging, no changes in the LD curves and consequently the hardness or pop-ins were observed as shown in Fig. 10.



(a) Freshly electropolished 316L SS

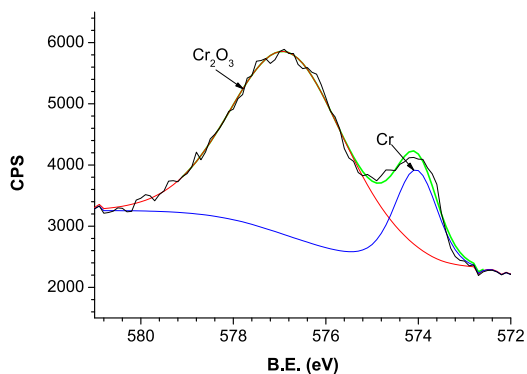


(b) OArP treated 316L SS

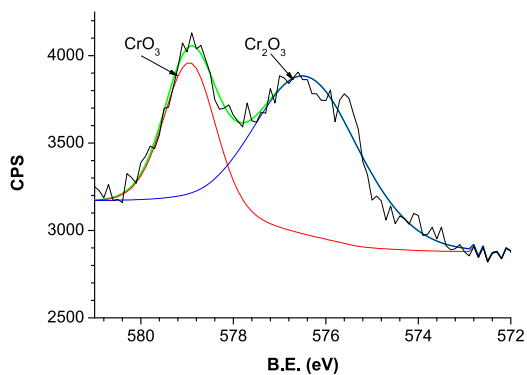
Fig. 11 – The detailed XPS spectra of Fe 2p_{3/2} of the surface films formed on (a) freshly electropolished and (b) freshly electropolished and then OArP treated 316L SS.

XPS surface analysis

XPS measurements were used to characterize the change in the composition of surface film after OARp treatment. Figs. 11–15 display the detailed spectra of O 1s, Fe 2p_{3/2}, Cr 2p_{3/2}, Ni 2p_{3/2} and Mo 3d_{5/2} in the surface films. Background subtraction was performed according to Shirley [62] and then the XPS results were separated into contributions of the different possible compounds on the basis of well characterized standards from Refs. [63–65], as shown in Table 4. Fitting of spectra from EP and OARp treated surfaces shown in Figs. 11–14, clearly shows that elemental and lower oxide peaks of metallic species are dominant in the surface of the EP sample. This is in good agreement with the previous XPS studies of the EP austenitic stainless steels [66]. After OARp treatment the elemental peaks were vanished and higher oxide peaks for Cr and Fe become detectable. Additionally, the O 1s spectra of the oxygen shown in Fig. 15 clearly show a reduction in the hydroxide peak after the OARp treatment. Based on this primary XPS analysis we can conclude that the variation in the oxidation state of the present elements on the surface after the OARp treatment have a decisive influence on

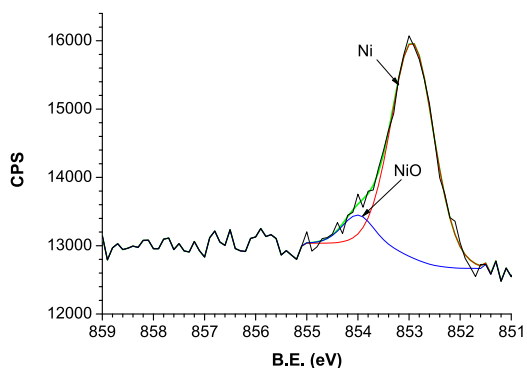


(a) Freshly electropolished 316L SS

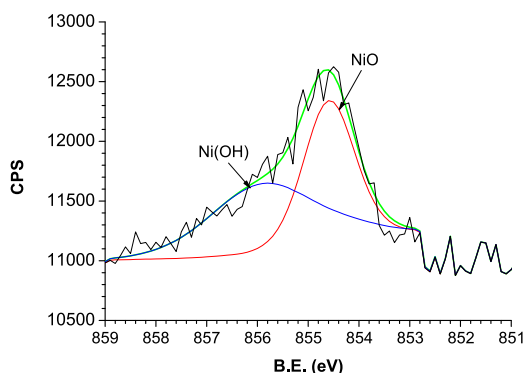


(b) OARp treated 316L SS

Fig. 12 – The detailed XPS spectra of Cr 2p_{3/2} of the surface films formed on (a) freshly electropolished and (b) freshly electropolished and then OARp treated 316L SS.



(a) Freshly electropolished 316L SS



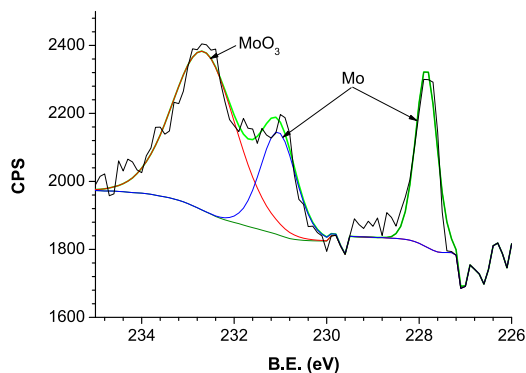
(b) OARp treated 316L SS

Fig. 13 – The detailed XPS spectra of Ni 2p_{3/2} of the surface films formed on (a) freshly electropolished and (b) freshly electropolished and then OARp treated 316L SS.

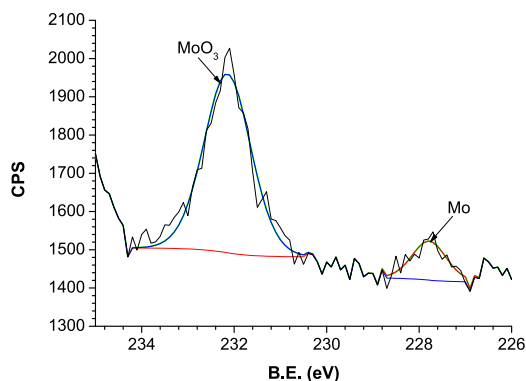
the hydrogen uptake of the austenitic stainless steel from the surface. Further quantitative XPS analysis in combination with the surface sputtering are planned to have a more in depth characterization of the surface films after the OARp treatment.

Electrochemical analysis

To reveal any differences in the electrochemical behaviour on the surface of the freshly EP samples and the OARp treated samples, CV tests were performed. The CV curves with the 100 mV s⁻¹ scan rate are shown in Fig. 16 for both materials. The voltammograms clearly show the differences in the electrochemical behaviour before and after OARp treatment. It is worth mentioning that every parameter except the surface condition of the samples remains precisely the same during these electrochemical tests. The electrochemical behaviour of the samples is characterised by a cathodic (reduction) peak and an anodic (oxidation) peak. For both SDSS and 316L, there is a significant difference in the currents and the potentials where the cathodic and anodic current peaks appear for the two applied treatments. The interpretation of the



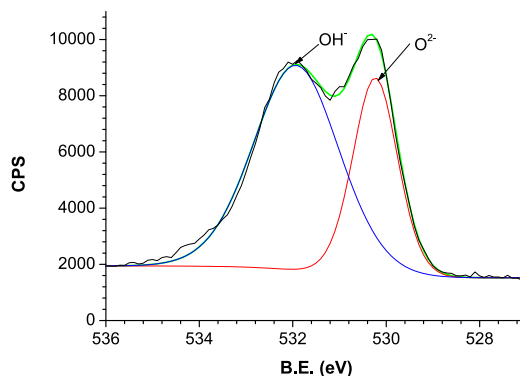
(a) Freshly electropolished 316L SS



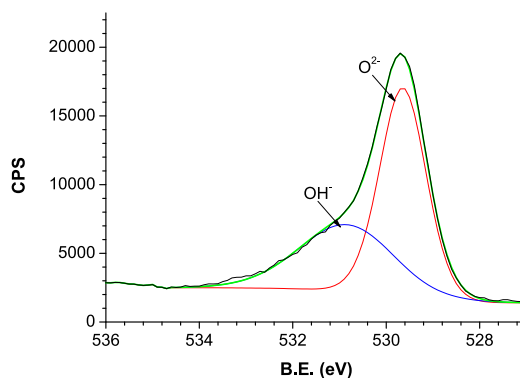
(b) OArP treated 316L SS

Fig. 14 – The detailed XPS spectra of Mo 3d of the surface films formed on (a) freshly electropolished and (b) freshly electropolished and then OArP treated 316L SS.

voltammogram taken from the SDSS is not as straightforward as the ASS, due to the co-presence of the both austenite and ferrite phases. Though, voltammograms of both steels except EP SDSS show clearly an anodic and a cathodic peak. The OArP treatment shifted the peaks to more cathodic values. The anodic peak for SDSS at potential -418 mV(SCE) and for ASS at -390 mV(SCE) are ascribed to the oxidation of Fe(II) to Fe(III) [67] which are shifted respectively to -476 mV(SCE) and -550 mV(SCE) after OArP treatment. In the reduction cycle while there is no clear peak for SDSS but only a local flattened region at -724 mV(SCE) a peak for ASS at -566 mV(SCE) was observed which are attributed to valence transitions, occurring in the solid state, associated with the reductive dissolution of a hydrated ferric oxide to ferrous oxide [68]. As in the case of anodic peaks these cathodic peaks are also shifted after OArP treatment to more cathodic values of -858 mV(SCE) and -818 mV(SCE) respectively. The shift in the cathodic direction of the peak potentials in the voltammograms is associated with compositional changes in the passive film and also observed within the XPS measurements. The same shift in the peak potentials was observed by Ramasubramanian et al. [69]



(a) Freshly electropolished 316L SS



(b) OArP treated 316L SS

Fig. 15 – The detailed XPS spectra of O 1s of the surface films formed on (a) freshly electropolished and (b) freshly electropolished and then OArP treated 316L SS.

after anodizing of 316L stainless steel. Additionally the heights of the reduction peak, attributed to hydrated ferric oxide in the voltammograms, is seen to increase after OArP treatment. This variation is directly related to the charge passed during the reduction of the oxide and corresponds to an increase in the thickness of the oxide. Additional work is necessary to relate quantitatively the peaks in the

Table 4 – Binding energies (B.E.) of XPS-peaks for standard states.

Element	Peak	Fe	Fe ₃ O ₄	FeO	Fe ₃ O ₃	FeOOH
Fe 2p3/2	Peak	706.7	708.2	709.4	710.9	711.8
	B.E.(eV)					
Cr 2p3/2	Peak	Cr	Cr ₂ O ₃	Cr(OH) ₃	CrO ₃	
	B.E.(eV)	574.3	576.8	577.3	579.0	
Ni 2p3/2	Peak	Ni	NiO	Ni(OH) ₂		
	B.E.(eV)	852.7	853.8	855.6		
Mo 3d5/2	Peak	Mo	Fe ₂ (MoO ₄) ₃	MoO ₃		
	B.E.(eV)	227.9	232.5	232.6		
O 1s	Peak	O ²⁻	OH ⁻			
	B.E.(eV)	530.2	531.5			

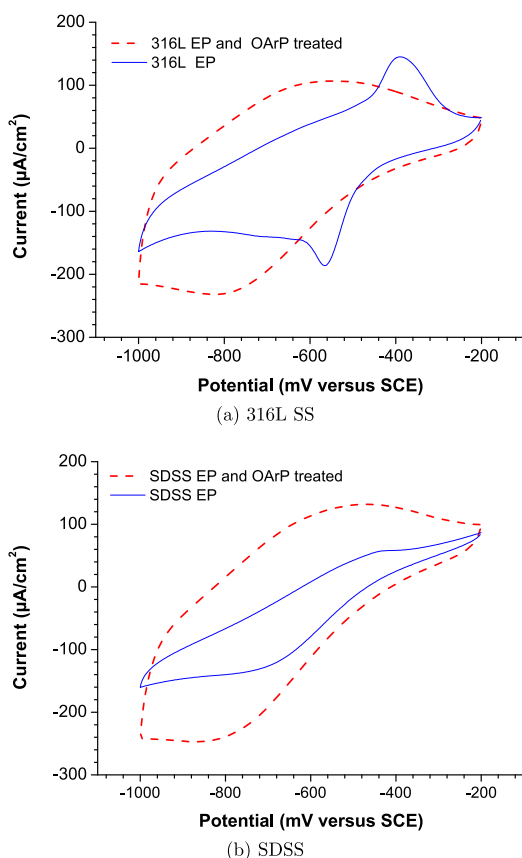


Fig. 16 – Cyclic voltammetry characterisations on a sweep rate of 100 mV s^{-1} of a) SDSS and b) 316L samples.

voltammograms with the composition of the passive film and the XPS analysis.

Conclusions

The advantageous effects of oxygen–argon plasma treatment on the nanomechanical properties of cathodically polarized austenitic stainless steel and the austenitic phase in SDSS were revealed and studied in this work. Cathodic polarization and consequent charging of the electropolished samples with the hydrogen clearly resulted in the reduction of the load necessary for the onset of the plasticity the so called pop-in load. Additionally, electrochemically charged hydrogen increased the hardness of the austenite in both electropolished 316L austenitic stainless steel and super duplex stainless steel. The change in the pop-in load is related to the change in the activation energy required for dislocation nucleation according to the defectant theory i.e., in the presence of hydrogen, the line energy of the dislocation is reduced, and the dislocation nucleation can occur at lower

loads. The increase in the hardness is related to the effect of hydrogen on lattice friction, increasing as a result of short-range interactions between dislocations and hydrogen atoms in the solid solution. After oxygen–argon plasma treatment the nanomechanical properties of the samples surfaces in air did not change. Also, the reduction in the hardness and pop-in load induced by electrochemically charged hydrogen at cathodic polarization was not observed for the oxygen–argon plasma treated samples. XPS analysis clearly showed the compositional changes of the surface film on 316L austenitic stainless steel sample. Electrochemical cyclic voltammetry showed the clear change in electrochemical behaviour due to the variation in the surface oxide composition. The clear inhibition of hydrogen induced hardening and reduction in the pop-in load after oxygen–argon plasma treatment proved that this treatment prevents hydrogen uptake into the substrate metal. The exact explanation for this decrease in the hydrogen uptake is still unclear. The changes in the electronic structures of the semiconductive oxide film through variation in the oxidation states as shown by XPS analysis after OArP treatment which can alter both the hydrogen evolution reaction on the surface and/or hydrogen diffusion into the metal is assumed to be the reason for this change.

Acknowledgements

The authors would like to acknowledge the Research Council of Norway for providing financial support through the PET-ROMAKS Program (10290803) and PhD candidate Amin Hossein Zavieh from Department of Engineering Design and Materials, NTNU, for performing the XPS measurements.

REFERENCES

- [1] Turnbull A, Hutchings R. Analysis of hydrogen atom transport in a two-phase alloy. *Mater Sci Eng A* 1994;177(1):161–71.
- [2] Koyama M, Akiyama E, Sawaguchi T, Ogawa K, Kireeva IV, Chumlyakov YI, et al. Hydrogen-assisted quasi-cleavage fracture in a single crystalline type 316 austenitic stainless steel. *Corros Sci* 2013;75:345–53. Russia.
- [3] Griffiths A, Turnbull A. Defining the limits of application of duplex stainless steel coupled to carbon steel in oilfield environments. *Corrosion* 2001;57(2):165–74.
- [4] Hatano M, Fujinami M, Arai K, Fujii H, Nagumo M. Hydrogen embrittlement of austenitic stainless steels revealed by deformation microstructures and strain-induced creation of vacancies. *Acta Mater* 2014;67(0):342–53.
- [5] Olden V, Thaulow C, Johnsen R. Modelling of hydrogen diffusion and hydrogen induced cracking in supermartensitic and duplex stainless steels. *Mater Des* 2008;29(10):1934–48.
- [6] Griffiths A, Turnbull A. Hydrogen uptake and cracking in 22% Cr duplex stainless steel under galvanic coupling conditions. *Corrosion* 1997;53(9):700–4.
- [7] Zhang L, An B, Fukuyama S, Yokogawa K. Hydrogen effects on localized plasticity in SUS310S stainless steel investigated by nanoindentation and atomic force microscopy. *Jpn J Appl Phys* 2009;48(8).

- [8] Barnoush A, Asgari M, Johnsen R. Resolving the hydrogen effect on dislocation nucleation and mobility by electrochemical nanoindentation. *Scr Mater* 2012;66:414–7.
- [9] Nibur K, Bahr D, Somerday B. Hydrogen effects on dislocation activity in austenitic stainless steel. *Acta Mater* 2006;54:2677–84.
- [10] Olden V, Alvaro A, Akselsen OM. Hydrogen diffusion and hydrogen influenced critical stress intensity in an API X70 pipeline steel welded joint—experiments and FE simulations. *Int J Hydrogen Energy* 2012;37(15):11474–86.
- [11] Oltra R, Bouillot C, Magnin T. Localized hydrogen cracking in the austenitic phase of a duplex stainless steel. *Scr Mater* 1996;35(9):1101–5.
- [12] Takakuwa O, Soyama H. Suppression of hydrogen-assisted fatigue crack growth in austenitic stainless steel by cavitation peening. *Int J Hydrogen Energy* 2012;37(6):5268–76.
- [13] Zakroczyński T, Owczarek E. Electrochemical investigation of hydrogen absorption in a duplex stainless steel. *Acta Mater* 2002;50(10):2701–13.
- [14] El-Yazgi A, Hardie D. Stress corrosion cracking of duplex and super duplex stainless steels in sour environments. *Corros Sci* 1998;40(6):909–30.
- [15] Borchers C, Michler T, Pundt A. Effect of hydrogen on the mechanical properties of stainless steels. *Adv Eng Mater* 2008;10:11–23.
- [16] Barnoush A. Hydrogen embrittlement, revisited by in situ electrochemical nanoindentation. Ph.D. thesis. Saarland University; 2009.
- [17] Zakroczyński T, Lukomski N, Flis J. The effect of plasma nitriding-base treatments on the absorption of hydrogen by iron. *Corros Sci* 1995;37(5):811–22.
- [18] Ąwiek J, Baczyńska M. Behaviour of nitrated layers subjected to influence of hydrogen. *Sci Eng* 2010;43(1):30–41.
- [19] Lepiński C, Kuromoto N, Souza J, Foerster C, Serbena F, Silva S. Effect of hydrogen on mechanical properties of nitrated austenitic steels. *Philos Mag* 2006;86(33–35):5407–18.
- [20] Bruzzoni P, Brühl SP, Gómez BJ, Nosei L, Ortiz Ma, Feugeas JN. Hydrogen permeation modification of 4140 steel by ion nitriding with pulsed plasmas. *Surf Coat Tech* 1998;110(1):13–8.
- [21] Asgari M, Barnoush A, Johnsen R, Hoel R. Nanomechanical evaluation of the protectiveness of nitrated layers against hydrogen embrittlement. *Corros Sci* 2012;62:51–60.
- [22] Asgari M, Barnoush A, Johnsen R, Hoel R. Microstructural characterization of pulsed plasma nitrated 316L stainless steel. *Mater Sci Eng A* 2011;529:425–34.
- [23] Barnoush A, Asgari M, Johnsen R, Hoel R. Hydrogen effect on nanomechanical properties of the nitrated steel. *Metall Mater Trans A* 2013;44:766–75.
- [24] Izawa C, Wagner S, Martin M, Weber S, Pargeter R, Michler T, et al. SIMS analysis on austenitic stainless steel: the influence of type of oxide surface layer on hydrogen embrittlement. *J Alloys Compds* 2013;580(Suppl. 1(0)):S13–7 [SI] : [MH2012].
- [25] Bahr D, Nelson J, Tymiak N, Gerberich W. The mechanical behavior of a passivating surface under potentiostatic control. *J Mater Res* 1997;12(12):3345–53.
- [26] Barnoush A, Vehoff H. In situ electrochemical nanoindentation: a technique for local examination of hydrogen embrittlement. *Corros Sci* 2008;50:259–67.
- [27] Guo H, Lu B, Luo J. Response of surface mechanical properties to electrochemical dissolution determined by in situ nanoindentation technique. *Electrochem Commun* 2006;8:1092–8.
- [28] Barnoush A, Bies C, Vehoff H. In situ electrochemical nanoindentation of FeAl (100) single crystal: hydrogen effect on dislocation nucleation. *J Mater Res* 2009;24(3):1105–13.
- [29] Seo M, Chiba M. Nano-mechano-electrochemistry of passive film surfaces. *Electrochim Acta* 2001;47:319–25.
- [30] Barnoush A, Vehoff H. Hydrogen embrittlement of aluminum in aqueous environments examined by in situ electrochemical nanoindentation. *Scr Mater* 2008;58:747–50.
- [31] Seo M, Kurata Y. Nano-mechano-electrochemical properties of passive titanium surfaces evaluated by in-situ nano-indentation and nano-scratching. *Electrochim Acta* 2003;48(20):3221–8.
- [32] Barnoush A, Vehoff H. Electrochemical nanoindentation: a new approach to probe hydrogen/deformation interaction. *Scr Mater* 2006;55:195–8.
- [33] Barnoush A, Vehoff H. Recent developments in the study of hydrogen embrittlement: hydrogen effect on dislocation nucleation. *Acta Mater* 2010;58(16):5274–85.
- [34] Barnoush A, Dake J, Kheradmand N, Vehoff H. Examination of hydrogen embrittlement in FeAl by means of in situ electrochemical micropillar compression and nanoindentation techniques. *Intermetallics* 2010;18(7):1385–9.
- [35] Zamanzade M, Vehoff H, Barnoush A. Cr effect on hydrogen embrittlement of iron aluminide intermetallics: surface or bulk effect. *Acta Mater* 2014;69:210–23.
- [36] Zamanzade M, Vehoff H, Barnoush A. Effect of chromium on elastic and plastic deformation of Fe₃Al intermetallics. *Intermetallics* 2013;41(0):28–34.
- [37] Zhang H, Hei Z, Liu G, Lu J, Lu K. Formation of nanostructured surface layer on AISI 304 stainless steel by means of surface mechanical attrition treatment. *Acta Mater* 2003;51(7):1871–81.
- [38] Begau C, Hartmaier A, George E, Pharr G. Atomistic processes of dislocation generation and plastic deformation during nanoindentation. *Acta Mater* 2011;59(3):934–42.
- [39] Bei H, Gao Y, Shim S, George E, Pharr G. Strength differences arising from homogeneous versus heterogeneous dislocation nucleation. *Phys Rev B* 2008;77(6):6103.
- [40] Barnoush A. Correlation between dislocation density and nanomechanical response during nanoindentation. *Acta Mater* 2012;60(3):1268–77.
- [41] Sadrabadi P, Durst K, Göken M. Study on the indentation size effect in ca₂: dislocation structure and hardness. *Acta Mater* 2009;57(4):1281–9.
- [42] Ahn T, Oh C, Lee K, George E, Han H. Relationship between yield point phenomena and the nanoindentation pop-in behavior of steel. *J Mater Res* 2012;1(1):1–6.
- [43] Barnoush A, Yang B, Vehoff H. Advances in solid state physics. In: chap. Effect of hydrogen and grain boundaries on dislocation nucleation and multiplication examined with a NI-AFM, vol. 47. Berlin/Heidelberg: Springer; 2008. pp. 253–69.
- [44] Montagne A, Audurier V, Tromas C. Influence of pre-existing dislocations on the pop-in phenomenon during nanoindentation in MgO. *Acta Mater* 2013;(0).
- [45] Mao W, Shen Y. Nanoindentation study of pop-in phenomenon characteristics and mechanical properties of sapphire (10–12) crystal. *J Am Ceram Soc* 2012;95(11):3605–12.
- [46] Bahr D, Jennerjohn S, Morris D. Dislocation nucleation and multiplication in small volumes: the onset of plasticity during indentation testing. *JOM* 2009;61:56–60.
- [47] Vehoff H, Yang B, Barnoush A, Natter H, Hempelmann R. Mechanical properties of nanomaterials examined with a NI-AFM. *Z Phys Chem* 2008;222:499–525.
- [48] Wen M, Zhang L, An B, Fukuyama S, Yokogawa K. Hydrogen-enhanced dislocation activity and vacancy formation during nanoindentation of nickel. *Phys Rev B* 2009;80(9):094113 [pages 5].



- [49] Engels P, Ma A, Hartmaier A. Continuum simulation of the evolution of dislocation densities during nanoindentation. *Int J Plast* 2012;38(0):159–69.
- [50] Zhu T, Li J, Vliet KJ, Ogata S, Yip S, Suresh S. Predictive modeling of nanoindentation-induced homogeneous dislocation nucleation in copper. *J Mech Phys Solids* 2004;52:691.
- [51] Pilhagen J, Sandström R. Loss of constraint during fracture toughness testing of duplex stainless steels. *Eng Fract Mech* 2013;99:239–50.
- [52] Bello J, Wood R, Wharton J. Synergistic effects of micro-abrasion–corrosion of UNS S30403, S31603 and S32760 stainless steels. *Wear* 2007;263(1):149–59.
- [53] Ledbetter H. Stainless-steel elastic constants at low temperatures. *J Appl Phys* 1981;52(3):1587–9.
- [54] Frenkel J. Zur Theorie der Elastizitätsgrenze und der Festigkeit kristallinischer Körper. *Z für Phys* 1926;37:572–609.
- [55] Oliver W, Pharr G. Measurement of hardness and elastic modulus by instrumented indentation: advances in understanding and refinements to methodology. *J Mater Res* 2004;19(1):3–20.
- [56] Oliver W, Pharr G. An improved technique for determining hardness and elastic modulus using load and displacement sensing indentation experiments. *J Mater Res* 1992;7(6):1564–83.
- [57] Basa A, Barnoush A, Thaulow C. Nanomechanical testing of hydrogen effects on super duplex stainless steel. *Mech Test Diagn* 2012;2:5–14.
- [58] Tal-Gutelmacher E, Gemma R, Volkert C, Kirchheim R. Hydrogen effect on dislocation nucleation in a vanadium (1 0 0) single crystal as observed during nanoindentation. *Scr Mater* 2010;63(10):1032–5.
- [59] Kirchheim R. Reducing grain boundary, dislocation line and vacancy formation energies by solute segregation. I. Theoretical background. *Acta Mater* 2007;55(15):5129–38.
- [60] Kirchheim R. Reducing grain boundary, dislocation line and vacancy formation energies by solute segregation: II. Experimental evidence and consequences. *Acta Mater* 2007;55(15):5139–48.
- [61] Kirchheim R. On the solute-defect interaction in the framework of a defectant concept. *Int J Mater Res* 2009;100(4):483–7.
- [62] Shirley DA. High-resolution X-ray photoemission spectrum of the valence bands of gold. *Phys Rev B* 1972;5(12):4709.
- [63] Wagner C, Riggs W, Davis L, Moulder J. Handbook of X-ray photoelectron spectroscopy. Perkin-Elmer Corporation; 1979.
- [64] Asami K, Hashimoto K. The X-ray photo-electron spectra of several oxides of iron and chromium. *Corros Sci* 1977;17(7):559–70.
- [65] Graat PC, Somers MA. Simultaneous determination of composition and thickness of thin iron-oxide films from XPS Fe 2p spectra. *Appl Surf Sci* 1996;100–101:36–40.
- [66] Hryniewicz T, Rokosz K, Rokicki R. Electrochemical and XPS studies of AISI 316L stainless steel after electropolishing in a magnetic field. *Corros Sci* 2008;50(9):2676–81.
- [67] Büchler M, Schmuki P, Böhni H. Iron passivity in borate buffer. *J Electrochem Soc* 2005;145:609.
- [68] Kocijan A, Donik vD, Jenko M. Electrochemical and XPS studies of the passive film formed on stainless steels in borate buffer and chloride solutions. *Corros Sci* 2007;49(5):2083–98.
- [69] Ramasubramanian N, Preocanin N, Davidson R. Analysis of passive films on stainless steel by cyclic voltammetry and auger spectroscopy. *J Electrochem Soc* 1985;132(4):793–8.

PAPER II

An In-Situ Electrochemical Nanoindentation (ECNI) Study on the Effect of Hydrogen on the Mechanical Properties of 316L Austenitic Stainless Steel

Article

An In-Situ Electrochemical Nanoindentation (ECNI) Study on the Effect of Hydrogen on the Mechanical Properties of 316L Austenitic Stainless Steel

Adina Basa, Dong Wang , Nuria Espallargas and Di Wan * 

Department of Mechanical and Industrial Engineering (MTP), Norwegian University of Science and Technology (NTNU), Richard Birkelands vei 2B, 7491 Trondheim, Norway; adina.basa@ntnu.no (A.B.); dong.wang@ntnu.no (D.W.); nuria.espallargas@ntnu.no (N.E.)

* Correspondence: di.wan@ntnu.no

Abstract: In-situ electrochemical nanoindentation (ECNI) has been used to study the effect of hydrogen on the mechanical properties of austenitic stainless steel AISI 316L. Changing the electrode potential (via electrochemical charging) revealed the interconnected nature of the hydrogen effect on the nanomechanical properties of the stainless steel. At more positive cathodic potentials, a softening effect of hydrogen can be noticed, while significant hardening can be observed at more negative cathodic potentials. The hydrogen effects on the nanomechanical properties were analyzed in terms of the homogeneous dislocation nucleation (HDN) and the hydrogen-dislocation interactions from the energy point of view. The effects can be explained with the framework of the defactant theory and the hydrogen-enhanced localized plasticity (HELP) mechanism.

Keywords: hydrogen embrittlement; in-situ electrochemical nanoindentation; austenitic stainless steel; electron backscattered diffraction; cathodic charging



Citation: Basa, A.; Wang, D.; Espallargas, N.; Wan, D. An In-Situ Electrochemical Nanoindentation (ECNI) Study on the Effect of Hydrogen on the Mechanical Properties of 316L Austenitic Stainless Steel. *Materials* **2021**, *14*, 6426. <https://doi.org/10.3390/ma14216426>

Academic Editor: Alexander J. G. Lunt

Received: 6 October 2021

Accepted: 21 October 2021

Published: 26 October 2021

Publisher's Note: MDPI stays neutral with regard to jurisdictional claims in published maps and institutional affiliations.



Copyright: © 2021 by the authors. Licensee MDPI, Basel, Switzerland. This article is an open access article distributed under the terms and conditions of the Creative Commons Attribution (CC BY) license (<https://creativecommons.org/licenses/by/4.0/>).

1. Introduction

The interaction between hydrogen and structural materials, especially stainless steels, is causing numerous kinds of problems in industry, among which hydrogen embrittlement has been a great concern since its first discovery in 1875 [1]. In many industrial applications, the ingress of hydrogen into the steel microstructure has effects on the chemical and mechanical properties of the materials. There are different mechanisms in the literature explaining the hydrogen-induced degradation, such as hydrogen-enhanced localized plasticity (HELP) [2–4], hydrogen-enhanced decohesion (HEDE) [5–7], hydrogen-enhanced strain-induced vacancy formation (HESIV) [8,9], adsorption-induced dislocation emission (AIDE) [10,11], etc. More recently, researchers found that the mechanisms are not independent and can sometimes work simultaneously to have a synergistic action. For instance, the HELP + HEDE concept or the HELP-mediated HEDE model has been proposed [12]. However, a common agreement on what are the main causes for hydrogen embrittlement is still challenging to find due to the intrinsic complexity of the testing procedures and the many factors acting simultaneously in the process. This can in fact be seen as a system-dependent process, in which the operating conditions (environment, electrolyte composition, mechanical action, etc.) will determine the response, and therefore it is very difficult to have a unique theory or explanation for this degradation mechanism.

Austenitic stainless steels (ASS) are widely used in a variety of applications where corrosion resistance is needed, like in the oil and gas industry, offshore structures, or in pressurized pipeline applications [13–15]. In these applications, the risk of hydrogen embrittlement exists since the system is typically exposed to hydrogen (via cathodic protection) and mechanical loading [16–18]. The mechanical properties of the stainless steels exposed to cathodic charging or hydrogen gas environments degrade very quickly since

hydrogen is a small atom that can very easily diffuse in the microstructure of metals [19–22]. There is a vast number of experimental studies focusing on the relationship between hydrogen and plastic deformation in ASS, reporting significant effects on the plasticity [23–26]. However, a thorough literature survey shows a large contradiction in the magnitude of the hydrogen-induced degradation of mechanical properties. To justify the apparent inconsistency of some of these results, the experimental conditions (e.g., hydrogen charging conditions, geometry of the sample, stability of the structure) must be carefully controlled. For example, hydrogen charging of ASS at high temperatures may provide a relatively uniform distribution of hydrogen due to the higher diffusion coefficient than at room temperature [27,28]. Another example is the ex-situ mechanical tests, which are affected by the hydrogen gradient in the sample as a result of the outgassing of the hydrogen throughout the tests. The in-situ electrochemical hydrogen charging at room temperature can also be affected by the hydrogen gradient from the surface into the bulk of the sample [29]. In addition, the in-situ electrochemical hydrogen charging using recombination poisons like As_2O_3 (to increase the hydrogen effects) may lead to lattice distortions of the austenite as well as an increase of the defect density and the local formation of unstable hydrides [30,31]. Even though these observations report the degradation of mechanical properties due to hydrogen, they cannot be accounted for in the interaction of hydrogen with dislocations during plastic deformation.

The electrochemical nanoindentation (ECNI) technique has been proven to be a reliable approach to study the effect of hydrogen on materials' plasticity due to a uniform hydrogen concentration on the sample surface as well as the fact that the sample surface quality is not altered during hydrogen charging. ECNI implies using moderate conditions, i.e., low current densities are applied and no additional recombination of poisons are required, and therefore the austenite stability is not affected [32]. ECNI brings the possibility of simultaneous electrochemical hydrogen charging and nanomechanical testing within a very small volume close to the surface where the hydrogen concentration within a very short time becomes uniform. The significant advantage of ECNI is that all related behavior can be limited within a single grain, such that microstructural variations can be eliminated as much as possible. Moreover, when the microstructural features are intentionally studied, by combining micro-fabrication techniques, the small-scale cantilever beam bending or pillar compression tests can provide more insights [33–36]. Since ECNI is focusing on the deformation behavior in a limited volume, getting comparable results as from large-scale testing is rather challenging, but on the other hand, it suits refined studies on the genuine local material behavior. This technique has already been applied for studying the mechanism of hydrogen embrittlement and hydrogen dislocation interaction in various materials [37–40]. To the authors' knowledge, ECNI studies on ASS are relatively limited [41,42]. While previous works mostly focused on the hardening effect of hydrogen with cathodic polarization, sometimes, it can also be found that a softening effect can be recorded, similar to that from large-scale tests [12,43]. Covering a wider polarizing potential range (therefore a variety of hydrogen amounts) in the studies may potentially provide information for better understanding the hydrogen effect in a more comprehensive way.

In this paper, in-situ ECNI was used to study the effect of hydrogen on the nanomechanical performance of austenitic stainless steel AISI 316L. During the nanoindentation of samples with a very low dislocation density, it is possible to observe a homogeneous dislocation nucleation (HDN) below the surface. By further analyzing the pop-in behavior, the energy consumption can be carefully modelled during the onset of plastic deformation. By controlling the electrochemical cathodic potentials, different amounts of hydrogen can be introduced, and thus the nanomechanical performance evolution can be clearly observed with respect to hydrogen evolution. Finally, the possible hydrogen–metal interaction mechanisms are discussed. The current methodology can avoid extrinsic influencing factors as much as possible and reveal the intrinsic hydrogen–material interaction.

2. Materials and Methods

2.1. Sample Preparation

A cylindrical sample (12 mm diameter and 1~2 mm thickness) was cut by electrical discharge machining from a 316L ASS slab. The composition is given in Table 1. In order to achieve large austenite grains in the microstructure (ca 200 μm) and a low dislocation density, the sample was heat treated at 1150 $^{\circ}\text{C}$ for 8 days in vacuum followed by cooling in the furnace.

Table 1. Chemical composition of the studied steel.

Element	C	Si	Mn	S	P	Cr	Ni	Mo	N
wt.%	0.015	0.38	1.25	0.0005	0.027	16.39	10.16	2.09	0.04

Standard surface preparation, including grinding with silicon-carbide papers up to 2400 grade, followed by mechanical polishing with a water-based diamond suspension up to 1 μm was carried out. In the final step, electropolishing using 20 V in a methanol/ H_2SO_4 electrolyte for 30 s was used. Electropolishing was used to remove the plastically deformed surface layer produced by mechanical polishing. This is an important step in studying the metastable ASS because the mechanically deformed layer can undergo a phase transformation (austenite to martensite) and the electropolishing step guarantees a fully austenitic sample.

2.2. Microstructure

The microstructure of the material was characterized by electron backscatter diffraction (EBSD) mapping. A field emission scanning electron microscope (FESEM) Zeiss Supra 55 VP (ZEISS, Jena, Germany) was used for EBSD mapping of the samples prior to testing and TSL OIM software (version 7.2.1) was used for the data analysis. The sample was tilted by 70 $^{\circ}$, the acceleration voltage was 30 kV, the working distance was 21 mm, and a step size of 200 nm was used for EBSD mapping. Figure 1 presents the normal direction (i.e., indentation direction) inverse pole figure map. The initial microstructure of the tested material consisted of well-annealed equiaxial grains with a grain size larger than 200 μm . To exclude the crystallographic orientation effect, all sets of nanoindentations were performed within the same grain oriented close to the (101) direction, as indicated by the arrow in the figure. For easier identification of the selected grain, the sample was marked with 2 microindents (denoted as MI in Figure 1) where the prints of the microindents are sufficiently deep to be visible with the optical microscope of the TI-950 nanoindentation system (Bruker, former Hysitron, Minneapolis, MN, USA). Notice that the distance between the microindents and the grains is sufficiently large (larger than 200 μm), so the investigated grain is not affected by the plastic zones of the microindents.

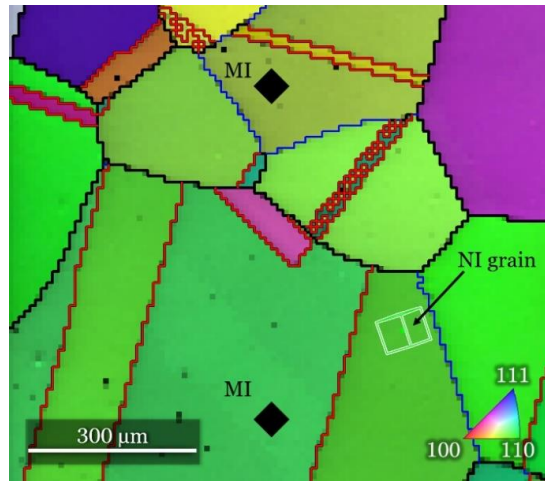


Figure 1. Normal direction inverse pole figure map of 316L ASS sample marked with micro-indenters (MI) for finding the grain selected for performing nanoindentation test. Black line is high-angle grain boundary; blue line is low-angle grain boundary; red line is twin boundary with 60° - $\langle 111 \rangle$ relationship.

2.3. In-Situ ECNI

The in-situ ECNI experiments were performed with a Tribo-Indenter TI-950, with a Performech™ controller (Bruker, former Hysitron, Minneapolis, MN, USA) in combination with an electrochemical setup to allow hydrogen charging of the samples. In addition to nanoindentation, the TI-950 is capable of scanning prior to and after testing, giving topographical images of the samples. A long shaft Berkovich indenter tip was calibrated for both the tip area function and machine compliance prior to the tests. The schematic of the experimental setup is shown in Figure 2.

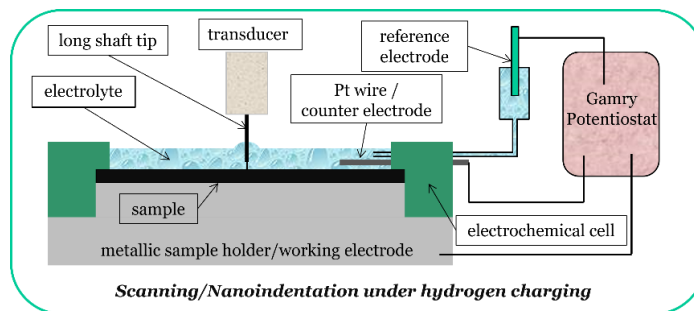


Figure 2. Experimental setup of the in-situ ECNI technique.

The nanoindentation was performed with a maximum load of $2000 \mu\text{N}$ and a loading rate of $2000 \mu\text{N/s}$. A typical load–displacement curve together with the load function is presented in Figure 3. For drift corrections, an additional holding time of 0.2 s at 10% of the maximum load value was added during the unloading. For hydrogen charging, a three-electrode electrochemical setup was used. The electrolyte was prepared from Na_2SO_4 (99%, Merck KGaA, Darmstadt, Germany) with deionized water at a concentration of 0.05 mol/L. The measured pH was 6.22. A platinum wire was used as the counter electrode, while $\text{Hg}/\text{Hg}_2\text{SO}_4$ was used as reference electrode. All electrode potentials in this study are referenced to this electrode. The working electrode was the ASS sample, and a Gamry

Reference 600TM Potentiostat (Gamry Instruments Inc., Warminster, PA, USA) was used to control the electrode potentials. Scanning probe microscopy (SPM) and nanoindentation tests were performed inside the electrochemical cell while the sample surface was immersed in the electrolyte.

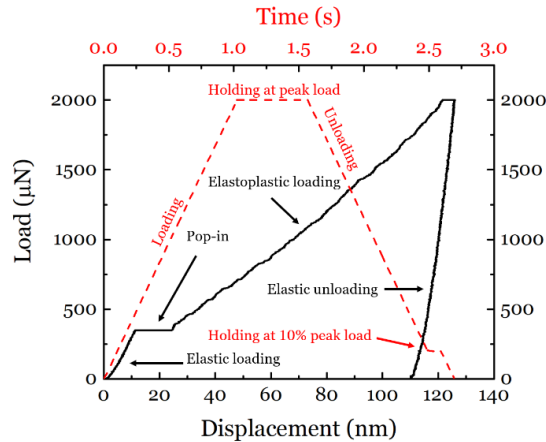


Figure 3. Nanoindentation load function (red) and a typical resulted load–displacement curve (black).

Before the ECNI test, the polarization curve of the ASS sample was measured at a scanning rate of 5 mV/s using the same setup as in the ECNI test, and the results are shown in Figure 4. The polarization curve was repeated at least three times, but only one plot is shown in the figure for clarity.

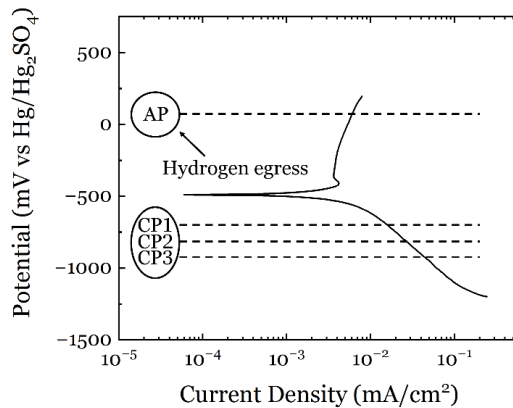


Figure 4. Polarization curve of the tested ASS at a scanning rate of 5 mV/s. AP is the anodic potential of +100 mV, CP1 is the cathodic potential of −740 mV, CP2 is the cathodic potential of −808 mV and CP3 is the cathodic potential of −884 mV.

The polarization curve shows the typical passive behavior of an ASS in a slightly acidic solution. The polarization curve shows three potential domains, i.e., cathodic, E_{corr} , and anodic. The cathodic domain comprises the potential range below −500 mV (corresponding to the corrosion potential, E_{corr}), where the current is determined by the reduction of dissolved oxygen as it corresponds to a slightly acidic medium (pH of 6.22). The second potential domain is characterized by the transition from cathodic to anodic current at the corrosion potential, E_{corr} (−500 mV). At E_{corr} , the speed of the anodic and

cathodic reaction is equal. The third domain corresponds to the anodic region, where oxidation of the metal takes place. In this case, this is a passive metal and two phenomena are observed in the anodic region: (1) active dissolution of the metal (−500 to −400 mV) characterized by an increase in current, and (2) passivation of the metal starting at −400 mV, which is characterized by a constant current density due to the passive film formation (a very thin, between 2 and 10 nm, homogeneous and uniform oxide layer mostly composed of chromium oxides builds up). At the tested conditions, no transpassive region (dissolution of the passive film and other substances) is visible in the polarization curve.

The electrode potentials chosen for the ECNI tests are denoted in Figure 4 with AP, CP1, CP2, and CP3. The testing sequence is presented in Table 2. The AP is the anodic potential located in the passive region of the ASS, and at this condition a nanometric thin oxide film (mostly chromium oxide) is present on the surface of the metal. The cathodic potentials (CP1 to CP3) are located in different regions of the cathodic domain where different reactions take place. The electrolyte chosen for this study is an aerated aqueous solution with a slightly acidic pH. Therefore, the cathodic reactions expected are the following:

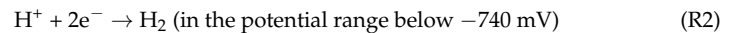
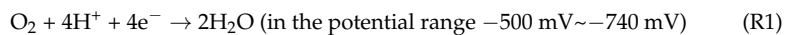


Table 2. Sequence of the testing conditions.

Steps	Testing Condition	Potential	Charging Time	ECNI Time
1	Air	-	0	24 min
2	CP1	−740 mV	30 min	16 min
3	CP2	−808 mV	10 min	23 min
4	CP3	−884 mV	15 min	20 min
5	AP	+100 mV	2 h	13 min

At CP1 (−740 mV), no or very little hydrogen evolution is expected in the current testing conditions since this value corresponds to the redox potential of hydrogen at pH 6.22 [44]. In the potential range between E_{corr} and CP1, oxygen is present in the solution and the metal surface will be passive even though a cathodic potential is being applied. In this potential range, only reaction 1 takes place. At CP2 and CP3, both reduction reactions (1 and 2) take place simultaneously and hydrogen gas starts to form on the surface of the stainless steel, promoting depassivation of the metal surface (i.e., a very thin passive film is still expected, thinner than for AP and CP1). The reduction reaction 2 exclusively takes place at electrode potentials below −1200 mV where the slope of the cathodic curve changes. At electrode potentials below −1200 mV no passive film is expected on the metal surface and only hydrogen evolution will take place.

The testing conditions are shown in Table 2. The testing procedure (including nanoindentation) was as follows: first, a freshly electropolished sample was mounted in the electrochemical cell and tested in air conditions. Then, the cathodic potentials were applied while the electrolyte was added to the sample. The nanoindentation tests were performed in different locations of the same grain after cathodic polarization (CP) by the time indicated in Table 2. The polarization plus testing sequence was repeated until all the electrode potentials were tested. The last step was done at the anodic potential (AP) indicated in Figure 4 and Table 2. Note that the AP time was intentionally designed longer than CPs to egress the hydrogen as much as possible. After the nanoindentation testing of each polarization sequence, the topography of the sample surface was inspected by SPM.

2.4. Statistical Analysis

The statistics collected from the nanoindentation tests are presented using a box plot (or box-whisker plot) in the following sections for better visibility of the data and the

associated statistical distribution. The interpretation of the plot is shown in Figure 5. The major shaded box symbol in Figure 5 shows the data range by their first (Q1) and third (Q3) quartiles (i.e., 25% and 75%), which is defined as the interquartile range (IQR). In the shaded box, the median value and the mean value are presented by a smaller box and a cross-line, respectively. The upper and lower whiskers show the 95th percentile and the 5th percentile, respectively, excluding any outliers. The outliers are also plotted as diamond symbols. Note that not all data sets have outliers. In the current study, at least 25 repetitions were performed for each nanoindentation testing condition.

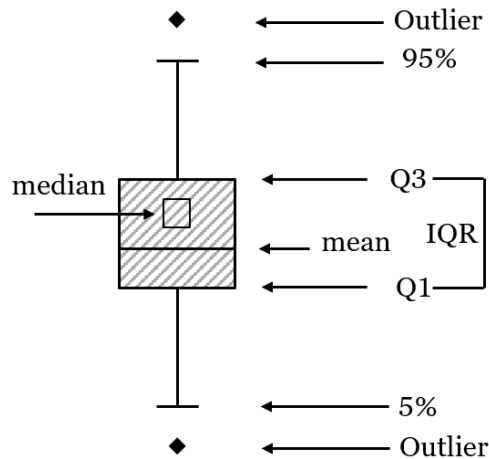


Figure 5. Interpretation of the box plot.

3. Results

3.1. Load-Displacement Curves

The sequence of the testing conditions applied to the sample are given in Table 2 and the representative load–displacement (LD) curves resulting from the nanoindentations under different potentials are shown in Figure 6a. All the LD curves clearly show four stages, namely elastic loading, pop-in, elastoplastic loading, and the final elastic unloading. When measured in air and under AP, the LD curves are very similar, while there is a clear change in the LD curves under CP. Note that the CP conditions were sequentially applied after the air condition and before the AP condition. Therefore, the LD behavior experienced a detectable change under CP and recovered to that under the initial air condition. Based on the LD results, special attention is paid to the variations (including hardness, reduced modulus, pop-in load, and pop-in width) at different electrochemical potentials, and a comprehensive analysis of the behavior of the selected steel is performed. The surface roughness was scanned after each set of tests and the scanning results are shown in Figure 6b. The SPM images do not reveal significant roughness on the surface after the individual polarization, and thus it can be concluded that the changes in the material behavior were due to the dissolved hydrogen and not to the changes in the surface conditions. Furthermore, the holding stage at 10% peak load in the unloading segment (see Figure 3) did not reveal significant changes in the LD curves for all conditions. Therefore, the thermal drift can be neglected in the ECNI procedure. The post-analysis results from the LD curves are presented in the following sections.

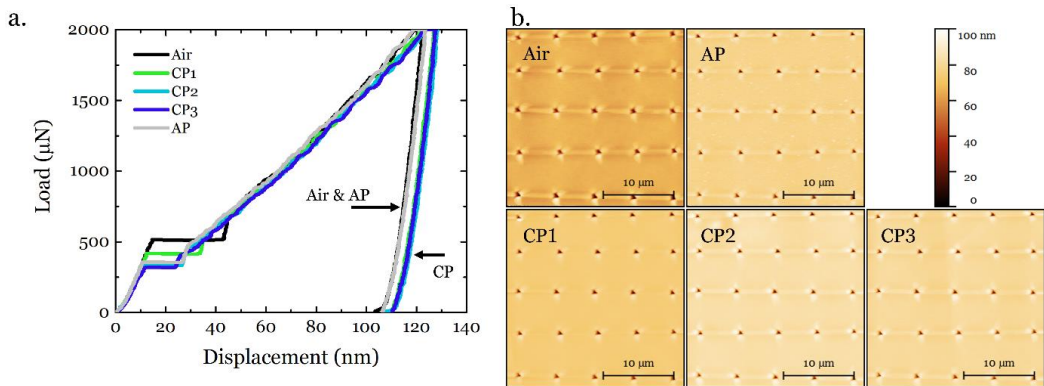


Figure 6. (a). Representative LD curves for different charging conditions and (b). the corresponding SPM images. Note the color scale applies to all SPM images.

3.2. Hardness and Elastic Moduli

A deeper analysis of the hydrogen effect on mechanical properties is performed and the LD curves were used to extract hardness and elastic modulus according to the Oliver-Pharr method. The resulting hardness (H) values and effective Young's moduli (reduced moduli E_r) can be calculated from Equations (1) and (2) [45]:

$$H = \frac{P_{max}}{A_c} \quad (1)$$

$$E_r = \frac{S}{2\beta} \sqrt{\frac{\pi}{A_c}} \quad (2)$$

where P_{max} is the maximum applied load and A_c is the tip area function that represents the projected area at a given contact depth h_c , S is the material stiffness, and β is a correction factor depending on the tip geometry (1.034 for a Berkovich indenter) as in Equation (3):

$$h_c \cong h_{max} - 0.75 \frac{P_m}{S} \quad (3)$$

In Equation (3), h_{max} represents the maximum displacement reached by the tip and the stiffness S is extracted from the initial unloading slope of the LD curves.

By combining the above equations, the hardness and reduced modulus can be calculated from the LD curves, and the results are presented in Figure 7. Without any electrochemical treatment in air, the specimen showed a mean hardness of 2.74 GPa. When CP1 was applied, the hardness slightly decreased to 2.67 GPa (about 2.5%). By further increasing the polarization potential to CP2 and CP3, the hardness recovered to 2.71 GPa and 2.72 GPa, respectively. By applying AP at +100 mV, the hardness fully recovered to 2.76 GPa, which is slightly higher than that in the air condition. On the other hand, the reduced modulus has a slightly different trend. The initial reduced modulus was 201.6 GPa in the air condition. When applying hydrogen charging at CP1~3, it decreased to 185.3 GPa, 179.0 GPa, and 180.1 GPa, respectively. After the egression of hydrogen under AP, the reduced modulus increased to 184.2 GPa, which is still lower than the air case.

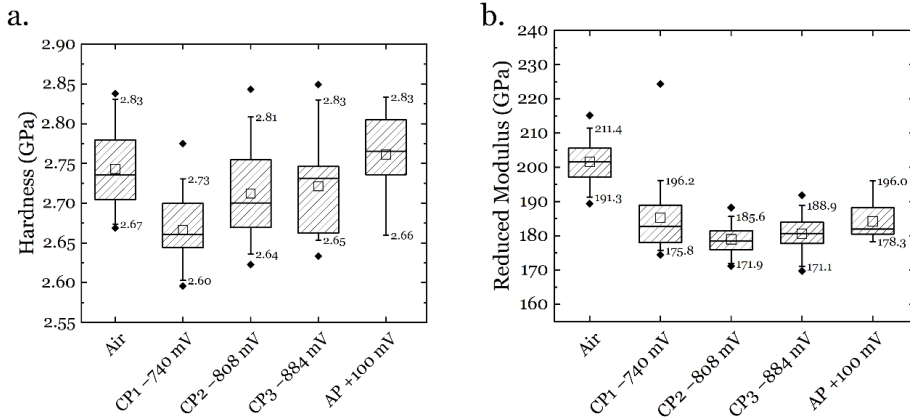


Figure 7. (a). Hardness and (b). reduced modulus under different charging conditions.

3.3. Pop-In Behavior

The pop-in phenomenon captured by the nanoindentation technique is believed to be triggered by the onset of plastic deformation [46], and upon in-situ hydrogen charging, a lowered pop-in load is always observed [47,48]. The pop-in data from the ECNI tests in the current study are summarized in Figure 8. The pop-in procedure can be depicted by the energy-based model proposed by Wang et al. [40].

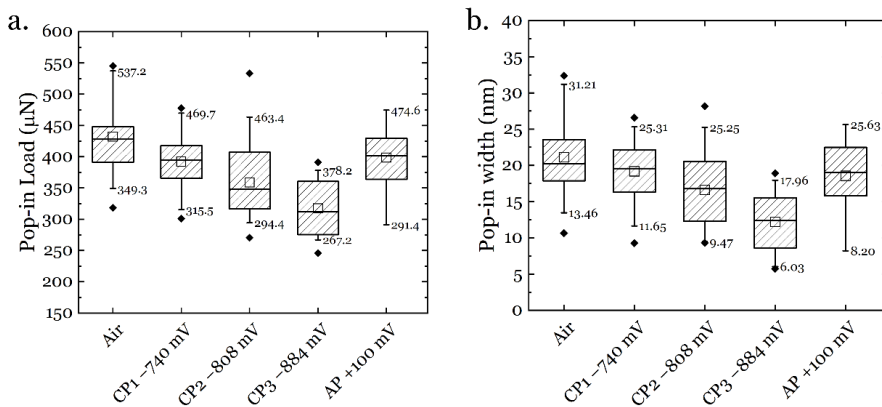


Figure 8. Pop-in data from the ECNI under different charging conditions: (a). pop-in load; (b). pop-in width.

Assuming the onset of plastic deformation results from the elastic stored energy (i.e., the loading segment before the pop-in starts), based on the energy balance principle that the elastic stored energy is consumed by the formation of dislocations with the associated interaction and lattice friction, the following mathematical relationship in Equation (4) can be assumed:

$$W_e = W_i^{tot} + N \cdot W_s + W_f^{tot} \quad (4)$$

where W_e is the elastic stored energy, W_i^{tot} is the total interaction energy between dislocation, N is the number of generated dislocation loops, W_s is the dislocation line energy, and W_f^{tot} is the total friction energy on dislocation motion during pop-in.

Since the elastic loading part can be described by the Hertzian contact theory, the stored energy can be described by Equation (5):

$$W_e = \int_0^{h_1} P(h)dh = \int_0^{h_1} \frac{4}{3} E_r h^{\frac{3}{2}} R^{\frac{1}{2}} dh = \frac{8}{15} E_r R^{\frac{1}{2}} h_1^{\frac{5}{2}} \quad (5)$$

where P and h denote the load and depth during indentation, and h_1 means the start depth of the pop-in. R is the tip radius that equals to 1875 nm in the current study.

The interaction energy between two circular prismatic dislocation loops can be described as Equation (6):

$$W_i = \frac{\mu b^2}{1-\nu} r \left(\ln \frac{8r}{d} - 1 \right) \quad (6)$$

where μ stands for the shear modulus, b denotes the magnitude of the Burgers vector, ν the Poisson's ratio, and d the distance between dislocation loops which is assumed to be equal to b , considering dislocation loops are piled on the close-packed crystallographic plane. The radius of dislocation loops r is determined from the stress field beneath the indenter by assuming the 98% maximum shear stress, as proposed in [40]. Therefore, the radius r can be correlated with the contact depth a_c in Equation (7):

$$r = 0.29a_c = 0.29 \times \sqrt[3]{\frac{3PR}{4E_r}} \quad (7)$$

The total interaction energy is calculated by considering the interactions between each dislocation loop with all the rest loops, which gives the following relationship in Equation (8):

$$W_i^{tot} = \frac{\mu b^2}{1-\nu} r \left(\left\{ \sum_{j=1}^{N-1} j \left(\ln \left(\frac{8r}{d} \right) \right) - \sum_{j=1}^{N-1} \ln(j!) - \sum_{j=1}^{N-1} j \right\} \right) \quad (8)$$

The number of generated dislocation loops can be correlated with the pop-in width Δh in Equation (9):

$$N = \frac{\Delta h}{2b} \quad (9)$$

The dislocation line energy is expressed by Equation (10):

$$W_s = \frac{\mu b^2}{2(1-\nu)} r \left(\ln \frac{8r}{\rho} - 1 \right) \quad (10)$$

Here, ρ is the radius of dislocation core which is assumed to be equal to $b/2$.

By combining Equations (4)–(10), the total friction energy W_f^{tot} for dislocation motion during pop-in can be calculated. The unit friction energy (W_f , i.e., the energy consumed for a single dislocation loop to move a distance of b) can be correlated with the total friction energy by Equation (11):

$$W_f \cdot \frac{N(N-1)}{2} = W_f^{tot} \quad (11)$$

Finally, the unit friction energy for individual dislocation motion and the corresponding energy consumption distribution for the entire pop-in procedure can be evaluated. The results are presented in Figure 9. Although the calculated friction energy with the scatter range looks similar between different charging conditions, a consistent trend can still be depicted regarding the hydrogen ingress and egression (see Figure 9a). In the air condition, the unit friction energy was calculated to be 1.84×10^{-15} J, and after charging at CP1 to CP3, the unit friction energy increased to 2.05×10^{-15} J, 2.28×10^{-15} J and 4.34×10^{-15} J, respectively. After the hydrogen egression by AP, the unit friction energy recovered to the level of 2.09×10^{-15} J. When considering the energy consumption categories

(see Figure 9b), the friction occupied 64% of the total energy during pop-in, and this value increased to 65%, 67%, and 79% under CP1, CP2, and CP3, respectively. After hydrogen egression, this portion dropped again to 66%. The competition was mainly between the friction and the dislocation interactions in the energy consumption, and in comparison, the energies consumed by dislocation line formation did not vary noticeably and engaged about 1~2% for all the testing conditions.

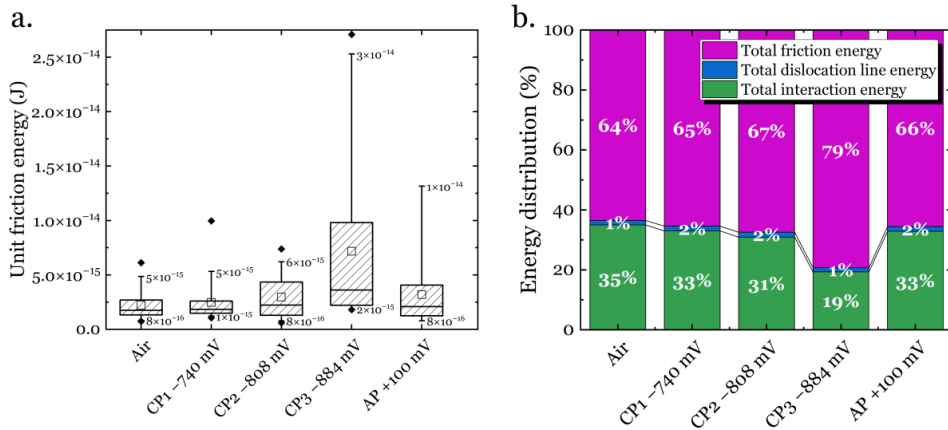


Figure 9. Lattice friction analysis based on the pop-in behavior from ECNI under different charging conditions: (a) unit friction energy; (b) energy consumption distribution during pop-in.

3.4. Homogeneous Dislocation Nucleation (HDN)

During nanoindentation, the contact between the tip and the sample surface is under elastic loading until the first dislocation nucleation occurs, which represents the beginning of plasticity, marked by the pop-in in Figure 3. The microstructure of well-annealed equiaxial grains and proper electropolishing indicate a relatively low dislocation density of the tested specimen (usually about 10^{10} to 10^{14} m⁻², corresponding to an average dislocation spacing of approximately 1–10 μ m [39], which is much larger than the indentation depth). Thus, it is reasonable to consider that at the onset of the pop-in during nanoindentation, the maximum shear stress under the indenter, τ_{max} , can be the shear stress resulting in HDN. According to continuum mechanics [49,50], the value of the maximum shear stress τ_{max} that appears at the position $z_{\tau(max)}$ is given by:

$$\tau_{max} = 0.31 \left(\frac{6E_r^2}{\pi^3 R^2} P \right)^{\frac{1}{3}} \quad (12)$$

$$z_{\tau(max)} = 0.48 \left(\frac{3PR}{4E_r} \right)^{\frac{1}{3}} \quad (13)$$

where E_r is the reduced modulus, R is the tip radius, and P is the pop-in load. The tip radius is extracted from fitting a Hertzian model to the elastic loading part of the LD curves, which is 1875 nm for the current study. Thus, the maximum shear stress obtained from Equation (12) is responsible for the HDN at $z_{\tau(max)}$ below the tip.

According to classic dislocation theory, the formation of a circular dislocation loop with radius r requires a free energy given by [49]:

$$\Delta G = 2\pi r \gamma_{dis} - \pi r^2 b \tau_{max} + \pi r^2 \gamma \quad (14)$$

The first term in the equation, $2\pi r\gamma_{dis}$ represent the line energy of the dislocation loop, the second term, $\pi r^2 b\tau_{max}$ describe the work needed for expanding the dislocation loop, while the latest one is the formation of the stacking fault energy (SFE). Thus, γ_{dis} (Equation (15)) represents the elastic self-energy of a full circular dislocation loop in an infinite isotropic elastic solid, γ is the SFE in mJ/m^2 (which is $22.83 \text{ mJ}/\text{m}^2$ according to Equation (16) [51]), and b is the Burgers vector for dislocation (0.254 nm [41]).

$$\gamma_{dis} = \frac{2 - \nu}{1 - \nu} \frac{\mu b^2}{8\pi} \left(\ln \frac{4r}{\rho_{core}} - 2 \right) \quad (15)$$

$$\gamma = 2.2 + 1.9\text{Ni} - 2.9\text{Si} + 0.77\text{Mo} + 0.5\text{Mn} + 40\text{C} - 0.016\text{Cr} - 3.6\text{N} \quad (16)$$

where μ is the shear modulus (80 GPa for the 316L steel [41]), ν is Poisson's ratio (0.3 [41]), and ρ_{core} represents the dislocation core radius.

Hence, by using Equation (15), the free energy required for a dislocation loop formation can be expressed as:

$$\Delta G = \frac{2 - \mu}{1 - \mu} \frac{Gb^2r}{4} \left(\ln \frac{4r}{\rho_{core}} - 2 \right) - \pi r^2 b\tau_{max} + \pi r^2 \gamma \quad (17)$$

The free energy change of HDN as a function of dislocation loop radius can be calculated by combining Equations (12)–(17), and the results are presented in Figure 10. The calculated curves have a maximum free energy ΔG^* value at a critical loop radius r^* . For the formation of a stable dislocation loop larger than r^* , the activation energy has to pass the barrier of ΔG^* . From Figure 10, considering the air condition as an initial reference, the ΔG^* and the r^* values are increasing with a higher cathodic potential, and after anodic discharging, the ΔG^* and the r^* values recovered towards the air condition, but not completely (the curve from AP is almost overlapping with the CP1 condition). This result is not surprising since at CP1 not enough hydrogen is formed. Indeed, since CP1 corresponds to the redox potential of hydrogen in the given testing conditions, one should expect a fully passivated surface in the material, very similar to the AP condition. In order to fully depassivate a stainless-steel surface, the cathodic potential applied should be below the redox potential for hydrogen. In the present study, this was found to be below -1200 mV (see Figure 4).

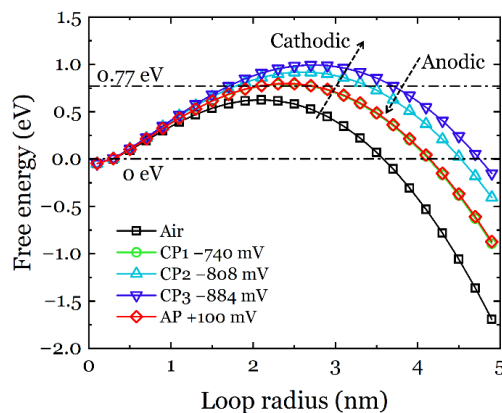


Figure 10. Free energy change of HDN as a function of dislocation loop radius calculated from the ECNI results.

The constants used in the current study are summarized in Table 3.

Table 3. The constants used in the current study.

Parameter	Symbol	Value	Reference
shear modulus	μ	80 GPa	[41]
tip radius	R	1875 nm	(extracted from LD curves)
Poisson's ratio	ν	0.3	[41]
Burgers vector	b	0.254 nm	[41]
stacking fault energy	γ	22.83 mJ/m ²	[51]

4. Discussion

4.1. The Influence of Hydrogen on the Pop-In Behavior

The influence of hydrogen on the pop-in behavior of materials during in-situ ECNI has been a focus since the development of this technique, as the change in pop-in is always noticeable in the testing procedure. A general trend is that hydrogen reduces both pop-in load and pop-in width [39].

It has been proposed that the pop-in width can be related to the number, mobility, and interactions between dislocations during pop-in [52–56]. Recently, this procedure was modeled [40] using the energy balance criteria and the analysis for the current work has been presented in Section 3.3. From Figure 9a, the hydrogen evolution by CP has a clear enhancing effect on the lattice friction for dislocation motion, and this enhancement becomes greater when the potential increased in the cathodic direction. The accumulation of hydrogen atoms in the specimen could generate a Cottrell-like atmosphere that provides more resistance to the dislocation motion in the framework of the solute drag theory [57,58] (further discussion in Section 4.3). Therefore, more energy needs to be consumed to overcome the friction during the onset of plastic deformation. It is worth noting that the total energy consumption by friction quantitatively increases as the electrode potential increases in the cathodic direction (Figure 9b), which provides more evidence on the hydrogen-induced friction hypothesis. When the hydrogen was discharged by applying an anodic potential, the friction recovered towards the original level, though not completely. This irreversible property change could possibly be ascribed to three reasons: (1) incomplete hydrogen egression, (2) hydrogen trapping in the material after CP sequences, and (3) surface modifications due to charging. The first two points have been widely reported in the literature [40,52]. For the third point, one can see from the SPM images in Figure 6b that the specimen surface did not change in a noticeable manner, and the surface roughness was still in an appropriate range (surface height variation of ~1 nm before test, and ~2 nm after test). Therefore, the irreversible friction due to surface modification can be excluded.

From the pop-in load, the free energy change can be depicted from the model presented in Section 3.4, which describes the HDN procedure. Based on thermodynamics, the critical energy barrier ΔG^* (the local maxima of the free energy curves in Figure 10) has to be overcome in order to make the formation of a dislocation loop energetically stable. According to Rice and Beltz [59], the available energy at room temperature for dislocation nucleation is roughly 0.77 eV (calculated by $30kT$, where k is Boltzmann constant and T is temperature), which is drawn as a reference line in Figure 10. It can be seen that the free energy curves from the hydrogen-free air condition and the AP and CP1 conditions are below the 0.77 eV threshold, which means that spontaneous dislocation nucleation is thermodynamically possible. Hydrogen charging at CP2 and CP3 clearly made the local maxima of the free energy curves higher than 0.77 eV, and therefore spontaneous HDN under these conditions is energetically unfavorable, and an additional energy source is needed. Comparing the testing conditions, hydrogen charging by cathodic polarization was the only parameter changed between the sequences. Therefore, it is reasonable to conclude that the dissolved hydrogen provided the energy needed for HDN. According to the defactant (defect acting agent) theory [60], hydrogen can act as a defactant that reduces the formation energy of defects such as dislocations. Therefore, the dissolution of hydrogen in the specimen made the nucleation of dislocations easier than the hydrogen-free case, and thus the pop-in load decreased. This effect is also more pronounced with a more

negative cathodic potential, i.e., a larger amount of hydrogen generated and ultimately absorbed in the material. CP1 showed a ΔG^* at the same level as the AP since in both cases a passive film was present on the surface of the ASS due to the very little hydrogen evolution at CP1. Indeed, hydrogen absorption in the metal is a stepwise process that depends on the diffusion kinetics. Hydrogen evolution reaction proceeds through three reaction steps, (1) Volmer (adsorption), (2) Heyrovsky (electrochemical desorption), and (3) Tafel (chemical desorption), where the latter is typically negligible in an electrochemical process. The hydrogen adsorption and absorption processes cannot be separated, i.e., once hydrogen has been adsorbed on the metal surface, it will absorb into the metal following the Fick's law [61]. Therefore, a critical amount of hydrogen (driven by the electrode potential applied) is needed in order to trigger significant degradation in the material properties. However, this critical amount is difficult to precisely measure in the material in-situ and in-real-time due to technical limitations. However, using the polarization curve (the current density at a given electrode potential) and assuming that the only cathodic reaction is hydrogen evolution, one could estimate the amount of hydrogen produced on the surface of the stainless steel. The amount of hydrogen absorbed in the material will ultimately depend on the diffusion kinetics and the cathodic potential applied.

4.2. Hydrogen Influence on Mechanical Properties

In the current study, a hydrogen-induced softening was observed at the cathodic potential (CP1) that was right at the redox potential for hydrogen (none or very little hydrogen evolution). A weaker softening effect has happened at the other two cathodic potentials (CP2 and CP3) instead of the expected hydrogen-induced hardening effect that is typically observed in conventional ECNI tests at cathodic potentials well below the redox potential for hydrogen evolution [35]. Worth noticing is the short charging periods (only 10 to 30 min per potential sequence) used in this work (Table 2) and the very small volume of electrolyte used. In addition, the electrolyte used was an aqueous electrolyte with very low viscosity, which promotes a fast track for hydrogen bubbles to escape the solution. This can possibly result in very different hydrogen concentration and diffusion in the material compared to other works and the HELP-related softening mechanisms [62]. Though the lattice friction has been enhanced by the introduction of hydrogen, this was modeled only until the onset of plastic deformation, where the massive dislocation motion and the associated dislocation–hydrogen interaction during motion was less pronounced. The hardness measured by ECNI was based on the projected area of the final imprint and the applied load. Since the eventual appearance of the imprint was determined from all four stages of the ECNI (see Figure 3), the elastoplastic loading regime coupled with massive dislocation motion and dislocation–hydrogen interaction could have given a strong contribution to the final hardness.

The hydrogen-induced softening effect observed by uniaxial tensile testing in similar austenitic steels has been reported in literature [63,64]. This can possibly be explained by the HELP mechanism. In 2001, Robertson [65] published the experimental proof for the HELP mechanism that upon in-situ hydrogen charging, the spacing between dislocations became visibly smaller in austenitic steels. This was attributed to the hydrogen-enhanced dislocation mobility. In later years, the conclusion was also applied to other materials such as Ni alloys [66]. It has also been stated that this hydrogen-enhanced mobility of different types of dislocations is working as long as the hydrogen atmosphere can move with the dislocations [66]. The physical reason behind this proposal has been concluded as the reduction effect of hydrogen on the short-range energy barrier of the thermally activated dislocation motion [67,68]. Considering the relatively low amount of hydrogen expected in the current study (specially at CP1), it is not surprising to assume that the environmental conditions of the results obtained in this work fit the conditions of the HELP mechanism, and thus the decrease in hardness should be the expected result.

Indeed, when the hydrogen concentration increases, the material gradually hardens (Figure 7a). As reported in literature, multiple hydrogen-metal interaction mechanisms can

be active simultaneously in the material depending on several different parameters, among which the hydrogen concentration is a critical one [12]. As the hydrogen concentration becomes higher than the critical value, the HELP mechanism becomes less dominant, and thus the softening induced by the enhanced dislocation mobility is replaced by other mechanisms. To prove this hypothesis, tests at more negative CPs were performed, and the results of the hardness measurements are shown in Figure 11. It can be seen that when the CP further increased to -1200 mV and -1400 mV, the hardness increased systematically. When the cathodic potential of -1500 mV was reached, the hardness showed an abrupt increase. This increase in hardness was followed by the formation of slip lines and/or martensite formation on the surface, as can be seen from the embedded SPM image in Figure 11. Considering the friction analysis in Section 3.3 and Figure 9, the importance of friction is becoming more and more important with a more negative CP. Therefore, it can be speculated that the friction plays a major role in the hardening behavior at higher hydrogen concentrations, i.e., when only reduction reaction 2 dominates the cathodic charging.

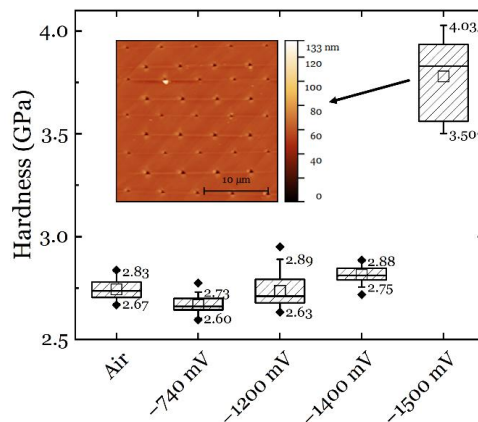


Figure 11. Hardness measured at relatively higher CPs. The hydrogen-free and low CP cases are presented for reference. Note that all measurements were conducted in the same grain and thus the orientation influence can be eliminated.

4.3. Permanent Change in Material

As mentioned in Section 4.1, the material properties did not fully recover to the level in air condition after the application of AP at $+100$ mV, and the surface modification was excluded from the possible reasons based on the result in Figure 6b. However, if the CP was further increased to -1500 mV, a clear topographic change could be observed in the material (Figure 11). A similar phenomenon has also been observed in austenitic high-entropy alloys, and the reason for this was the hydrogen-induced internal stress leading HISS (hydrogen-induced surface steps) [69] and/or hydrogen-induced martensitic transformation [70]. The hydrogen-induced surface modifications, either in the form of surface steps or martensitic transformation, can cause irreversible changes in the mechanical performance of the material. Such a permanent change did not happen in CP1~3 and AP charging conditions due to the lack of enough hydrogen and/or the short polarization times. The observed differences in the pop-in behavior and the friction and HDN analyses are therefore the most plausible reason for the intrinsic modification to the material.

On the other hand, the possible martensitic transformation found when the CP was further increased to -1500 mV (Figure 11) shows that the alloy has enough carbon solutes (Table 1) to trigger a permanent transformation in the material. As mentioned in Section 4.1, hydrogen could have generated a Cottrell-like atmosphere that hinders dislocation motion [57]. It may thus be speculated that hydrogen changes the Cottrell atmospheres created by larger solute atoms (carbon or nitrogen, Table 1) by interacting with them. For

example, Abraham and Altstetter studied the effect of cathodically charged hydrogen on the yield strength of a 310 s ASS and found an increase in the yield strength with increasing hydrogen content [19]. Since the yielding (discontinuous yielding) can be correlated with the dislocation interactions with the Cottrell atmospheres formed by carbon and nitrogen solutes, it is naturally reasonable to consider the effect of hydrogen on such interactions. This effect was also confirmed by testing pre-deformed specimens, where the interstitial atoms were redistributed due to the plastic deformation [19]. Zielinski et al. proposed that Cottrell atmospheres composed of hydrogen atoms may decrease the dislocation mobility in iron, and thus a change in the internal friction can be observed between the hydrogen-free and the hydrogen-charged iron [71]. The nature of the Cottrell atmosphere (whether created by hydrogen atoms or carbon/nitrogen solutes) needs more advanced techniques to be investigated, but all the discussion supports the conclusion that hydrogen is increasing the internal friction in the material.

5. Conclusions

The current work presents a study on the effect of hydrogen in a 316L ASS using in-situ electrochemical nanoindentation (ECNI) techniques. By in-situ polarizing the specimen with different cathodic and anodic potentials, the influence on the nanomechanical properties induced by hydrogen ingress and egress has been examined. The following conclusions have been drawn:

- Cathodic hydrogen charging increases the lattice friction both in the amount and the proportion during the onset of plastic deformation, and the lattice friction recovers towards the hydrogen-free case after anodic discharging.
- The cathodically charged hydrogen promotes the homogeneous dislocation nucleation during nanoindentation, which can be explained by the framework of the defacant theory.
- The softening effect of hydrogen can be observed at cathodic potentials up to the redox potential for hydrogen evolution, which can be explained by the HELP mechanism.
- When charging at higher cathodic potentials (above the redox potential for hydrogen evolution), hydrogen-induced surface steps can be observed, which contribute permanent changes (hardening) to the material.

Author Contributions: Conceptualization, A.B. and D.W. (Di Wan); methodology, A.B. and D.W. (Di Wan); validation, D.W. (Dong Wang), N.E. and D.W. (Di Wan); data curation, A.B.; writing—original draft preparation, A.B.; writing—review and editing, D.W. (Dong Wang), N.E. and D.W. (Di Wan); supervision, N.E. and D.W. (Di Wan). All authors have read and agreed to the published version of the manuscript.

Funding: This research was funded by the Research Council of Norway grant number 10290803 and 294739. The APC was funded by NTNU's Publishing Fund.

Institutional Review Board Statement: Not applicable.

Informed Consent Statement: Not applicable.

Data Availability Statement: Data are available on request to the corresponding author.

Acknowledgments: A. Basa would like to acknowledge the Research Council of Norway for providing financial support to perform the experimental part of this paper through the PETROMAKS Program (10290803). D. Wang is grateful to the Research Council of Norway for his postdoc scholarship through the HyLINE project (294739).

Conflicts of Interest: The authors declare no conflict of interest.

References

1. Johnson, W.H. On Some Remarkable Changes Produced in Iron and Steel by the Action of Hydrogen and Acids. *Proc. R. Soc. Lond.* **1875**, *23*, 168–179. [[CrossRef](#)]
2. Beachem, C.D. A new model for hydrogen-assisted cracking (hydrogen “embrittlement”). *Metall. Mater. Trans. B* **1972**, *3*, 441–455. [[CrossRef](#)]
3. Birnbaum, H.K.; Sofronis, P. Hydrogen-enhanced localized plasticity—A mechanism for hydrogen-related fracture. *Mater. Sci. Eng. A* **1994**, *176*, 191–202. [[CrossRef](#)]
4. Wang, S.; Nagao, A.; Sofronis, P.; Robertson, I.M. Hydrogen-modified dislocation structures in a cyclically deformed ferritic-pearlitic low carbon steel. *Acta Mater.* **2018**, *144*, 164–176. [[CrossRef](#)]
5. Gerberich, W.W.; Oriani, R.A.; Lji, M.J.; Chen, X.; Foecke, T. The necessity of both plasticity and brittleness in the fracture thresholds of iron. *Philos. Mag. A* **1991**, *63*, 363–376. [[CrossRef](#)]
6. Oriani, R.A. The diffusion and trapping of hydrogen in steel. *Acta Metall.* **1970**, *18*, 147–157. [[CrossRef](#)]
7. Troiano, A.R. The Role of Hydrogen and Other Interstitials in the Mechanical Behavior of Metals (1959 Edward De Mille Campbell Memorial Lecture). *Metallogr. Microstruct. Anal.* **2016**, *5*, 557–569. [[CrossRef](#)]
8. Barrera, O.; Bombac, D.; Chen, Y.; Daff, T.D.; Galindo-Nava, E.; Gong, P.; Haley, D.; Horton, R.; Katzarov, I.; Kermode, J.R.; et al. Understanding and mitigating hydrogen embrittlement of steels: A review of experimental, modelling and design progress from atomistic to continuum. *J. Mater. Sci.* **2018**, *53*, 6251–6290. [[CrossRef](#)]
9. Nagumo, M. Hydrogen related failure of steels—A new aspect. *Mater. Sci. Technol.* **2004**, *20*, 940–950. [[CrossRef](#)]
10. Lynch, S. Hydrogen embrittlement phenomena and mechanisms. *Corros. Rev.* **2012**, *30*, 105–123. [[CrossRef](#)]
11. Lynch, S.P. Environmentally Assisted Cracking—Overview of Evidence for an Adsorption-Induced Localized-Slip Process. *Acta Metall.* **1988**, *36*, 2639–2661. [[CrossRef](#)]
12. Djukic, M.B.; Bakic, G.M.; Sijacki Zeravcic, V.; Sedmak, A.; Rajjic, B. The synergistic action and interplay of hydrogen embrittlement mechanisms in steels and iron: Localized plasticity and decohesion. *Eng. Fract. Mech.* **2019**, *216*, 106528. [[CrossRef](#)]
13. Kaya, Y.; Kahraman, N. An investigation into the explosive welding/cladding of Grade A ship steel/AISI 316L austenitic stainless steel. *Mater. Des.* **2013**, *52*, 367–372. [[CrossRef](#)]
14. Zhu, M.; He, F.; Yuan, Y.; Guo, S.; Wei, G. A comparative study on the corrosion behavior of CoCrNi medium-entropy alloy and 316L stainless steel in simulated marine environment. *Intermetallics* **2021**, *139*, 107370. [[CrossRef](#)]
15. Hinds, G.; Wickström, L.; Mingard, K.; Turnbull, A. Impact of surface condition on sulphide stress corrosion cracking of 316L stainless steel. *Corros. Sci.* **2013**, *71*, 43–52. [[CrossRef](#)]
16. Lacombe, P.; Baroux, B.; Béranger, G.; Colombier, L.; Hochmann, J. *Stainless Steels*; Les Editions de Physique: Les Ulis, France, 1993.
17. Alvaro, A.; Wan, D.; Olden, V.; Barnoush, A. Hydrogen enhanced fatigue crack growth rates in a ferritic Fe-3 wt % Si alloy and a X70 pipeline steel. *Eng. Fract. Mech.* **2019**, *219*, 106641. [[CrossRef](#)]
18. Wan, D.; Alvaro, A.; Olden, V.; Barnoush, A. Hydrogen-enhanced fatigue crack growth behaviors in a ferritic Fe-3wt%Si steel studied by fractography and dislocation structure analysis. *Int. J. Hydrogen Energy* **2019**, *44*, 5030–5042. [[CrossRef](#)]
19. Abraham, D.P.; Altstetter, C.J. The effect of hydrogen on the yield and flow stress of an austenitic stainless steel. *Metall. Mater. Trans. A* **1995**, *26*, 2849–2858. [[CrossRef](#)]
20. Bentley, A.P.; Smith, G.C. Phase transformation of austenitic stainless steels as a result of cathodic hydrogen charging. *Metall. Trans. A* **1986**, *17*, 1593–1600. [[CrossRef](#)]
21. Kwietniewski, C.E.F.; Renck, T.; dos Santos, F.P.; Scheid, A.; Sartori, M.; Reguly, A. Influence of stress intensity factor rate and hydrogen charging conditions on Fracture Toughness of a Super Duplex Stainless Steel. In Proceedings of the Corrosion 2018, Phoenix, AZ, USA, 15–19 April 2018; Abstract No. 10891. pp. 1–15.
22. Rozenak, P.; Zevin, L.; Eliezer, D. Internal stresses in austenitic steels cathodically charged with hydrogen. *J. Mater. Sci. Lett.* **1983**, *2*, 63–66. [[CrossRef](#)]
23. Abraham, D.P.; Altstetter, C.J. Hydrogen-enhanced localization of plasticity in an austenitic stainless steel. *Metall. Mater. Trans. A* **1995**, *26*, 2859–2871. [[CrossRef](#)]
24. Gavriljuk, V.G.; Shivanyuk, V.N.; Foct, J. Diagnostic experimental results on the hydrogen embrittlement of austenitic steels. *Acta Mater.* **2003**, *51*, 1293–1305. [[CrossRef](#)]
25. Martin, M.L.; Dadfarnia, M.; Nagao, A.; Wang, S.; Sofronis, P. Enumeration of the hydrogen-enhanced localized plasticity mechanism for hydrogen embrittlement in structural materials. *Acta Mater.* **2019**, *165*, 734–750. [[CrossRef](#)]
26. Nibur, K.; Bahr, D.; Somerday, B. Hydrogen effects on dislocation activity in austenitic stainless steel. *Acta Mater.* **2006**, *54*, 2677–2684. [[CrossRef](#)]
27. Li, Y.-F.; Zhao, L.-M.; Pan, H.-L. Hydrogen permeation behaviour and associated phase transformations in annealed AISI304 stainless steels. *Mater. Struct.* **2013**, *46*, 621–627. [[CrossRef](#)]
28. Qu, W.; Gu, C.; Zheng, J.; Zhao, Y.; Hua, Z. Effect of plastic deformation at room temperature on hydrogen diffusion of S30408. *Int. J. Hydrogen Energy* **2019**, *44*, 8751–8758. [[CrossRef](#)]
29. Rozenak, P.; Loew, A. Stress distributions due to hydrogen concentrations in electrochemically charged and aged austenitic stainless steel. *Corros. Sci.* **2008**, *50*, 3021–3030. [[CrossRef](#)]
30. Brass, A.M.; Chêne, J. Hydrogen uptake in 316L stainless steel: Consequences on the tensile properties. *Corros. Sci.* **2006**, *48*, 3222–3242. [[CrossRef](#)]

31. Ulmer, D.G.; Altstetter, C.J. Hydrogen-induced strain localization and failure of austenitic stainless steels at high hydrogen concentrations. *Acta Metall. Mater.* **1991**, *39*, 1237–1248. [[CrossRef](#)]
32. Barnoush, A.; Vehoff, H. Recent developments in the study of hydrogen embrittlement: Hydrogen effect on dislocation nucleation. *Acta Mater.* **2010**, *58*, 5274–5285. [[CrossRef](#)]
33. Sun, B.H.; Wang, D.; Lu, X.; Wan, D.; Ponge, D.; Zhang, X.C. Current Challenges and Opportunities Toward Understanding Hydrogen Embrittlement Mechanisms in Advanced High-Strength Steels: A Review. *Acta Metall. Sin.-Engl. Lett.* **2021**, *34*, 741–754. [[CrossRef](#)]
34. Lu, X.; Ma, Y.; Zamanzade, M.; Deng, Y.; Wang, D.; Bleck, W.; Song, W.W.; Barnoush, A. Insight into hydrogen effect on a duplex medium-Mn steel revealed by in-situ nanoindentation test. *Int. J. Hydrogen Energy* **2019**, *44*, 20545–20551. [[CrossRef](#)]
35. Lu, X.; Wang, D. Effect of hydrogen on deformation behavior of Alloy 725 revealed by in-situ bi-crystalline micropillar compression test. *J. Mater. Sci. Technol.* **2021**, *67*, 243–253. [[CrossRef](#)]
36. Deng, Y.; Hajilou, T.; Wan, D.; Kheradmand, N.; Barnoush, A. In-situ micro-cantilever bending test in environmental scanning electron microscope: Real time observation of hydrogen enhanced cracking. *Scr. Mater.* **2017**, *127*, 19–23. [[CrossRef](#)]
37. Depover, T.; Wan, D.; Wang, D.; Barnoush, A.; Verbeken, K. The effect of hydrogen on the crack initiation site of TRIP-assisted steels during in-situ hydrogen plasma micro-tensile testing: Leading to an improved ductility? *Mater. Charact.* **2020**, *167*, 110493. [[CrossRef](#)]
38. Wang, D.; Hagen, A.B.; Wan, D.; Lu, X.; Johnsen, R. Probing hydrogen effect on nanomechanical properties of X65 pipeline steel using in-situ electrochemical nanoindentation. *Mater. Sci. Eng. A* **2021**, *824*, 141819. [[CrossRef](#)]
39. Wang, D.; Lu, X.; Deng, Y.; Guo, X.; Barnoush, A. Effect of hydrogen on nanomechanical properties in Fe-22Mn-0.6C TWIP steel revealed by in-situ electrochemical nanoindentation. *Acta Mater.* **2019**, *166*, 618–629. [[CrossRef](#)]
40. Wang, D.; Lu, X.; Lin, M.; Wan, D.; Li, Z.; He, J.; Johnsen, R. Understanding the hydrogen effect on pop-in behavior of an equiatomic high-entropy alloy during in-situ nanoindentation. *J. Mater. Sci. Technol.* **2022**, *98*, 118–122. [[CrossRef](#)]
41. Barnoush, A.; Asgari, M.; Johnsen, R. Resolving the hydrogen effect on dislocation nucleation and mobility by electrochemical nanoindentation. *Scr. Mater.* **2012**, *66*, 414–417. [[CrossRef](#)]
42. Barnoush, A.; Basa, A.; Thaulow, C. Oxygen argon plasma treatment effect on hydrogen uptake in austenitic stainless steels. *Int. J. Hydrogen Energy* **2014**, *39*, 14120–14131. [[CrossRef](#)]
43. Djukic, M.B.; Sijacki Zeravcic, V.; Bakic, G.M.; Sedmak, A.; Rajcic, B. Hydrogen damage of steels: A case study and hydrogen embrittlement model. *Eng. Fail. Anal.* **2015**, *58*, 485–498. [[CrossRef](#)]
44. Pourbaix, M. *Atlas of Electrochemical Equilibria in Aqueous Solutions*; National Association of Corrosion Engineers: Houston, TX, USA, 1974.
45. Oliver, W.C.; Pharr, G.M. An improved technique for determining hardness and elastic modulus using load and displacement sensing indentation experiments. *J. Mater. Res.* **1992**, *7*, 1564–1583. [[CrossRef](#)]
46. Barnoush, A. Correlation between dislocation density and nanomechanical response during nanoindentation. *Acta Mater.* **2012**, *60*, 1268–1277. [[CrossRef](#)]
47. Barnoush, A.; Bies, C.; Vehoff, H. In situ electrochemical nanoindentation of FeAl (100) single crystal: Hydrogen effect on dislocation nucleation. *J. Mater. Res.* **2009**, *24*, 1105–1113. [[CrossRef](#)]
48. Barnoush, A.; Vehoff, H. In situ electrochemical nanoindentation: A technique for local examination of hydrogen embrittlement. *Corros. Sci.* **2008**, *50*, 259–267. [[CrossRef](#)]
49. Anderson, P.M.; Hirth, J.P.; Lothe, J. *Theory of Dislocations*, 3rd ed.; Cambridge University Press: Cambridge, UK, 2017; p. 718.
50. Gerberich, W.W.; Nelson, J.C.; Lilleodden, E.T.; Anderson, P.; Wyrobek, J.T. Indentation induced dislocation nucleation: The initial yield point. *Acta Mater.* **1996**, *44*, 3585–3598. [[CrossRef](#)]
51. Meric de Bellefon, G.; van Duysen, J.C.; Sridharan, K. Composition-dependence of stacking fault energy in austenitic stainless steels through linear regression with random intercepts. *J. Nucl. Mater.* **2017**, *492*, 227–230. [[CrossRef](#)]
52. Stenerud, G.; Johnsen, R.; Olsen, J.S.; He, J.Y.; Barnoush, A. Effect of hydrogen on dislocation nucleation in alloy 718. *Int. J. Hydrogen Energy* **2017**, *42*, 15933–15942. [[CrossRef](#)]
53. Bahr, D.F.; Kramer, D.E.; Gerberich, W.W. Non-linear deformation mechanisms during nanoindentation. *Acta Mater.* **1998**, *46*, 3605–3617. [[CrossRef](#)]
54. Liu, G.; Song, M.; Liu, X.; Ni, S.; Wang, S.; He, Y.; Liu, Y. An investigation of the mechanical behaviors of micro-sized tungsten whiskers using nanoindentation. *Mater. Sci. Eng. A* **2014**, *594*, 278–286. [[CrossRef](#)]
55. Cordill, M.J.; Moody, N.R.; Gerberich, W.W. The role of dislocation walls for nanoindentation to shallow depths. *Int. J. Plast.* **2009**, *25*, 281–301. [[CrossRef](#)]
56. Corcoran, S.G.; Colton, R.J.; Lilleodden, E.T.; Gerberich, W.W. Anomalous plastic deformation at surfaces: Nanoindentation of gold single crystals. *Phys. Rev. B* **1997**, *55*, R16057–R16060. [[CrossRef](#)]
57. Song, J.; Curtin, W.A. Mechanisms of hydrogen-enhanced localized plasticity: An atomistic study using α -Fe as a model system. *Acta Mater.* **2014**, *68*, 61–69. [[CrossRef](#)]
58. Hull, D.; Bacon, D.J. *Introduction to Dislocations*, 5th ed.; Elsevier: Amsterdam, The Netherlands, 2011.
59. Rice, J.R.; Beltz, G.E. The activation energy for dislocation nucleation at a crack. *J. Mech. Phys. Solids* **1994**, *42*, 333–360. [[CrossRef](#)]
60. Kirchheim, R. On the solute-defect interaction in the framework of a defactant concept. *Int. J. Mater. Res.* **2009**, *100*, 483–487. [[CrossRef](#)]

61. Lasia, A.; Grégoire, D. General Model of Electrochemical Hydrogen Absorption into Metals. *J. Electrochem. Soc.* **2019**, *142*, 3393–3399. [[CrossRef](#)]
62. Hachet, G.; Oudriss, A.; Barnoush, A.; Hajilou, T.; Wang, D.; Metsue, A.; Feaugas, X. Antagonist softening and hardening effects of hydrogen investigated using nanoindentation on cyclically pre-strained nickel single crystal. *Mater. Sci. Eng. A* **2021**, *803*, 140480. [[CrossRef](#)]
63. Kim, Y.; Kim, Y.; Kim, D.; Kim, S.; Nam, W.; Choe, H. Effects of Hydrogen Diffusion on the Mechanical Properties of Austenite 316L Steel at Ambient Temperature. *Mater. Trans.* **2011**, *52*, 507–513. [[CrossRef](#)]
64. Bak, S.; Abro, M.; Lee, D. Effect of Hydrogen and Strain-Induced Martensite on Mechanical Properties of AISI 304 Stainless Steel. *Metals* **2016**, *6*, 169. [[CrossRef](#)]
65. Robertson, I.M. The effect of hydrogen on dislocation dynamics. *Eng. Fract. Mech.* **2001**, *68*, 671–692. [[CrossRef](#)]
66. Robertson, I.M.; Birnbaum, H.K.; Sofronis, P. Hydrogen Effects on Plasticity. In *Dislocations in Solids*, 1st ed.; Hirth, J.P., Kubin, L., Eds.; Elsevier: Amsterdam, The Netherlands, 2010; Volume 15, pp. 249–293.
67. Ogawa, Y.; Hosoi, H.; Tsuzaki, K.; Redarce, T.; Takakuwa, O.; Matsunaga, H. Hydrogen, as an alloying element, enables a greater strength-ductility balance in an Fe-Cr-Ni-based, stable austenitic stainless steel. *Acta Mater.* **2020**, *199*, 181–192. [[CrossRef](#)]
68. Wang, S.; Hashimoto, N.; Wang, Y.M.; Ohnuki, S. Activation volume and density of mobile dislocations in hydrogen-charged iron. *Acta Mater.* **2013**, *61*, 4734–4742. [[CrossRef](#)]
69. Wang, D.; Lu, X.; Deng, Y.; Wan, D.; Li, Z.; Barnoush, A. Effect of hydrogen-induced surface steps on the nanomechanical behavior of a CoCrFeMnNi high-entropy alloy revealed by in-situ electrochemical nanoindentation. *Intermetallics* **2019**, *114*, 106605. [[CrossRef](#)]
70. Wang, D.; Lu, X.; Wan, D.; Li, Z.; Barnoush, A. In-situ observation of martensitic transformation in an interstitial metastable high-entropy alloy during cathodic hydrogen charging. *Scr. Mater.* **2019**, *173*, 56–60. [[CrossRef](#)]
71. Zielinski, A.; Lunarska, E.; Smialowski, M. The interaction of hydrogen atoms and dislocations in irons of different purity. *Acta Metall.* **1977**, *25*, 551–556. [[CrossRef](#)]

PAPER III

Chemically induced phase transformation in austenite by focused ion beam

Chemically Induced Phase Transformation in Austenite by Focused Ion Beam

ADINA BASA, CHRISTIAN THAULOW, and AFROOZ BARNOUSH

A highly stable austenite phase in a super duplex stainless steel was subjected to a combination of different gallium ion doses at different acceleration voltages. It was shown that contrary to what is expected, an austenite to ferrite phase transformation occurred within the focused ion beam (FIB) milled regions. Chemical analysis of the FIB milled region proved that the gallium implantation preceded the FIB milling. High resolution electron backscatter diffraction analysis also showed that the phase transformation was not followed by the typical shear and plastic deformation expected from the martensitic transformation. On the basis of these observations, it was concluded that the change in the chemical composition of the austenite and the local increase in gallium, which is a ferrite stabilizer, results in the local selective transformation of austenite to ferrite.

DOI: 10.1007/s11661-013-2101-4

© The Minerals, Metals & Materials Society and ASM International 2013

I. INTRODUCTION

THE faced-centered cubic (FCC) to body-centered cubic (BCC) phase transformation in steel is an important process which can be both dis- or advantageous. For example, in the case of transformation-induced plasticity (TRIP) or TRIP-assisted steels, this phase transformation is used to provide extra strain hardening, as well as deformation capability, to the steels.^[1–3] Conversely, in the case of austenitic stainless steels (ASSs), the martensitic phase transformation can drastically influence the corrosion and mechanical properties.^[4–6] Abreu *et al.*^[4] have shown that the increase in volume fraction of martensite formed during plastic deformation of ASSs reduces both pitting corrosion and generalized corrosion resistance. Baudry and Pineau^[5] reported that the formation of martensite in an Fe-18.25 Cr-6.50 Ni-0.19 C (wt pct) alloy caused earlier initiation and propagation of fatigue cracks.

The typical martensitic phase transformation for most commercially available ASSs is below room temperature; even if it is thermodynamically possible, the driving force for the phase transformation is too high, which makes the phase transformation only important in the case of the cryogenic applications.^[7–9] There are a few empirical relations available in the literature providing the martensitic transformation temperature (M_s) as a function of the composition of the steel.^[7,10–13] However, because the martensitic transformation is a non-

diffusional phase transformation accompanied by shear, it can occur if the shear is provided mechanically by external forces. Therefore, cold working of ASSs may trigger the martensite formation well above the M_s . The degree to which this procedure can be accomplished varies with the chemical composition of the steel, and there are empirical equations available for predicting the amount of the phase transformation at a given strain.^[14]

It is also found that implantation of a wide range of ions triggers the martensitic transformation in the austenite, and it was shown that the main contributing factor is the strain induced by the implantation, which is responsible for the phase transformation.^[15–19] Though, a change in the chemical composition of the alloy can play a role as well; for example, it is shown that by implantation of strong austenite-stabilizing ions, such as nickel and nitrogen, it is possible to transform the martensite into austenite.^[20] Recently, by the introduction of focused ion beam (FIB), the implantation of gallium ions and their effects on the sample become a concern. It is highly important to elucidate these side effects because of application of FIB for characterization, examination, and sample preparation in materials science; for example, micro-compression testing of pillars,^[21–24] 3D tomography of microstructure,^[25,26] studying the crack interaction with the grain boundary,^[27,28] preparation of TEM, and atom probe microscope samples.^[29,30] Knipling *et al.*^[31] studied the effect of FIB on the stability of the austenite phase and its transformation to the BCC structure in three commercial stainless steels with different austenite stability. These researchers determined that the alloy composition, *i.e.* austenite stability, is the most crucial parameter for observation of phase transformation.

The austenite stability and its phase transformation in the cases of the duplex stainless steels (DSSs) and super DSSs (SDSSs) are not well studied. A direct comparison between the austenite phase in DSSs and SDSSs and the austenitic steels can be performed cautiously by

ADINA BASA, Ph.D. Student, and CHRISTIAN THAULOW, Professor, are with the Department of Engineering Design and Materials, Norwegian University of Science and Technology, 7491 Trondheim, Norway. AFROOZ BARNOUSH, Postdoctoral Fellow, is with the Department of Engineering Design and Materials, Norwegian University of Science and Technology, and also with the Department of Materials Science, Saarland University, 66041 Saarbrücken, Germany. Contact e-mail: afrooz.barnoush@ntnu.no

Manuscript submitted March 11, 2013.

Article published online November 8, 2013

considering the following factors: first, the chemical composition of the austenite phases in DSSs and SDSSs are different from typical ASSs; second, the austenite phase in DSSs and SDSSs is constrained by the ferrite phase, and the whole microstructure is under alternating compressive stress in ferrite and tensile stress in austenite as a result of quenching from high temperature for stabilization of the 50/50 austenite/ferrite composition in these alloys.^[32] Lo and Lai^[9] used TEM, magnetic susceptibility and electrical resistivity, magnetic hysteresis loops, and X-ray diffractometry to study the stability of the austenite in a highly alloyed DSS. These researchers' results show that the austenite phase in this alloy is highly stable against cooling to 4 K (−269 °C), as well as cold deformation up to 50 pct.

In this paper, the stability of the austenite phase in a SDSS under the influence of FIB and gallium ion implantation is examined. For these experiments, a combination of high resolution electron backscatter diffraction (EBSD), energy dispersive X-ray spectroscopy (EDS) investigations of the Ga-damaged microstructure, and Monte Carlo simulations using the SRIM code were used.

II. EXPERIMENTAL PROCEDURE

A. Materials

An EN1.4501 (UNS S32760) SDSS with the nominal composition given in Table I was used in this study. The sample was solution annealed, the process consisting of holding the material at 1403 K (1130 °C) for 7 hours followed by water quenching to less than 285 K (12 °C). The heat treatment applied results in a mixture of austenite and ferrite phases of an approximately 50/50 ratio. Table II shows the partitioning coefficients of the major stabilizer elements for the austenite (nickel, copper) and ferrite (chromium, molybdenum) phases as they were determined by EDS.

Cylindrical samples with a diameter of 12 mm and a thickness of 4 mm were cut from forged bars having 177.8 mm in diameter. The metallographic preparation of the samples consisted of grinding with silicon-carbide papers up to 2400 grade, followed by mechanical polishing with water-based diamond suspension up to 1 μm, and electropolishing for 30 seconds with a methanol/H₂SO₄ electrolyte.^[33] Figure 1 presents the

scanning electron microscope (SEM) image of an electropolished sample, where the α ferrite grains are filling in the spaces between γ austenite grains.

B. Methods

1. FIB milling

The FEI Helios NanoLab DualBeam FIB microscope was used, which incorporates both an Elstar ultrahigh resolution SEM and a Sidewinder™ gallium ion column. The ion column can be used both for high resolution imaging and precise material removal/deposition from/on the surface of a sample. In the milling mode, the ion beam scans the surface of the defined pattern in a number of steps in a serpentine manner. Each step is characterized by a certain overlap of the beam diameter, and the ion beam will stay at each step for a specific time, which is a fraction of the total milling time.

Milling patterns with the dimension 5 × 5 μm² were defined on two austenite grains designated A(001) and A(111) for which the (001) and (111) plane normals were approximately parallel to the specimen surface normal. The sample was positioned at the SEM–FIB coincidence point and a combination of three gallium ion doses and four acceleration voltages was used for milling patterns on each grain. The dose was controlled by varying the pattern depths and the applied gallium current. Decreasing of the beam current resulted in an increase of the

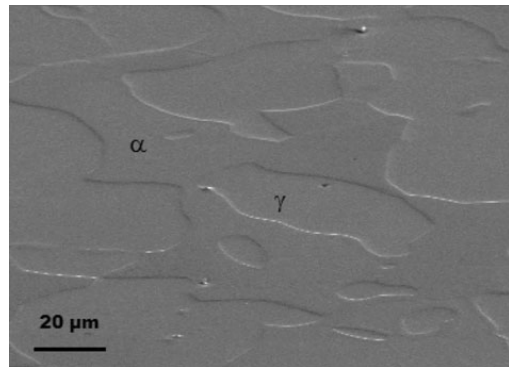


Fig. 1—SEM image of the dual phase microstructure of SDSS.

Table I. Chemical Composition of SDSS Investigated in This Study (Weight Percent)

	C	Si	Mn	S	P	Cr	Ni	W	Mo	Cu	N	Al
SDSS	0.017	0.23	0.51	0.001	0.027	24.92	7.31	0.53	3.6	0.60	0.253	0.005

Table II. Partitioning Coefficients of the Major Stabilizer Elements of the Austenite and Ferrite Phases

	Cr	Ni	Mo	Cu
Austenite (γ)	24.51 ± 0.18	8.85 ± 0.13	2.67 ± 0.17	0.76 ± 0.10
Ferrite (α)	28.30 ± 0.18	5.54 ± 0.03	4.03 ± 0.16	0.46 ± 0.04
Partitioning coefficient (K _{γ/α})	0.86	1.59	0.63	1.66

Table III. Parameters Used for FIB Milling

Ga Doses (nC/ μm^2)	Voltage (kV)	Ga Current (nA)	Time (s)	Height (μm)	Name
1.25	30	6.5	5	0.2	A1_D1
	16	4.7	7	0.196	A2_D1
	8	1.5	21	0.191	A3_D1
	5	1.3	26	0.189	A4_D1
1.13	30	2.7	11	0.18	A1_D2
	16	1.4	21	0.174	A2_D2
	8	0.66	46	0.182	A3_D2
	5	0.43	68	0.168	A4_D2
0.988	30	0.44	65	0.17	A1_D3
	16	0.24	112	0.1577	A2_D3
	8	0.21	131	0.1685	A3_D3
	5	0.13	197	0.1518	A4_D3

total milling time and decrease of the height. A complete overview of the parameters used is given in Table III.

During milling, the volume per dose, the dwell time (how long the ion beam spends on a single pixel in one pass), the overlap (distance between steps) and the milled areas were kept constant at $0.15 \mu\text{m}^3/\text{nC}$, $1 \mu\text{s}$, 50 pct and $25 \mu\text{m}^2$, respectively.

2. SEM-EBSD mapping

A low-vacuum field emission SEM (LV-FESEM), Zeiss Ultra 55 VP, was used for EBSD analysis prior to and after milling out the square patterns in the sample. The EBSD patterns were acquired offline using a NORDIF UF750 high speed camera system on a hard disk, and TSL OIM software was used for indexing and data analysis. The sample was tilted 70 deg for EBSD mapping, the acceleration voltage was 30 kV and the working distance was 21 mm. Two different step sizes were used for EBSD mapping: 200 nm step size for overall analysis of large regions, and 20 nm step size for high resolution analysis of $2 \times 4 \mu\text{m}^2$ patterns, including milled and non-milled areas within the examined austenite grains.

The EBSD patterns resulting from the interaction of the electron beam with the samples are indexed by selecting ferrite and austenite as possible phases. The resulting information is represented in the form of different types of maps: the inverse pole figure (IPF) map also known as the orientation map, which represents the normal orientation in each scanned point; the material phase map which gives phase information about the present phase in each measurement point; the image quality (IQ) map and the confidence index (CI) map which give the quality of the diffraction pattern and the confidence in indexing the pattern taken at each scanned point, respectively. In addition to these standard methods, it was also used orientation gradient mapping (OGM) analysis. The OGM technique is used to analyze the lattice misorientation calculated with respect to its neighbor points.^[34] This approach means that for each point measured, the next neighbor point will be determined. The relation between two orientations is given by the rotation axis and the rotation angle necessary to rotate the first orientation until it becomes the same as the second one. The orientation gradient in one direction is given by the value of the rotation angle.

The OGM procedure determines the gradients in both the x - and y -directions (θ_x and θ_y), and the present study will analyze the average (θ_x , θ_y) orientation gradient map.

3. EDS investigations

The EDS analysis of the areas milled with FIB was performed on a variable pressure SEM (VP-SEM), Hitachi S-3400N, and the offline software Oxford Instruments AZtec was used for quantification of the results. Two modes were used, a multipoint scan taken from inside of each milled area, and a map scan of the FIB milled areas with gallium ion doses D2 and D3 in the A(111) austenite grain. An acceleration voltage of 25 kV was used.

III. RESULTS

A. EBSD Analysis of Gallium Ions Implanted Areas

Phase transformation in the austenite grains milled with FIB was investigated by means of EBSD. Figures 2 and 3 present the SEM images, the phase identification and the IPF maps of the milled areas made in the A(001) and A(111), respectively, austenite grains.

At a high acceleration voltage of 30 kV, the beam size is reduced and milling is precisely performed, as can be observed from the sharp edges of the milled boxes in Figures 2(a) and 3(a). The higher kinetic energy of the ions resulted in higher damage to the surface, as well as surface roughening. Conversely, lower acceleration voltages result in increasing ion beam diameters, which causes contamination around the milled areas, as well as lower milling precision.

Independent of the acceleration voltage or the gallium doses, the austenite phase is transformed into a ferritic phase for both orientations, clearly shown in the phase maps of the Figures 2(b) and 3(b). The FCC to BCC phase transformation seen in Figures 2(c) and 3(c) is in accordance with the Nishiyama–Wasserman (N–W) or Kurdjumov–Sachs (K–S) orientation relationships.^[35,36] This transformation was also observed by Knipling in their investigations.^[31]

In addition to the EBSD measurements shown in Figures 2 and 3, high resolution EBSD measurements have been conducted on all the FIB milled areas to

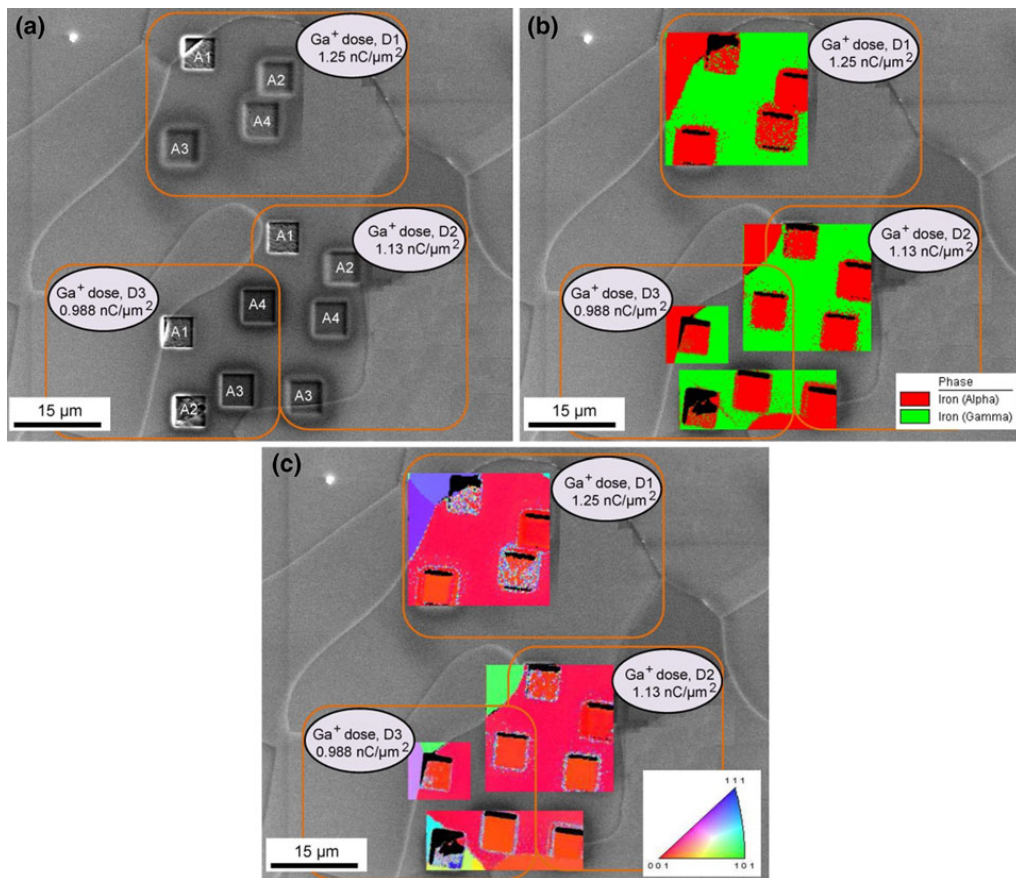


Fig. 2—FIB milled areas in the A(001) austenite grain (a) SEM image of all the patterns milled with different parameters; (b) phase map where green is austenite and red is ferrite, (c) IPF map showing the change in the crystallographic orientation of the grains after milling.

confirm the above observations. Tables IV and V present a selection from all the high resolution EBSD measurements, which are representatives for this study of both austenite orientations. The first row of the tables gives the name of the milled area according to the parameters used in FIB and presented in Table III. The second row presents the SEM image with an indication of the location of the EBSD map, where half of the pattern was capturing the FIB milled area and half was on the un-milled region. The following two rows present the phase, IPF, IQ, CI, and OGM maps.

The information summarized in Table IV shows that for the A(001) grain, the austenite to ferrite phase transformation is preceded by milling with FIB in all conditions. The IPF maps clearly show the N–W and K–S relation between the original phase and the transformed phase. Both CI and IQ maps assure that the measurements are reliable and acceptable. Additionally, the IQ maps show that the transformation is not accompanied with high local strains. Obviously,

surface damage at high acceleration voltages resulted in surface roughening, which most likely blocked the diffraction pattern or reduced its quality. The orientation gradients close to zero in the OGM maps also clearly indicate that the phase transformation is not accompanied with any local plastic deformation or local excess of dislocations with the same sign.^[37]

However, the FIB milling of the A(111) grain, as shown in Table V, is somewhat different from the A(001) one. At low acceleration voltage, the phase transformation is not complete, and the FIB milled region is partly transformed to ferrite. At high acceleration voltage, A1_D1, the damage to the surface is sufficiently high that no diffraction pattern was formed on the milled area. Though at moderate acceleration voltage, *i.e.*, A3_D3, the phase transformation with K–S and N–W crystallographic relations occurs without any formation of excess dislocations with the same sign (see OGM map) or relatively high residual strains (see IQ map), as in the case of the A(001) grain.

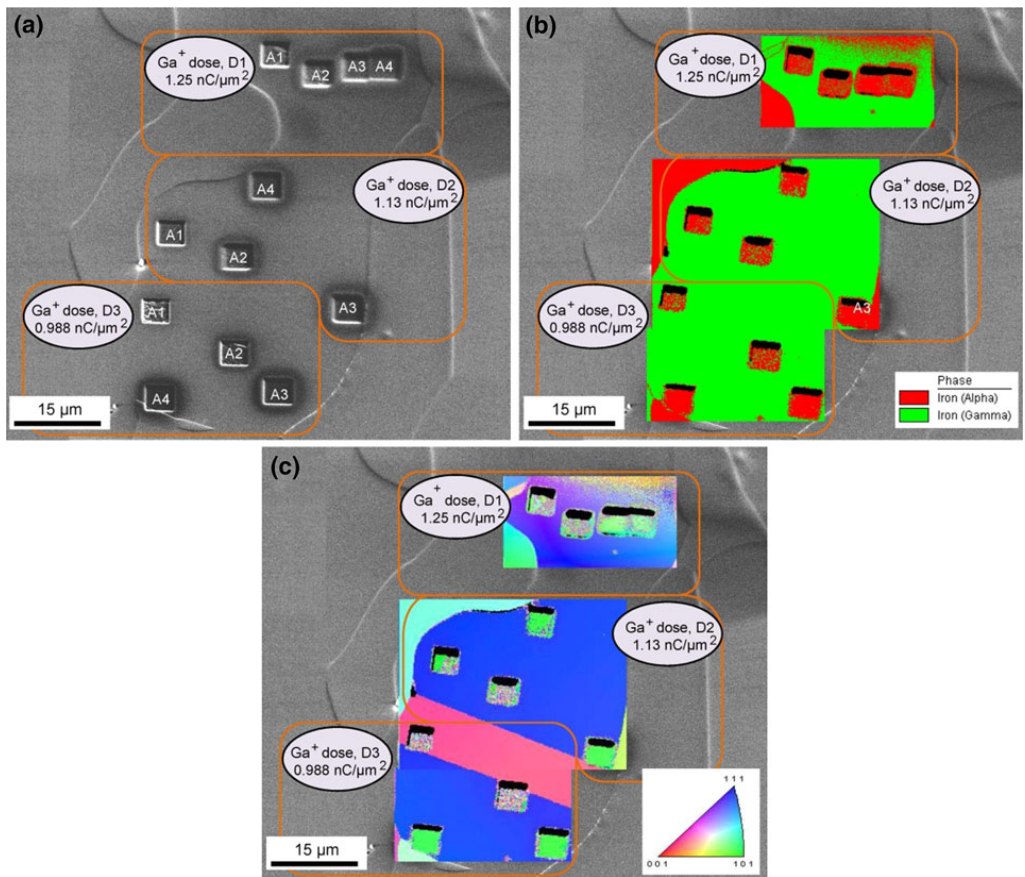


Fig. 3—FIB milled areas in the A(111) austenite grain (a) SEM image of all the patterns milled with different parameters; (b) phase map where green is austenite and red is ferrite, (c) IPF map showing the change in the crystallographic orientation of the grains after milling.

B. EDS Results

The gallium map taken by EDS analysis, shown in Figure 4, presents the ion beam voltage effect on the implanted gallium concentration for an A(111) austenite grain. Clearly, by reducing the acceleration voltage, the implanted gallium concentration is reduced.

A multipoint scan EDS analysis has been performed on all areas milled with FIB, and the results are shown in Figure 5. The variation of the implanted gallium concentration at different doses is within the resolution limit of the EDS; therefore, the multipoint scans were plotted as average values. The concentration of implanted gallium is only dependent on the acceleration voltage and the orientation of the grains. Even at low acceleration voltages, gallium was implanted into the sample, and it was possible to detect it with EDS; the increase in acceleration voltage used in FIB milling will result in an increase in gallium concentration in the sample. As for the crystallographic orientation effect, gallium will penetrate more easily into the open packed planes, and a higher amount of gallium will therefore be

found in the A(001) grain compared with the closely packed A(111) grain.

One of the main short comings of the EDS method is the large volume probed by this method. During EDS, the interaction of the electron with the sample will result in an electron excited volume of a hemispherical shape under the surface of the sample. The depth of the electron penetration and the volume of interaction depend on such parameters as the angle of incidence of the electron beam with the sample, the current and the acceleration voltage of the electron beam, as well as the average atomic number and the density of the sample. For the acceleration voltage of 25 kV used in this study and the typical density of 7.8 g/cm³ for SDSS, the depth of electron penetration during X-ray investigation (x) and the width of the excited volume (y) can be estimated according to the empirical formulas given by Potts,^[38] as given in Table VI. Additionally, Kanaya and Okayama^[39] have given a theoretical expression for the distance (r) that an electron will travel after it enters into the sample and reaches its final resting site.

Table IV. Selection of High Resolution EBSD Maps Made for Areas Milled in the A(001) Austenite Grain

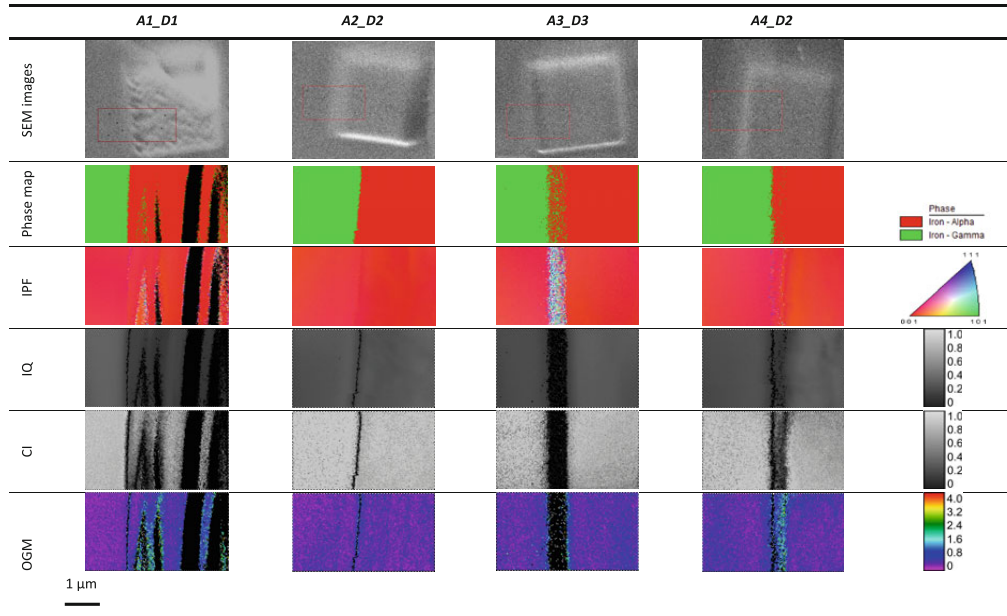
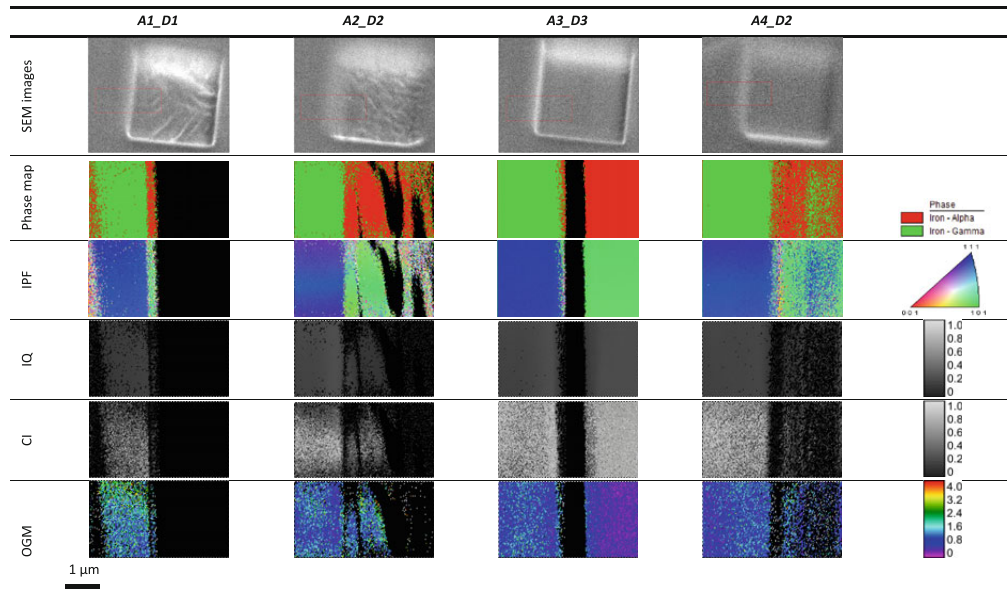


Table V. Selection of High Resolution EBSD Maps Made for Areas Milled in A(111) Austenite Grain



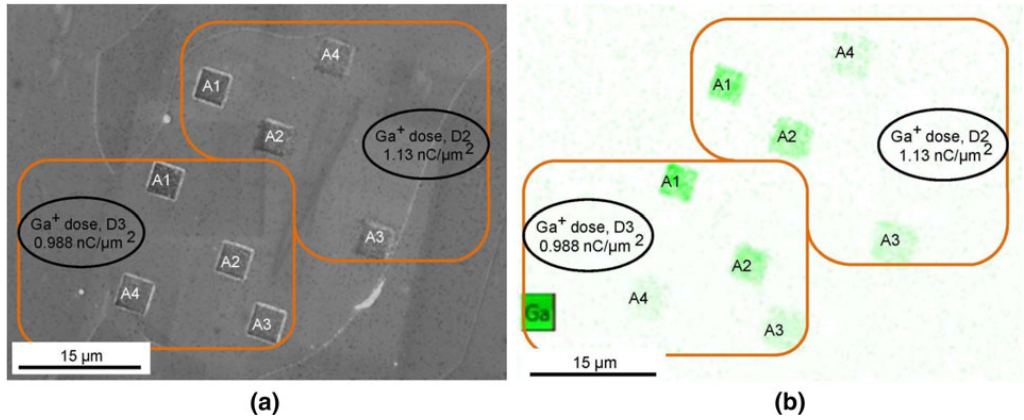


Fig. 4—EDS map analysis of an A(111) grain: (a) SEM image with the position of the areas milled with gallium, (b) EDS map of gallium.

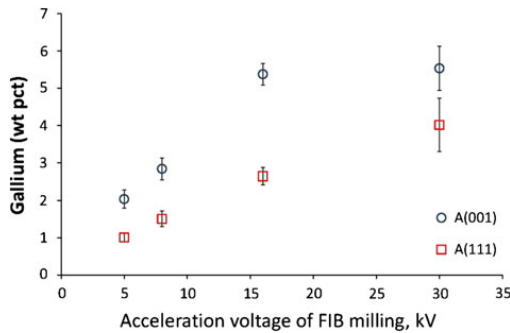


Fig. 5—Multipoint EDS scan.

Generally, the electron penetration depth ranges in between 1 and 5 μm , and the values presented in Table VI are within these limits.

The penetration depth of the large gallium ions is expected to be much less than the electrons at similar acceleration voltages. To elucidate the range of penetration of the gallium ions, it was performed a Monte Carlo simulation using the SRIM code.^[40] For the simulations, the composition of the target material was set in at pct to 25 chromium, 9 nickel, and 3 molybdenum, with the rest being iron.

The simulations were performed with 30, 16, 8, and 5 kV acceleration voltages, which resulted in the ion implantation profiles given in Figure 6. The maximum amount of gallium was found to be at a distance of 10 nm under the surface when an acceleration voltage of 30 kV was used for the gallium implantation simulations, and the last traces of gallium should be found at a maximum distance of 25 nm. The penetration depth decreases with the decrease of acceleration voltage, so gallium will penetrate a depth of less than 10 nm when 5 kV is used.

Comparison of the gallium implantation depth from SRIM simulation with the volume probed with the EDS

Table VI. The Estimated Electron Penetration Parameters During X-ray Investigations

	25 kV
$x = 0.1E_0^{1.5}/\rho$ (μm)	1.6
$y = 0.077E_0^{1.5}/\rho$ (μm)	1.2
$r = 0.0276AE_0^{1.67}/(\rho Z^{.89})$ (μm)	2.4

E_0 represents the acceleration voltage, ρ the density of the material, A is the atomic mass and Z is the atomic number of the material.

technique shows that there is a large underestimation in the gallium concentration measurement on the surface, as given in Figure 5.

IV. DISCUSSION

Transformation of metastable austenitic steels under the influence of FIB has already been reported by Knipling *et al.*^[31] They examined the stability of three different stainless steels, a maraging sandvik 1RK91 (MSS), AISI 304 (ASS), and an super austenitic AL-6XN (sASS). These authors concluded that the main factor influencing the FCC to BCC phase transformation was the austenite stability in the steels.

The most important criterion for the stability of the austenite is the M_s . According to Warnes and King,^[8] the stability of austenite to not transform to martensite is given by a negative M_s . In the case of SDSS, there is no established empirical equation to estimate the stability of the austenite phase. Lo and Lai^[9] have studied the applicability of the available equations in literature that describe the M_s ^[7,8,10–13,41–44] to a DSS and concluded that only the equations given by Pickering,^[10] Monkman,^[11] Eichelman–Hull^[12], and Larbalestier–King^[7] are valid for a duplex steel. The austenite phase in the DSS they examined was stable down to 4 K (-269 °C).

The composition of the austenitic phase of the SDSS studied in this paper and of the materials studied by Lo

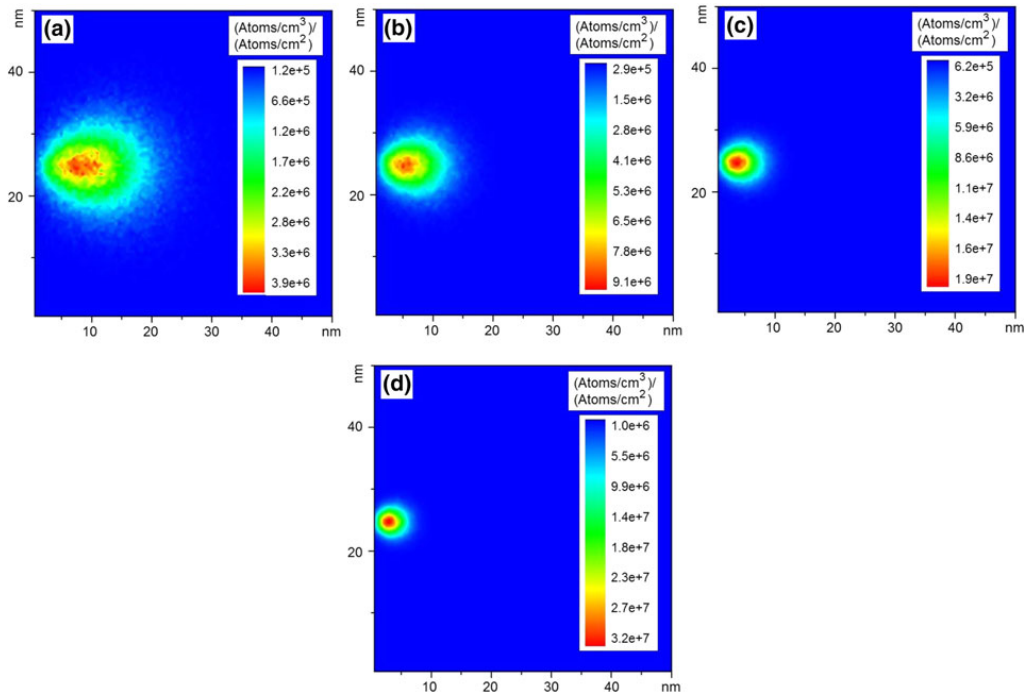


Fig. 6—SRIM simulations of the penetration depth of gallium ions into the surface at (a) 30 kV, (b) 16 kV, (c) 8 kV, and (d) 5 kV.

Table VII. The Composition of the Austenitic Phases of the Materials Compared in this Paper (Weight Percent)

	C	Si	Mn	S	P	Cr	Ni	W	Mo	Cu	N	Al
SDSS_present study	0.017	0.21	—	—	—	24.52	8.86	0.261	2.67	0.76	0.25	—
DSS_Lo ^[9]	0.03	0.25	0.23	—	—	24.95	6.13	—	1.16	—	0.31	—
DSS_Tavares ^[45]	0.02	—	—	—	—	21.83	5.85	—	2.18	—	0.16	—
MSS_Knipling ^[31]	0.01	0.15	0.30	—	—	12.00	9.00	—	4.00	2.00	—	0.30
ASS_Knipling ^[31]	0.08	1.00	2.00	0.03	0.04	19.00	9.50	—	—	—	—	—
sASS_Knipling ^[31]	0.02	0.40	0.40	0.001	0.02	20.50	24.00	—	6.20	0.20	0.22	—

and Lai,^[9] Tavares^[45] and Knipling^[31] are given in Table VII. The estimated M_s for the steel compositions given in Table VII, according to the different equations, are shown in Figure 7. Indeed, the Pickering, Monkman, Eichelman–Hull, and Larbalestier–King’s equations predict that the austenite phase in the SDSS studied in this paper is as stable as Lo’s DSS and Knipling’s sASS. The relatively high M_s estimated for the austenite phase of Tavares’ DSS is in good agreement with their findings that the austenite phase in that particular DSS is not stable and transforms to martensite during cold rolling.

While Dai’s M_s estimated for Lo’s DSS predicts that the austenite FCC phase in this alloy transforms to BCC phase at a temperature lower than 100 K (−173 °C), Lo’s experiments showed that the austenite is stable down to 4 K (−269 °C). This finding suggests that Dai’s equation is most likely overestimating the M_s in the case of DSS.

From the M_s values estimated for the SDSS material investigated in this paper (Figure 7), notably high austenite stability is expected. This finding raises the question of how phase transformation is triggered with the FIB.

Naraghi *et al.*^[46] showed that the EBSD technique is a reliable way to detect both spontaneous and deformation induced martensite in austenitic stainless. Indeed the very high angular resolution of the EBSD technique for detecting any lattice rotation makes this technique perfect for detecting martensitic deformation.^[47–50] Considering the EBSD results, it can be concluded that the phase transformation is not followed by the typical shearing process known from austenite to martensite transformations. The IQ and OGM maps do not indicate any plastic deformation precedes the phase transformation. Conversely, the EDS analysis in combination with the simulations of gallium ion

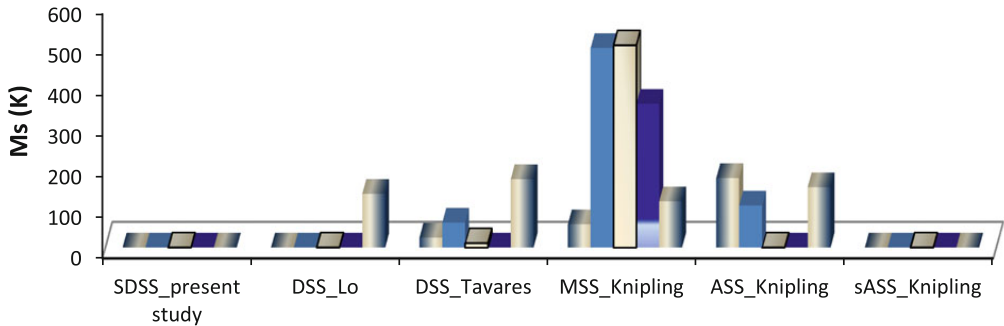
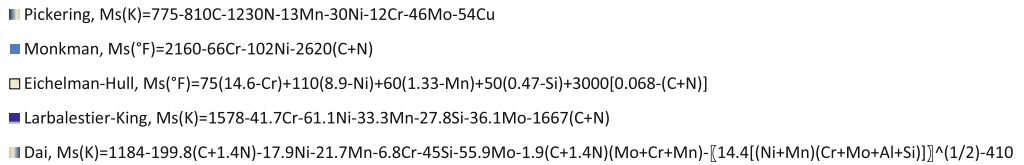


Fig. 7—Martensitic transformation temperatures as given by Pickering, Monkman, Eichelman–Hull, Larbalestier–King, and Dai’s equations for the investigated materials.

implantation confirmed relatively high implanted gallium ion concentrations on the surface of the milled areas.

Kolman *et al.*^[51] showed that gallium is a ferrite stabilizer and small addition of this element to ASSS promotes the austenite to ferrite phase transformation. This result is exactly what is observed in the SDSS investigated in the present paper. FIB-induced gallium ion implantation locally changes the chemical composition on the surface of the austenite and triggers the austenite to ferrite phase transformation. Hence, this phenomenon was called chemically induced phase transformation.

The observed differences in the FIB-induced phase transformation on the different crystallographic orientations examined in this study can also be explained by the two different phenomena, which may occur when an ion comes into contact with a solid surface, *i.e.*, channeling and sputtering. In the case of the (001) oriented grains, the chance of the ions’ channeling deep into the crystal is higher, and this means less sputtering and more ions implantation. This effect is clearly seen in Figure 5, where gallium ion concentration on the surface of the (001) oriented grain for all FIB milling conditions is higher. Conversely, EBSD analysis shows that the FIB damage on the densely packed (111) oriented grain (Table V) is larger than on the (001) oriented grain (Table IV).

V. CONCLUSIONS

It is shown that through the implantation of ferrite stabilizing gallium that it is possible to trigger the FCC to BCC phase transformation in a highly stable austenite phase in a SDSS. High resolution EBSD analysis

proved that the phase transformation is not followed by plastic deformation and an increase in the dislocation density, as has been established for the metastable austenite to martensite phase transformation, but it is an austenite to ferrite transformation triggered by local change in the composition of the steel. EDS and Monte Carlo simulations using the SRIM code were performed to reveal qualitatively the local increase in the gallium concentration after FIB milling. It is shown that an adequate increase in the gallium concentration for the phase transformation is expected, even after FIB milling with relatively low acceleration voltage and doses. In addition, it is shown that the implanted gallium concentration is dependent on the crystal orientation. In densely packed orientations, where more sputtering than channeling of the ions is anticipated for the given acceleration voltage and ion doses, less ion implantation, and more mechanical damage was observed.

ACKNOWLEDGMENTS

The authors would like to acknowledge the Research Council of Norway for providing financial support through the PETROMAKS program. Special thanks are due to SINTEF Materials and Chemistry Department in Trondheim, Norway for providing the SDSS material studied in this paper. The first author would also like to thank Dr. Nousha Kheradmand for fruitful discussion regarding the OGM method.

NOMENCLATURE

A(001) Austenitic grain having the (001) plane normal oriented parallel to the normal of the sample’s surface

A(111)	Austenitic grain having the (111) plane normal oriented parallel to the normal of the sample's surface
ASS	Austenitic stainless steel
BCC	Body-centered cubic
CI	Confidence index
DSS	Duplex stainless steel
EBSD	Electron backscatter diffraction
EDS	Energy dispersive X-ray spectroscopy
FCC	Faced-centered cubic
FIB	Focused ion beam
IPF	Inverse pole figure
IQ	Image quality
K-S	Kurdjumov-Sachs relation
MSS	Maraging sandvik steel
M_s	Martensitic transformation temperature
N-W	Nishiyama-Wasserman relation
OGM	Orientation gradient mapping
sASS	Super austenitic stainless steel
SEM	Scanning electron microscopy
SDSS	Super duplex stainless steel
SRIM	Stopping and range of ions in matter
TEM	Transmission electron microscopy
TRIP	Transformation-induced plasticity
α	Ferrite
γ	Austenite

REFERENCES

- G.B. Olson and M. Azrin: *Metall. Trans. A*, 1978, vol. 9A, pp. 713-21.
- O. Grässel, L. Krüger, G. Frommeyer, and L.W. Meyer: *Int. J. Plast.*, 2000, vol. 16, pp. 1391-409.
- S.D. Antolovich and B. Singh: *Metall. Trans. B*, 1971, vol. 2B, pp. 2135-41.
- H.F.G. Abreu, S.S. Carvalho, P. Lima Neto, R.P. Santos, V.N. Freire, P.M. Oliveira Silva, and S.S.M. Tavares: *Mater. Res.*, 2007, vol. 10, pp. 359-66.
- G. Baudry and A. Pineau: *Mater. Sci. Eng.*, 1977, vol. 28, pp. 229-42.
- K. Sato, M. Ichinose, Y. Hirotsu, and Y. Inoue: *ISIJ Int.*, 1989, vol. 29, pp. 868-77.
- D.C. Larbalestier and H.W. King: *Cryogenics*, 1973, vol. 13, pp. 160-68.
- L.A.A. Warnes and H.W. King: *Cryogenics*, 1976, vol. 16, pp. 659-67.
- K.H. Lo and J.K.L. Lai: *J. Magn. Magn. Mater.*, 2010, vol. 322, pp. 2335-39.
- H.W. Pickering: *Physical Metallurgy and the Design of Steels*, Applied Science, London, 1978, p. 228.
- F.C. Monkman, F.B. Cuff, and N.J. Grant: *Met. Prog.*, 1957, vol. 71, p. 94.
- G.H. Eichelman and F.C. Hull: *Trans. Am. Soc. Met.*, 1953, vol. 45, p. 77.
- K.W. Andrews: *J. Iron Steel Inst.*, 1965, vol. 203, p. 721.
- K. Spencer, J.D. Embury, K.T. Conlon, M. Véron, and Y. Bréchet: *Mater. Sci. Eng. A*, 2004, vols. 387-389, pp. 873-81.
- N. Hayashi, I. Sakamoto, E. Johnson, L. Graabak, P. Børgesen, and B.M.U. Scherzer: *Hyperfine Interact.*, 1988, vol. 42, pp. 989-92.
- N. Hayashi, I. Sakamoto, and T. Takahashi: *J. Nucl. Mater.*, 1984, vols. 128-129, pp. 756-59.
- N. Hayashi and T. Takahashi: *Appl. Phys. Lett.*, 1982, vol. 41, pp. 1100-01.
- E. Johnson, A. Johansen, L. Sarholt-Kristensen, L. Graabk, N. Hayashi, and I. Sakamoto: *Nucl. Instrum. Method B*, 1987, vol. 1920, pp. 171-76.
- E. Johnson, A. Johansen, L. Sarholt-Kristensen, H. Roy-Poulsen, and A. Christiansen: *Nucl. Instrum. Method B*, 1985, vols. 7-8, pp. 212-18.
- R.G. Vardiman and I.L. Singer: *Mater. Lett.*, 1983, vol. 2, pp. 150-54.
- A. Barnoush, J. Dake, N. Kheradmand, and H. Vehoff: *Intermetallics*, 2010, vol. 18, pp. 1385-89.
- N. Kheradmand, A. Barnoush, and H. Vehoff: *J. Phys. Conf. Ser.*, 2010, vol. 240, pp. 3216-30.
- C.A. Volkert and A.M. Minor: *MRS Bull.*, 2007, vol. 32, pp. 389-99.
- M.D. Uchic and D.M. Dimiduk: *Mater. Sci. Eng. A*, 2005, vols. 400-401, pp. 268-78.
- D. Raabe, S. Zaefferer, P. Konijnenberg, E. Demir, A. Khorashadizadeh, and N. Zaafarani: *E-MRS Spring Meeting*, Strasbourg, France, 2010.
- S. Zaefferer, S.I. Wright, and D. Raabe: *Metall. Mater. Trans. A*, 2008, vol. 39A, pp. 374-89.
- C. Holzappel, W. Schäf, M. Marx, H. Vehoff, and F. Mücklich: *Scripta Mater.*, 2007, vol. 56, pp. 697-700.
- W. Schaefer, M. Marx, H. Vehoff, A. Heckl, and P. Randelzhofer: *Acta Mater.*, 2011, vol. 59, pp. 1849-61.
- S. Lozano-Perez: *Micron*, 2008, vol. 39, pp. 320-28.
- S. Kuwano, T. Fujita, D. Pan, K. Wang, and M. Chen: *Mater. Trans.*, 2008, vol. 49, pp. 2091-95.
- K.E. Knipling, D.J. Rowenhorst, R.W. Fonda, and G. Spanos: *Mater. Charact.*, 2010, vol. 61, pp. 1-6.
- A. Barnoush, M. Zamanzade, and H. Vehoff: *Scripta Mater.*, 2010, vol. 62, pp. 242-45.
- A. Barnoush and H. Vehoff: *Scripta Mater.*, 2006, vol. 55, pp. 195-98.
- M. Henning and H. Vehoff: *Acta Mater.*, 2005, vol. 53, pp. 1285-92.
- Z. Nishiyama: *Sci. Rep. Tohoku*, 1934, vol. 23, pp. 637-64.
- G.V. Kurdjumov and G. Sachs: *Z. Phys.*, 1930, vol. 64, pp. 325-43.
- N. Kheradmand and H. Vehoff: *Adv. Eng. Mater.*, 2012, vol. 14, pp. 153-61.
- P.J. Potts: *A Handbook of Silicate Rock Analysis*, Blackie, Glasgow, 1987, pp. 336-37.
- K. Kanaya and S. Okayama: *J. Phys. D*, 1972, vol. 5, pp. 43-58.
- J.F. Ziegler, M.D. Ziegler, and J.P. Biersack: *Nucl. Instrum. Methods B*, 2010, vol. 268, pp. 1818-23.
- C. Capdevila, F.G. Caballero, and C. Garcia de Andres: *ISIJ Int.*, 2002, vol. 42, pp. 894-902.
- Q.X. Dai, X.N. Cheng, Y.T. Zhao, X.M. Luo, and Z.Z. Yuan: *Mater. Charact.*, 2004, vol. 52, pp. 349-54.
- K. Ishida: *J. Alloys Compd.*, 1995, vol. 220, pp. 126-31.
- E.R. Jones, Jr, T. Datta, C. Almasan, D. Edwards, and H.M. Ledbetter: *Mater. Sci. Eng.*, 1987, vol. 91, pp. 181-88.
- S.S.M. Tavares, M.R. da Silva, J.M. Pardal, H.F.G. Abreu, and A.M. Gomes: *J. Mater. Process. Technol.*, 2006, vol. 180, pp. 318-22.
- R. Naraghi, P. Hedström, and A. Borgenstam: *Steel Res. Int.*, 2011, vol. 82, pp. 337-45.
- H. Sato and S. Zaefferer: *Acta Mater.*, 2009, vol. 57, pp. 1931-37.
- M. Calcagnotto, D. Ponge, E. Demir, and D. Raabe: *Mater. Sci. Eng. A*, 2010, vol. 527, pp. 2738-46.
- M. Karlsen, Ø. Grong, M. Søfferud, J. Hjelen, G. Rørvik, and R. Chiron: *Metall. Mater. Trans. A*, 2009, vol. 40A, pp. 310-20.
- M. Calcagnotto, D. Ponge, and D. Raabe: *Metall. Mater. Trans. A*, 2012, vol. 43A, pp. 37-46.
- D.G. Kolman, J.F. Bingert, and R.D. Field: *Metall. Mater. Trans. A*, 2004, vol. 35A, pp. 3445-54.

PAPER IV

***Nanomechanical testing of hydrogen effects on super duplex
stainless steel***

NANOMECHANICAL TESTING OF HYDROGEN EFFECTS ON SUPER DUPLEX STAINLESS STEEL

Adina BASA ¹⁾, Afrooz BARNOUSH ²⁾, Christian THAULOW ¹⁾

¹⁾NTNU, Department of Engineering Design and Materials, Trondheim, NORWAY,

²⁾Saarland University, Department of Material Science, Saarbruecken, GERMANY

adina.basa@ntnu.no , a.barnoush@matsci.uni-sb.de

ABSTRACT

The effect of hydrogen on the mechanical properties of the super duplex stainless steel is examined using in situ electrochemical nanoindentation (ECNI) tests. Within the ECNI, which is a nanoindenter combined with an electrochemical setup, the nanoindentation can be made on a surface that is immersed in an electrolyte and in situ electrochemically charged with hydrogen. In situ electrochemical nanoindentation testing captures the change in the onset of plasticity (pop-in load level) as well as the change in the hardness due to the absorption of the atomic hydrogen.

Keywords: Nanoindentation, hydrogen, super duplex stainless steel, pop-in

1. INTRODUCTION

Over the last years, the interaction of steels with hydrogen has led to many incidents, sometimes causing catastrophic failures. The main sources for hydrogen are the corrosion from the aqueous solutions, the cathodic protection and the contaminants in the melting and welding processes. Different mechanisms for hydrogen have been proposed, but the most established ones are Hydrogen Enhanced Decohesion (HEDE) and Hydrogen Enhanced Local Plasticity (HELP). The HEDE mechanism (the brittle fracture) suggests that the hydrogen accumulated within the atomic lattice reduces the cohesive bonding strength and it was first proposed by Troiano [1]. The HELP mechanism (the ductile fracture) proposes that the atomic hydrogen enhances the mobility of the dislocations causing a lowering in the shear strength and it was described for the first time by Birnbaum and Sofronis [2].

The Super Duplex Stainless Steel (SDSS) is a widely used material in offshore applications due to its high strength and toughness and excellent corrosion resistance [3] given by the two phases, austenite (γ) and ferrite (α). The non-magnetic ductile austenite has a Face-Centred Cubic (FCC) structure and it is acting like a crack stopper while the ferrite is more brittle due to its Body-Centred Cubic (BCC) structure. Despite these strong points, SDSS has often failed due to the hydrogen released during the cathodic protection leading to the hydrogen embrittlement. The main diffusion mechanism for hydrogen in

steel is the lattice diffusion by the interstitial jumps. The higher packing density of the austenite (0.74 as compared to 0.68 of the ferrite) [4] and its close packed lattice structure gives a higher solubility of the hydrogen atoms and a lower diffusion rate, while the ferrite is characterized by a higher diffusion rate and a lower solubility due to its open lattice structure. Although the concentration of hydrogen may be higher in the austenite, the ferrite is prone to the crack propagation at lower hydrogen concentration [5]. Even though many experimental studies [6, 7] and simulations [8, 9] of the hydrogen effect on SDSS have been done, a more complete understanding of the micro-mechanism is needed. A starting point for that is to provide a better characterization of the hydrogen effect on each individual phase and this can be done by the nanoindentation in combination with an electrochemical setup described below.

The nanoindentation is a widely used method [10,11] for studying the micromechanical properties of the materials. Recently, Barnoush et al. [12, 13] used the nanoindenter in combination with an electrochemical setup to investigate the effect of hydrogen on the micromechanical properties of different materials under hydrogen charging conditions. This is a promising method because the immediate effect of hydrogen on the local material microconstituents can be observed. Another advantage of using in-situ ECNI is related to the testing time, which is considerably lowered and limited to some hours while the nanoindentations are performed. Also, another big advantage is that the surface quality remains the same during testing, while in the case of ex-situ ECNI, either the surface is damaged [14] by the hydrogen during the long time charging or the hydrogen diffuses out of the material while the sample is transferred in between the electrochemical setup and the nanoindenter [15]. In-situ ECNI method is used in this paper and the authors would like to mention that the aim of this paper is primarily to describe the experimental procedure and to present only some preliminary results.

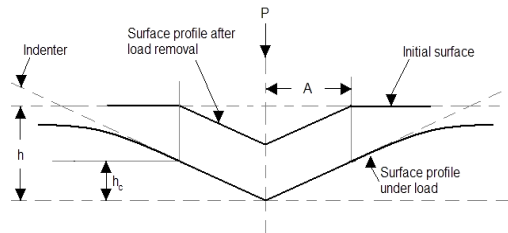


Fig. 1. The cross-sectional area of a nanoindentation

During a nanoindentation, an indenter tip is forced into the sample with a defined load. The maximum force is kept constant for a few seconds and then decreased, see Fig. 1. A load – displacement curve is produced, see **Fout! Verwijzingsbron niet gevonden.**, which is used to calculate the hardness and the reduced modulus of elasticity.

Three-sided pyramidal tips are standard for the nanoindentations [16]. The standard three-sided tip is the Berkovich tip, which has a total included angle from plane to edge of 142.3° and a half angle, θ , of 65.35° , see Fig. 3.

The hardness is calculated according to:

$$H = \frac{P_{\max}}{A_c} \quad (1)$$

where P_{\max} - the maximum applied load, A_c - the contact area, calculated from the tip area function, based on the contact depth, h_c .

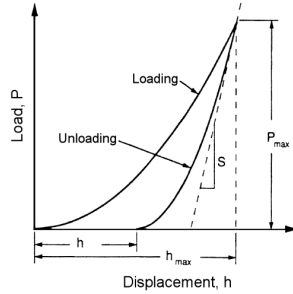


Fig. 2. Load – displacement curve produced during the nanoindentation

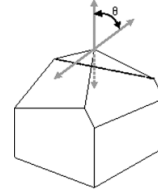


Fig. 3. Three-sided pyramidal Berkovich tip

For a perfect Berkovich indenter [10]:

$$A_c = 24.5h_c^2 \quad (2)$$

$$h_c = h_{max} - \varepsilon \frac{P_{max}}{S} \quad (3)$$

where h_{max} - the maximum displacement, ε - the geometric constant equal to 0.75, S - the stiffness of the material.

In reality, an indenter tip will never be perfect, so, each tip will be calibrated according to its own tip area function. The procedure involves performing a series of 25 up to 100 indents of different contact depths (varying the loading levels) on a fused quartz sample with a known reduced modulus of 69.6 GPa. The contact area will be determined by measuring the stiffness based on the following equation:

$$A_c = \frac{\pi}{4} \left(\frac{S}{E_r} \right)^2 \quad (4)$$

where: E_r - the reduced modulus of elasticity.

Then, the contact area will be plotted as a function of the contact depth and the points will be fitted to a sixth order polynomial:

$$A_c = C_0h_c^2 + C_1h_c + C_2h_c^{1/2} + C_3h_c^{1/4} + C_4h_c^{1/8} + C_5h_c^{1/16} \quad (5)$$

where: C_0 - equal to 24.5 for a Berkovich tip, C_1 to C_5 - the curve fitting parameters.

The reduced modulus of elasticity is calculated as:

$$E_r = \frac{\sqrt{\pi}}{2} \frac{S}{\sqrt{A_c}} \quad (6)$$

The relation between the reduced modulus and the elastic modulus is:

$$\frac{1}{E_r} = \frac{1 - \nu_s^2}{E_s} + \frac{1 - \nu_i^2}{E_i} \quad (7)$$

where: ν - the Poisson ratio for the sample, respectively, the indenter; E - the elastic modulus of the sample, respectively, the indenter.

For a standard diamond indenter tip $E_i = 1140 \text{ GPa}$ and $\nu_i = 0.07$.

2. EQUIPMENT AND SAMPLE PREPARATION

The experiments were performed with a Hysitron TriboScan TI-750 with Performech controller in combination with an electrochemical setup as shown in Fig. 4. A diamond Berkovich long tip, specially designed for testing inside the electrolyte was used. The used load function is presented in Fig. 5, where the last segment of 1 second holding time at 10% peak value was added for the drift correction.

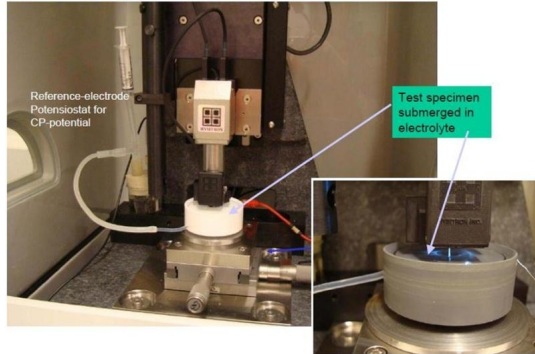


Fig. 4. The electrochemical setup

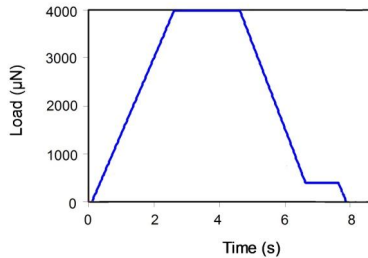


Fig. 5. Load function

As a counter electrode for the electrochemical setup, a platinum wire was used while a Saturated Calomel Electrode (SCE) was the reference electrode. The sample holder allows the sample to be covered with the electrolyte during testing.

A coarse grained SDSS with a chemical composition of 0.016% C, 0.46% Mn, 0.24% Si, 0.024% P, 0.001% S, 7.16% Ni, 25.22% Cr, 3.76% Mo, 0.276% N, 0.205% Cu and a Pitting Resistance Equivalent Number (PRE_N) equal to 42.044 has been investigated. The high pitting resistance is given by the high levels of chromium, molybdenum and nitrogen, as is calculated according to:

$$PRE_N = \%Cr + 3.3 \times \%Mo + 16 \times \%N \quad (8)$$

The macroscopic yield strength for this material is 560 MPa and the tensile strength is 790 MPa. These excellent properties are given by the dual phase microstructure of the austenite (γ) and ferrite (α), Fig. 6.

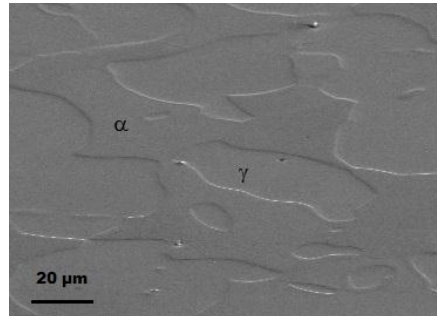


Fig. 6. SEM image of the coarse grained super duplex stainless steel

The starting point for the sample preparation was the grinding with silicon-carbide papers of grade 500, 1000 and 2400, followed by a mechanical polishing with a water based diamond suspension of 3 μm and 1 μm. The last step was the electropolishing in order to remove the work hardened microscopic layer of the material caused by the mechanical polishing. Table 1 presents the electrolyte and the used electropolishing parameters [14].

Table 1. Parameters used for the electropolishing

Electrolyte	Pot., V	Flow rate	Time, s	Temp., °C
Methanol/H ₂ SO ₄	15	8	15	21

The surface quality after the electropolishing is presented in Fig. 7. The Average Roughness (RA) is less than 10 nm, as given by the nanoindenter software.

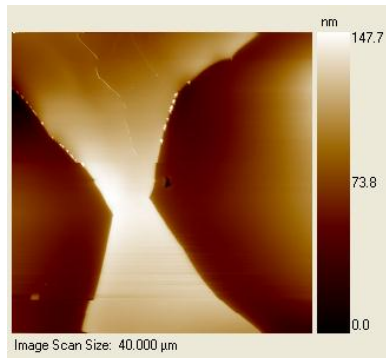


Fig. 7. Topography image, scanned with TI-750 prior testing, where the ferrite is light and the austenite is dark

3. EXPERIMENTAL RESULTS

Freshly electropolished samples were tested first in air and then in a 0.05 M Na₂SO₄ electrolyte. Hydrogen started to form when a cathodic potential of -1150 mV was applied.

Both the austenite and the ferrite phases were tested with a maximum load of 4000 μN and a loading rate of 2000 $\mu\text{N/s}$. Fig. 8 and Fig. 9 present the effect of hydrogen on the hardness and on the reduced modulus of elasticity, respectively.

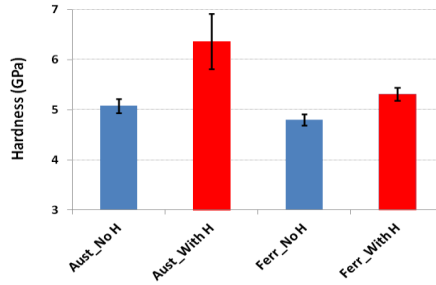


Fig. 8. The hydrogen effect on the sample hardness

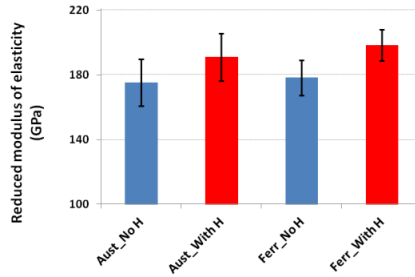


Fig. 9. The hydrogen effect on the reduced modulus of elasticity

The effect of hydrogen on the hardness is larger for the austenite than for the ferrite, the differences in hardness, before and after hydrogen charging, being of about 1 GPa for the austenite and of 0.6 GPa for the ferrite. A higher increase in the hardness for the austenite is due to a higher solubility of hydrogen in the austenite as comparing to the ferrite.

From Fig. 9, we can disregard the effect of hydrogen since the increase of the reduced modulus of elasticity is within the measurement error and it is not sure that is due to the presence of hydrogen.

Another effect of hydrogen evolved during the cathodic potential is on the onset of plasticity. Fig. 11 presents typical load displacement curves and the difference between the pop-in load levels, when the nanoindentations are made with and without hydrogen. Since more than 30 nanoindentations were made for each phase and each testing condition in order to have repeatability, the pop-in event frequencies are presented in Fig. 10. A decreasing in pop-in load level was observed for both the austenite and the ferrite phases.

The elastic part of the load – displacement curves presented in Fig. 11 can be fitted to the Hertzian equation:

$$P = 1.33E_r h^{1.5} \sqrt{R} \quad (9)$$

where: P - the applied load, h - the indentation depth, R - the radius of the indenter tip, E_r - reduced modulus of the sample, given by the Eq. (7).

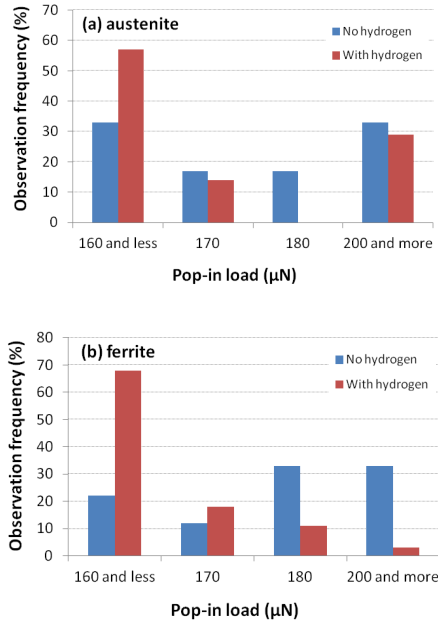


Fig. 10. Pop-in event frequencies for (a) austenite, (b) ferrite

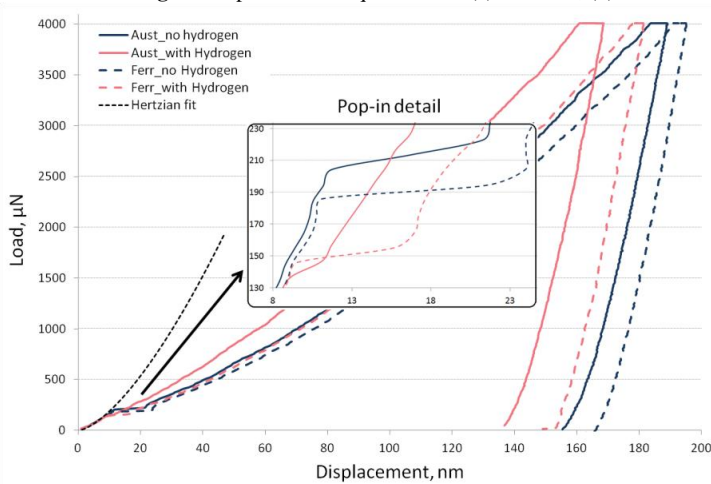


Fig. 11. The reduction in the onset of plasticity (pop-in load level) due to hydrogen

During a nanoindentation, the indenter tip will approach the sample with a certain velocity and as soon as the contact is established, the initial elastic loading begins until the first dislocation nucleation (or pop-in) occurs. The stress field underneath the indenter tip during the elastic deformation is described via continuum mechanics, assuming that the indenter tip is spherical [17]. When this assumption is made, the maximum shear stress under the indenter tip is:

$$\tau_{max} = 0.31 \sqrt[3]{\frac{6E_r^2 P}{\pi^3 R^2}} \quad (10)$$

According to continuum mechanics, the maximum shear stress occurs at a distance of approximately 0.48 times the contact radius, r_c , directly below the center axis of the contact, between the sample and the indenter tip [17]:

$$z_{\tau(max)} = 0.48 r_c \quad (11)$$

If the contact radius between the indenter tip and the sample is [17]:

$$r_c = \frac{\pi R}{2E_r} \sqrt[3]{\frac{6E_r^2 P}{\pi^3 R^2}} \quad (12)$$

replacing Eq. (12) in Eq. (11), the position of the maximum shear stress, $z_{\tau(max)}$ can be calculated as:

$$z_{\tau(max)} = 0.48 r_c = 0.48 \sqrt[3]{\frac{3PR}{4E_r}} \quad (13)$$

The maximum shear stress acting at the $z_{\tau(max)}$ is responsible for the homogeneous dislocation nucleation in the volume below the surface and is in the order of the theoretical strength of a defect free material, according to the Frenkel model [18]:

$$\tau_{th} \approx \frac{G}{2\pi} \approx \frac{G}{10} \quad (14)$$

where G is the shear modulus.

Now, we can equate the measured maximum shear stress during pop-in to the theoretical strength of the austenite or the ferrite phase in Eq. (14). This relates any change in the pop-in load to a change in the shear modulus of the given phase in SDSS as a result of hydrogen. In other words, hydrogen not only facilitates the dislocation nucleation, but also reduces the lattice cohesion [19].

A deeper analysis of the pop-in behavior was made using a pop-in finder program developed by Barnoush [14]. The program is using the load displacement curves imported from the Hysitron software and is finding the pop-in from the analysis of the regions where the displacement is constant. Further, based on the Hertzian fit, Eq. (9) the tip radius is found and used for calculating the position of the maximum shear stress and its value, Eq. (10) to (13).

Fig. 12 presents the decrease in both pop-in width and pop-in load for the austenite and the ferrite, in the presence of hydrogen. The pop-in i.e. homogeneous dislocation nucleation in the austenite requires higher load levels than the ferrite, but the width of the pop-in is smaller. The pop-in width in the austenite is reduced to half in the presence of hydrogen while for the ferrite, the decreasing is around one third.

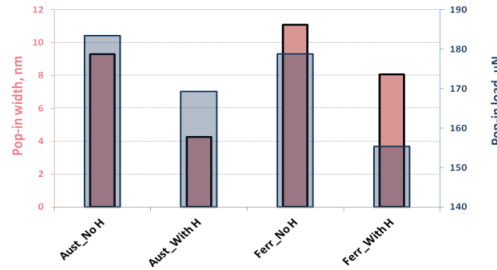


Fig. 12. Pop-in width and pop-in load from the pop-in analysis

Table 2 presents a summary of the nanomechanical properties of the SDSS, extracted from the load-displacement curves and from the pop-in finder program. The maximum shear stresses are higher when hydrogen is present in the material and closer to the surface. It should be mentioned that in the SDSS, in order to have both phases in quasi equilibrium with each other, it is necessary to quench them from about 1100°C down to the room temperature. This results in the formation of very high tensile stresses in the austenite and compressive stresses in the ferrite [20]. This is very important to consider the effect of these local high residual stresses on hydrogen uptake and its effect on the measured nanomechanical properties. Therefore, future works are planned to study the effect of hydrogen on the nanomechanical response of the austenite and the ferrite phases in combination with these residual stresses.

4. CONCLUSIONS AND FURTHER WORK

The increase in the hardness and the decrease in the pop-in load level of both the austenite and the ferrite phases were observed due to hydrogen evolution after the cathodic potential was applied to the sample. While the decrease in the pop-in can be related to the hydrogen effect on the interatomic potential, the cohesion the effect of hydrogen on hardness is in agreement with the hydrogen pinning effect on the dislocations.

Table 2. Summary of the nanomechanical properties of SDSS

	Load displacement curves			Pop-in analysis				
	H (GPa)	Er (GPa)	S (μN/nm)	Start load (μN)	Start depth (nm)	Width (nm)	Maximum shear stress	
							$Z_{\tau(max)}$ (nm)	τ_{max} (GPa)
Austenite_air	5.1	175	176	183	10.8	9.3	31.1	2.90
Austenite_hydrogen	6.4	191	171	177	11.5	4.0	26.5	3.74
Ferrite_air	4.8	178	184	178	11.2	11	27.7	3.40
Ferrite_hydrogen	5.3	198	194	155	10.9	8.0	23.4	3.43

The Super Duplex Stainless Steel is a very complex material as well as is the hydrogen embrittlement micromechanism and further investigations have to be made. Further work will focus on the hydrogen effect on the grains with different crystallographic orientations. Also, different loading rates will be considered.

REFERENCES

1. **Trojano, A.R.**, 1960, The role of hydrogen and other interstitials in the mechanical behaviour of metals, *Trans ASM*, 52, pp. 54-80.
2. **Birnbaum H.K., Sofronis P.**, 1994, Hydrogen-enhanced localized plasticity-a mechanism for hydrogen-related fracture, *Materials Science and Engineering: A*, 176(1-2), pp. 191-202.
3. **Nilsson J.O.**, 1992, Super duplex stainless steels, *Material Science and Technology*, 8(8).
4. **Krauss G.**, 2005, Steels: processing, structure, and performance.
5. **Zakroczymski T., Owczarek E.**, 2002, Electrochemical investigation of hydrogen absorption in a duplex stainless steel, *Acta Materialia*, 50(10), pp. 2701-2713.
6. **Oltra R., Bouillot C., Magnin T.**, 1996, Localized hydrogen cracking in the austenitic phase of a duplex stainless steel, *Scripta Materialia*, 35(9), pp. 1101-1105.
7. **Johnsen R., Nyhus B., Wästberg S., Lauvstad G.O.**, 2007, New Improved Method For Hisc Testing Of Stainless Steels Under Cathodic Protection. Corrosion, paper no. 07496.
8. **Olden V., Thaulow C., Johnsen R., Østby E., Berstad T.**, 2009, Influence of hydrogen from cathodic protection on the fracture susceptibility of 25%Cr duplex stainless steel - Constant load SENT testing and FE-modelling using hydrogen influenced cohesive zone elements. *Engineering Fracture Mechanics*, 76(7), pp. 827-844.
9. **Olden, V., Thaulow, C., Johnsen R., Ostby E.**, 2007, Cohesive zone modeling of hydrogen-induced stress cracking in 25% Cr duplex stainless steel. *Scripta Materialia*, 57(7), pp. 615-618.
10. **Oliver W.C., Pharr G.M.**, 1992, An improved technique for determining hardness and elastic modulus. *J. Mater. Res.*, 7(6).
11. **Fang, T., Chang W., Tsai S.**, 2005, Nanomechanical characterization of polymer using atomic force microscopy and nanoindentation. *Microelectronics Journal*, 36(1), pp. 55-59.
12. **Barnoush A., Vehoff H.**, 2006, Electrochemical nanoindentation: A new approach to probe hydrogen/deformation interaction, *Scripta Materialia*, 55(2), pp. 195-198.
13. **Barnoush A., Vehoff H.**, 2008, In situ electrochemical nanoindentation: A technique for local examination of hydrogen embrittlement, *Corrosion Science*, 50(1), pp. 259-267.
14. **Barnoush A.**, 2008, Hydrogen embrittlement, revisited by in situ electrochemical nanoindentation, PhD Dissertation.
15. **Øverland M.**, 2007, Hydrogen induced stress cracking in super duplex stainless steel, Master thesis.
16. **Hysitron**, 2009, TI-750 Ubi User Manual NRL-M-201 r9.0.0609 (TriboScan 9.1).
17. **Johnson K.L.**, 1985, Contact Mechanics. Cambridge Press, pp. 85-95.
18. **Frenkel, J.**, 1926, Zur Theorie der Elastizitätsgrenze und der Festigkeit kristallinischer Körper, *Zeitschrift für Physik A Hadrons and Nuclei*, Springer Berlin / Heidelberg, 37: pp. 572-609.
19. **Barnoush A., Vehoff H.**, 2010, Recent developments in the study of hydrogen embrittlement: Hydrogen effect on dislocation nucleation, *Acta Materialia*, 58(16), pp. 5274-5285.
20. **Barnoush A., Zamanzade M., Vehoff H.**, 2010, Direct observation of hydrogen-enhanced plasticity in super duplex stainless steel by means of in situ electrochemical methods. *Scripta Materialia*, 62(5), pp. 242-245.

ISBN 978-82-326-5288-4 (printed ver.)
ISBN 978-82-326-5250-1 (electronic ver.)
ISSN 1503-8181 (printed ver.)
ISSN 2703-8084 (online ver.)



NTNU

Norwegian University of
Science and Technology